DISSERTATIONES
CHIMICAE
UNIVERSITATIS
TARTUENSIS
205

MADIS LÜSI

Electroreduction of oxygen on nanostructured palladium catalysts

DISSERTATIONES CHIMICAE UNIVERSITATIS TARTUENSIS
205

DISSERTATIONES CHIMICAE UNIVERSITATIS TARTUENSIS
205

MADIS LÜSI

Electroreduction of oxygen on nanostructured palladium catalysts

UNIVERSITY OF TARTU
Press

Institute of Chemistry, Faculty of Science and Technology, University of Tartu, Estonia

The dissertation is accepted for the commencement of the degree of *Doctor Philosophiae* in Chemistry on June 18th, 2021 by the Council of Institute of Chemistry, Faculty of Science and Technology, University of Tartu.

Supervisors: Assoc. Prof. Kaido Tammeveski
Institute of Chemistry, University of Tartu, Estonia

PhD Heiki Erikson
Institute of Chemistry, University of Tartu, Estonia

Opponent: PhD Serhiy Cherevko
Forschungszentrum Jülich GmbH, Germany

Commencement: August 25th, 2021 at 10.15, Ravila 14A–1020, Tartu (Chemicum) and Microsoft Teams (*online*)

This work has been partially supported by ASTRA project PER ASPERA Graduate School of Functional Materials and Technologies receiving funding from the European Regional Development Fund under project in University of Tartu, Estonia

ISSN 1406-0299
ISBN 978-9949-03-646-2 (print)
ISBN 978-9949-03-647-9 (pdf)

University of Tartu Press
www.tyk.ee

TABLE OF CONTENTS

1. LIST OF ORIGINAL PUBLICATIONS

I **M. Lüsi**, H. Erikson, K. Tammeveski, J. Solla-Gullon, J.M. Feliu Oxygen reduction reaction on Pd nanoparticles supported on novel mesoporous carbon materials (manuscript submitted for publication)

II H. Erikson, **M. Lüsi**, A. Sarapuu, K. Tammeveski, J. Solla-Gullon, J.M. Feliu, Oxygen electroreduction on carbon-supported Pd nanocubes in acid solutions, *Electrochimica Acta* 188 (2016) 301–308.

III **M. Lüsi**, H. Erikson, A. Sarapuu, K. Tammeveski, J. Solla-Gullon, J.M. Feliu, Oxygen reduction reaction on carbon-supported palladium nanocubes in alkaline media, *Electrochemistry Communications* 64 (2016) 9–13

IV **M. Lüsi**, H. Erikson, A. Sarapuu, M. Merisalu, M. Rähn, A. Treshchalov, P. Paiste, M. Käärik, J. Leis, V. Sammelselg, T. Kaljuvee, K. Tammeveski, Electroreduction of Oxygen on Carbide-Derived Carbon Supported Pd Catalysts, *ChemElectroChem* 7(2) (2020) 546–554.

V **M. Lüsi**, H. Erikson, M. Merisalu, M. Rähn, V. Sammelselg, K. Tammeveski, Electrochemical reduction of oxygen in alkaline solution on Pd/C catalysts prepared by electrodeposition on various carbon nanomaterials, *Journal of Electroanalytical Chemistry* 834 (2019) 223–232.

VI **M. Lüsi**, H. Erikson, A. Treshchalov, M. Rähn, M. Merisalu, A. Kikas, V. Kisand, V. Sammelselg, K. Tammeveski, Oxygen reduction reaction on Pd nanocatalysts prepared by plasma-assisted synthesis on different carbon nanomaterials, *Nanotechnology* 32(3) (2020) 035401.

VII **M. Lüsi,** H. Erikson, M. Merisalu, A. Kasikov, L. Matisen, V. Sammelselg, K. Tammeveski, Oxygen electroreduction in alkaline solution on Pd coatings prepared by galvanic exchange of copper, *Electrocatalysis* 9(3) (2018) 400–408.

Authors contributions:

Paper I: The author performed all of the electrochemical measurements, synthesis of catalysts, analysis of data and is mainly responsible for writing of the paper.

Paper II: The author measured electrochemical data for $HClO_4$ part of the work and participated in the data analysis and writing of the paper.

Paper III: The author performed all of the electrochemical measurements, analysed the data and participated in the writing of the paper.

Paper IV: The author prepared the catalyst materials, performed all of the electrochemical experiments, performed data analysis and is mainly responsible for writing of the paper.

Paper V: The author prepared catalyst materials, conducted all electrochemical experiments and analysed the data. The author is mainly responsible for the writing of the paper.

Paper VI: The author performed all of the electrochemical measurements and data analysis. Participated in the writing of the paper.

Paper VII: The author performed all of the electrochemical measurements, analysed the data and is mainly responsible for writing of the paper.

2. ABBREVIATIONS AND SYMBOLS

ads – adsorbed
AEMFC – anion exchange membrane fuel cell
ALD – atomic layer deposition
BE – binding energy
CB – carbon black
C^{b}_{O2} – oxygen concentration in bulk solution
CDC – carbide-derived carbon
CNT – carbon nanotubes
CTAB – cetyltrimethylammonium bromide
CV – cyclic voltammetry
CVD – chemical vapour deposition
D_{O2} – oxygen diffusion coefficient
DFT – density functional theory
E – potential
$E_{1/2}$ – half-wave potential
E_{onset} – onset potential
$E°$ – standard electrode potential
ECS – engineered catalyst support
EDX – energy dispersive X-ray spectroscopy
ESA – electrochemical surface area
F – faraday constant
FC – fuel cell
fcc – face-centred cubic
GC – glassy carbon
GDL – gas-diffusion layer
GNP – graphene nanoplatelets
GNS – graphene nanosheets
GO – graphene oxide
HMT-PMBI – hexamethyl-*p*-terphenyl-poly(benzimidazolium)
HOPG – highly oriented pyrolytic graphite
HR-SEM – high-resolution scanning electron microscopy
I_k – kinetic current
j – current density
j_d – diffusion-limited current density
j_k – kinetic-limited current density
k – electrochemical rate constant
K-L – Koutecky-Levich

n	–	number of electrons transferred
NGO	–	N-doped graphene oxide
NrGO	–	N-doped reduced graphene oxide
MA	–	mass activity
MEA	–	membrane-electrode assembly
MP-AES	–	microwave plasma atomic emission spectroscopy
MWCNT	–	multiwalled carbon nanotube
ORR	–	oxygen reduction reaction
PdNP	–	palladium nanoparticles
PSD	–	pore size distribution
PtNP	–	platinum nanoparticles
PVP	–	polyvinylpyrrolidone
RDE	–	rotating disc electrode
rGO	–	reduced graphene oxide
RHE	–	reversible hydrogen electrode
SA	–	specific activity
SEM	–	scanning electron microscopy
SCE	–	saturated calomel electrode
SHE	–	standard hydrogen electrode
TEM	–	transmission electron microscopy
UDP	–	underpotential deposition
UHV	–	ultrahigh vacuum
XPS	–	X-ray photoelectron spectroscopy
v	–	kinematic viscosity of the solution
ω	–	rotation rate of the electrode

3. INTRODUCTION

The oxygen reduction reaction (ORR) is studied due to its applications in fuel cells, hydrogen peroxide synthesis and metal-air batteries. In general, the ORR proceeds through two main pathways: $2e^-$ pathway (preferred for peroxide synthesis) and $4e^-$ pathway [1-3]. The $4e^-$ ORR pathway is preferred for fuel cell and metal-air battery applications. The most active single metal catalyst for low-temperature polymer electrolyte fuel cells is Pt. The second best metal for the ORR is Pd, which historically had lower price when comparing to Pt [1]. This price difference has changed in recent years, however, more Pd is available in Earth's crust. There have been studies showing that Pd outperforms Pt as ORR catalyst in alkaline media [4-6]. The aim of this study was to use various Pd deposition methods to prepare carbon-supported Pd nanoparticles and to evaluate different support material effects on the Pd catalyst activity for the ORR in both alkaline and acidic media employing the rotating disk electrode technique.

In the first part of the work the Pd nanoparticles were prepared using a citrate method and deposited onto various porous commercially available nitrogen-doped carbon materials, the effect of the porosity and N-doping was evaluated for the ORR and one of the catalysts was studied in a single-cell anion exchange membrane fuel cell [I]. In the second part carbon-supported cubic Pd nanoparticles were studied for ORR, where the effect of their unique morphology was evaluated [II, III]. In the third part carbide-derived carbons were used as support materials for Pd catalysts. Pd nanoparticles were deposited onto these supports using borohydride method and the effects of the support porosity on the Pd deposition were evaluated. These materials were electrochemically evaluated using cyclic voltammetry and ORR studies [IV]. In the fourth part of the work, electrodeposition method was employed for Pd particle dispersion onto various nanocarbon supports. Effects of electrochemical activation and electrodeposition overpotential were studied in relation to the obtained Pd deposits. These deposits were also electrochemically tested for ORR [V]. Following the electrodeposition, physical deposition was applied with novel plasma-assisted method in the liquid phase, where Pd ions were reduced using solvated electrons. Furthermore, the graphene oxide used as a support was reduced to reduced graphene oxide (rGO) in parallel to Pd. The ORR on these novel catalyst materials was studied [VI]. In the final part galvanic exchange as a deposition method for Pd catalysts was evaluated. For consistency, the electron beam evaporation method was used for deposition of Cu layers onto glassy carbon electrodes. These electrodes were then submerged to the Pd^{2+} ion containing solution resulting in replacement of Cu with Pd. The ORR electrocatalytic activity of these thin Pd films was investigated [VII].

4. LITERATURE OVERVIEW

4.1 The oxygen reduction reaction

Due to the relevance of oxygen reduction reaction (ORR) in the field of fuel cells and metal-air batteries the reaction has been extensively studied. It occurs on the cathode side of the fuel cell and is limited by sluggish kinetics and further complicated by reaction mechanism. Multiple pathways for oxygen reduction must be considered. The main ORR pathways observed for Pt group metals are direct $4e^-$ pathway and the series $2e^- + 2e^-$ pathway [7]. During the $2e^- + 2e^-$ pathway a part of the generated peroxide can desorb and it may cause the degradation of the fuel cell cathode catalysts and ion exchange membranes [8].

In alkaline media the relevant ORR pathways are [8]:

Direct: $O_{2,ads} + 2H_2O + 4e^- \rightarrow 4OH^-$ $\quad E^0 = 0.401$ V (1)

Series: $O_{2,ads} + H_2O + 2e^- \rightarrow HO_2^- + OH^-$ $\quad E^0 = -0.065$ V (2)

$HO_2^-{}_{,ads} + H_2O + 2e^- \rightarrow 3OH^-$ $\quad E^0 = 0.867$ V (3)

In acidic media the relevant ORR pathways are [8]:

Direct: $O_{2,ads} + 4H^+ + 4e^- \rightarrow 2H_2O$ $\quad E^0 = 1.229$ V (4)

Series: $O_{2,ads} + 2H^+ + 2e^- \rightarrow H_2O_2$ $\quad E^0 = 0.70$ V (5)

$H_2O_{2,ads} + 2H^+ + 2e^- \rightarrow 2H_2O$ $\quad E^0 = 1.76$ V (6)

where E^0 is the standard potential vs. SHE.

The mechanisms of the ORR have been extensively studied on Pt electrodes [9, 10]. It has also been shown computationally that the $4e^-$ reduction is the most likely pathway in acidic media for O_2 reduction to water [11]. In alkaline, however, there is increased likelihood of parallel $2e^- + 2e^-$ pathway due to the lower working potentials, which could facilitate HO_2^- desorption [12]. The ORR is the limiting factor in low-temperature fuel cell development due to its sluggish kinetics, high price of the catalyst, low resistivity to poisoning and insufficient long-term stability. In case of Pt it has been shown that strongly adsorbed hydrogen inhibits the ORR rate and promotes peroxide production. Markovic and others showed that in the H_{UDP} region the ORR follows a two-electron reduction pathway on Pt(hkl) surfaces [13, 14]. Similar increase in peroxide production in the H_{UDP} region has also been noted on Pd, furthermore the extent of H_2O_2 production was higher in the

H_{UDP} region for Pd as compared to Pt due to higher quantity of hydrogen adsorbed on Pd within that region [6]. Reaction mechanism for ORR if the Pd electrode is covered by oxide layer has also been studied and it was suggested that the introduction of PdO promotes peroxide intermediate formation [15]. The effect of surface blocking by Cl^- ions has been studied by Ledendecker et al. showing nearly 100% selectivity between 0.1–0.5 V (vs RHE) for peroxide production in 0.1 M $HClO_4$ on PdNPs synthesised using $PdCl_2$ as a precursor and only 60% selectivity for Pd nanoparticles prepared from $Pd(acac)_2$ [16].

4.2 Oxygen reduction reaction on palladium

Among the pure noble metals used for ORR Pt and Pd are the best electrocatalysts for this reaction [1–3, 8, 17, 18]. Pt is better to use in acidic conditions and is currently widely used in low-temperature fuel cell applications. Due to scarcity and high price of Pt, alternatives are sought for. Pd belongs to the same group in the periodic table and has same face-centred cubic (fcc) crystal structure. Furthermore, Pd is more abundant in Earth's crust, which has led to extensive study of Pd as a replacement to Pt [1, 2]. However, due to increase in palladium consumption and deficit in Pd production the price of Pd has increased since 2009 by about 10-fold while Pt price has only increased by about 10% in the same time-period [19, 20]. While the activity and stability of Pd is lower than that of Pt in acidic conditions, there are studies showing opposite in alkaline media [4–6]. In acidic media the lower activity of Pd is often ascribed to stronger adsorption of anions such as Cl^-, ClO_4^-, SO_4^{2-}, which block the active sites for O_2 adsorption on the Pd catalyst [2]. Arriaga et al. compared graphene and carbon black supported Pd and Pt catalysts in alkaline solution and found that Pd/graphene outperformed Pt/graphene, while using carbon black as a catalyst support the Pt catalyst outperformed Pd [5]. Superior activity on Pd/graphene was also noted by Kim et al. by comparing to similarly prepared Pt/graphene catalyst [4]. Furthermore, it has been shown that Pd/C is more stable in alkaline environment than Pt/C [21].

The ORR on polycrystalline Pd proceeds through a 4-electron pathway yielding water as the final product and the reaction mechanism is proposed to be same for Pd as on Pt [1]. Tafel slopes have been used to characterise both Pd and Pt catalyst materials, where the reaction mechanism is described by two slopes of –120 and –60 mV. At high current densities the slope value of –120 mV is observed and is related to Pd surface that is not covered by oxides, while –60 mV slope at low current densities is attributed to Pd catalyst, which is covered by oxides [22]. In both of these Tafel regions the rate-limiting step for oxygen reduction is considered to be the transfer of the first electron to the adsorbed O_2 molecule [22].

The ORR activity has been explored on the low-index planes of Pd [23]. In perchloric acid it was shown that the Pd(100) facet was 3 times more active for ORR than the most active plane of Pt. The activity of Pt low-index planes follows the order (110) ≈ (111) > (100) with the activity difference between (111) and (110) being small, however the difference is greater in KOH solution [14]. In case

of Pd the most active facet is (100) followed by (111) and (110), with 14 times kinetic current density difference between (100) and (111) [23]. The effect of the oxide film to the n(111)–(100) series in perchloric acid showed that the ORR activity is not affected by the oxides at 0.9 V, which contradicts results found using Pt [24]. To date no such study has been done on monocrystalline Pd in alkaline.

4.3 ORR on nanostructured palladium

Discoveries on the electrocatalytic activity differences on low-index Pd planes has led to study of shape-controlled Pd particles and there are studies, where higher activity using Pd nanocubes in comparison to conventional spherical Pd particles has been achieved in both acidic and alkaline conditions [25–30]. However, there are contradicting results, as Shao and others compared 5–6 nm Pd octahedra (with preferential (111) facets) to cubic nanoparticles (with preferential 100 facets) and found 10-fold activity increase in $HClO_4$, 17-fold activity increase in H_2SO_4 with their cubic particles but no difference in the ORR activity between these particles in alkaline environment [31]. Particle shape control has been also applied to triangular Pd rods, that were prepared to have predominant (111) planes, showed higher activity as compared to polycrystalline Pd [32]. Ten times increase in specific activity has been observed on Pd nanorods in which case the activity increase was attributed to (110) planes [33]. Furthermore, it has been shown that the cubic particles, even when studied in alkaline where Pd is more stable become spherical during potential cycling [34]. Stability of Pd nanocubes in alkaline media showed that by increasing the concentration of hydroxide from 0.1 M to 1 M leads to the increasing loss of kinetic current after 1000 potential cycles from 21.3% to 52.5% [30].

Pd particle size effect has been evaluated in perchloric acid by Xue et al. [35]. In their work they varied Pd particle size between 2.7 and 8.7 nm and found that the mass activity increased monotonically, however, specific activity showed a volcano plot with maximum around 5–6 nm. The decrease in specific activity was attributed to surface blockage of reaction intermediates such as –OH. Similar effects were studied in alkaline media by Jiang et al., where particle sizes were varied between 3 and 16.7 nm, however, specific activity in the case of alkaline did not reach a maximum with increased OH^- adsorption being suggested as the reason for the lower specific activity. Furthermore, it was shown that the mass activity increases when Pd particle size increased from 3 to 5 nm by 1.3 fold and showed a volcano plot with a maximum around 5 nm [36]. Particle size effect has also been demonstrated using DFT on Pd@Pt core-shell nanoparticles where it was shown that particle size variation from 1 to 2.6 nm on pyramidal particles increases oxygen binding energy (BE) from 1.1 to 1.7 eV, while with spherical particles the BE decreased from 2.1 to 1.3 eV when decreasing particle size from 2.2 to 1.2 nm [37]. Pt and Pd particle size effect has also been evaluated by Offin and others, by studying particle sizes between 1.5–5.5 nm and found that the optimum for Pt was around 4 nm in 0.5 M perchloric acid, while no optimum for Pd

particles within range up to 11 nm was observed for neither mass nor specific activity [38].

Since larger particles generally have lower mass activities, which drive the price of the catalyst material, better utilisation of the noble metal could be achieved through core-shell structured catalysts [39]. Core-shell catalysts are constructed in a way that the precious metal covers some cheaper metal, thus reducing the cost. Furthermore, it has been shown that the underlying metal can affect the electronic surface structure of the overlying metal. Adzic and co-workers have studied shifting of the d-band centre of Pt, where underlying Pd reduced the interaction of Pt-O and thus increased the activity [40]. Oxygen binding energy has been correlated to the ORR activity and volcano plots have been devised for Pt alloys, where the optimal BE for ORR is –0.2 eV lower than pure Pt with a binding energy of –2.04 eV [41]. Using DFT methods Adzic et al. has also determined the binding energy for Pd-O bond and found that particles with Pd_3Fe core and Pd shell show most optimal binding energy and lead to higher mass activity than commercial Pt/C [42–44]. Optimum shell thickness was discussed by Jiang et al. who observed a drop in half-wave potential as shell thickness increased above 0.71 nm [45]. The effect of the underlying substrate has also been discussed by Liu and others in their work, where PdNPs were deposited on SnO_2 nanowires. Increase of lattice spacing of 0.005 nm was observed, which was used to interpret increase of ORR activity, however the thickness of the particles where the spacing was observed was not available [46]. Lattice contraction has also been achieved on BN and C/BN supports for Pd(111) plane and the observed lattice contraction was 4.2% and 3.4% respectively, which leads to downshift in d-band centre and could weaken the adsorbate bond strength [47].

4.4 ORR on Pd catalysts deposited on different supports

The effect of the support material on the ORR electrocatalytic activity and stability has been extensively studied [3, 18]. Pd/C stability differences were studied on two different carbon black materials, where it was shown that the activity for both materials was similar, however, higher stability was observed on Vulcan carbon in comparison to Ketjenblack carbon [48]. Another study looked at pre-treatment of support material for Pd nanoparticles and it was observed that the pre-treatment of Vulcan carbon can lead to differences in morphology and dispersion of PdNPs and affect the amount of peroxide produced during the ORR process, however H_3PO_4, KOH and H_2O_2 treatment lead to 5-fold increase in activity compared to commercial Pd/C while HNO_3 treatment resulted in 10-fold decrease in activity [49]. Treatment with 5% HNO_3 and H_2O_2 led to 25–50% loss of porosity while 0.07 M H_3PO_4 and 0.2 M KOH kept the original porosity, furthermore, H_2O_2 treatment led to severe loss in the microporosity. Graphitisation degree of graphene supports was discussed by Atanassov and co-workers showing better PdNP dispersion on graphene supports as compared to Pd/Vulcan and suggesting that one of the reasons for the higher peroxide production on Pd/Vulcan in comparison to the Pd/GNS materials is due to interparticle distance with

agglomeration reducing the number of available peroxide re-adsorption sites [50]. In a follow up study it has been discussed that the microporosity can facilitate peroxide production on graphene materials [51]. One of the main methods to improve particle dispersion is looking at support materials for available sites for Pd particle anchoring. By studying graphene oxide (GO) supported PdPt particles, excessive reduction of the GO lead to agglomeration of the nanoparticles [52]. Similar Pd particle agglomeration has also been noted on carbon nanotubes (CNT) in multiple works [53–55]. To overcome this lack of sites linkers have been employed, Jiang and co-workers showed a better dispersion of Pd particles on multiwalled carbon nanotubes (MWCNT) using tungstophosphoric acid that was immobilised on the surface of MWCNT using polydiallyldimethylammonium chloride [56]. Same group later achieved good dispersion of PdNPs on Ni modified CNTs using poly(diallyldimethylammonium) chloride linkers [57]. Linkers have been also studied by Jeon and others on graphene surfaces [58]. Another group of materials that has been studied are various mesoporous carbons, which have high specific surface area and could facilitate better dispersion of nanoparticles [59, 60]. Furthermore, there is an interesting method of obtaining support materials with controlled porosity by deriving them from metal carbides, these materials are called carbide-derived carbons (CDC) [61, 62]. CDCs have been extensively studied as Pt nanoparticle support by Lust and co-workers [63–65]. When preparing CDC supports their porosity can be varied by choice of the starting carbide and leaching method making the method highly tuneable for preparation of porous carbon supports [61, 62].

There are various studies showing increase in particle dispersion by N-doping of the substrate material [66, 67]. Gennaro and co-workers reported that larger Pd nanoparticles (5–6 nm) were formed on non-doped mesoporous carbon, while smaller nanoparticles (2–4 nm) were observed on N-doped mesoporous carbon [67]. Generally, the increase in ORR activity is attributed to better dispersion of the Pd particles on the support since in order to affect the electron structure of Pd atomic or near atomic dispersion is required. A better dispersion and smaller Pd particle size was achieved by Jeon and others showing average particle size decrease from 8 to 2.5 nm by adding 3-aminomethylpyridine to rGO [68]. Similarly smaller PdNPs on N-doped graphene, which were prepared for direct ethanol fuel cell, where a decrease of average particle size from 4.92 ± 0.51 to 3.6 ± 0.52 nm was observed [69]. However, there are papers discussing Pd-N groups affecting the activity of the Pd catalyst [66, 70]. Chen and others prepared N-doped porous carbon-cages for Pd catalyst and noticed during stability testing a decrease in the area of the PdO reduction peak, however, the ORR activity remained constant and thus suggested that majority of the activity came from Pd-N groups. Furthermore, they studied the ORR in the presence of poisoning species in an attempt to separate Pd-N and metallic Pd contribution and found that Pd-N contributed most to the ORR activity. Sub-nanometre Pd particles coordinated to pyridinic N showed good activity in comparison to larger 2–5 nm particles on N-doped carbon [70].

In order to increase the stability and dispersion of Pd particles N-doping has been employed in both alkaline and acidic conditions [71]. Generally, the

increase in stability is attributed to anchoring effect to the N-groups on the surface of the substrate [71, 72]. There are contradicting results, Granozzi and co-workers showed decreased stability for N-doped carbon materials in acidic media, suggesting that Pd^{2+} presence increases the likelihood of Pd dissolution [73].

4.5 Methods for deposition of palladium

There are three broad methods for preparation of Pd nanoparticles, namely electrodeposition, chemical deposition and physical deposition. Benefits and problems when using these methods for nanoparticle preparation are discussed below.

In electrodeposition the particle size, dispersion and shape can all be controlled by choice of substrate, Pd ion concentration, overpotential, duration of the pulse and presence of other ions, which could adsorb to specific sites and thus control the shape of the deposit. Mechanism of Pd deposition has been studied on pencil graphite, where a three-step process was suggested with initial adsorption, 2D nucleation and 3D diffusion-limited growth [74]. By changing the concentration of the Pd ions, a change in deposited particle shape can be observed due to the diffusion-limited step for 3D growth where nanorods became nanospheres when lowering the concentration [33]. Similarly, a change in morphology can be obtained when changing the overpotential from 250 to 500 mV by which flower-like deposits became spherical particles [75]. Furthermore, the shape of the Pd deposits can be manipulated if nucleation cycles are used before the deposition cycles, for example 14–30 nm nanoneedles can be turned into urchinlike deposits [76]. Uosaki and co-workers noticed during Pd deposition that the adsorption of $PdCl_4^{2-}$ ions inhibited the 3D growth [77, 78]. By studying the effects of the solution Kolb and co-workers noted that the Pd growth on Au (111) in chloride-free environment favours 3D growth [79]. These results were contradicted by a later study by Sibert and co-workers, where in the presence of chloride ions no inhibition of 3D growth was noted [80]. Effect of temperature on the Pd electrodeposition was studied by Yu et al., where the deposition rate changed, however no impact on the surface morphology was noted [81]. By decreasing the $PdCl_2$ concentration from 3×10^{-4} to 3×10^{-5} M a change in the deposit shape from nanorods to nanospheres was observed by Xiao et al., furthermore in the same study by switching from Cl^- ions to Br^- ions at the potential of –0.2 V (vs Ag/AgCl) no Pd electrodeposition occurred [33]. Effects of the support were noted by Unwin and co-workers when studying Pd deposition kinetics on transmission electron microscopy (TEM) grid and highly oriented pyrolytic graphite (HOPG), where the time lag before current flow on the TEM grid was 7 times higher than on HOPG, where they attributed the difference to availability of step-edges, which could trap electrodeposited nuclei and these step-edges are absent on the TEM grids [82]. The effect of the support on the dispersion of Pd nanoparticles depending on the support material has been shown by comparing Vulcan XC-72R carbon and wood apple shell carbon, where the larger electrochemical surface area of deposited Pd was attributed to the increased surface area of the carbon support [83]. Similarly, smaller Pd nanoparticle

deposits were observed on N-doped glassy carbon (GC) in comparison to bare GC, where the increase was ascribed to N-based defects [84]. Variation of particle size was demonstrated by Stimming and co-workers when using double pulse method, where particle radii followed the $t^{1/3}$ rule for the growth pulse [85].

Another deposition method is chemical deposition where the additives are used to facilitate growth in certain directions and limit the growth of the particle size [86]. Various groups have synthesised shape-controlled Pd particles using chemical methods and studied these further. However, with additives comes the requirement to clean these particles, which has proven to be a challenge, since these additives on the surface of the catalyst will reduce its electrocatalytic activity [87]. Effects of the supports on the deposition has been studied by Ejaz and Jeon, they showed difference in Pd growth kinetics depending on the support by switching the support from rGO to N-doped rGO that resulted in reduced Pd particle size from 6–10 nm to 2–4 nm, furthermore it was discussed how different N-centres could affect the growth kinetics of PdNPs [88]. Shape-controlled particles are often prepared with surface blocking agents such as cetyltrimethylammonium bromide (CTAB) [25, 89, 90], polyvinylpyrrolidone (PVP) [31, 91] or Br^- [92, 93], while small spherical particles have been prepared with citrate method [90], and oleylamine has been used to construct defect-rich Pd nanonetworks [94], furthermore the addition of $W(CO)_6$ to oleylamine resulted in Pd nanobelts [95]. Wang and others also added acetic acid and N,N-dimethylformamide to $W(CO)_6$ and oleylamine, which resulted in sub-nanometre thick Pd metallenes [96]. All of these oleylamine methods resulted in active ORR catalysts with high electrochemical surface areas. Shao and others showed how PVP with addition of Br^- could produce 5–6 nm shape-controlled Pd nanocrystals [31]. Using CTAB ~28 nm sized cubic nanoparticles have been synthesised, while using citrate method ~2.8 nm spherical particles were prepared, and these catalysts were used to study the ORR [25]. Depending on the chosen surfactants and reducing agents different shaped particles can be prepared, for example, with PVP and ascorbic acid Pd nanospheres were obtained, when KBr was used cubic particles were received and when changing KBr for citric acid Pd nanooctahedrons were formed [91].

A seldom used method to achieve core-shell structures is galvanic exchange. This method involves exchanging less noble metal for more noble. The process of galvanic exchange has been studied by Buriak co-workers, where they found that the mechanism for the Pd layer growth follows initially island growth followed by overlayer growth, furthermore the concentration of metal ions and temperature play crucial role in size and formation of these islands [97]. Similarly, since the exchanged metal is conductive, growth and dissolution centres can form, hindering the formation of an uniform shell, which requires addition of complexation agents slowing down the exchange of atoms [98]. Formation of dissolution centres and growth centres was noted by Mohl et al. when exchanging Cu rods, where hollow Pd rods with larger diameter were obtained [99]. When studying the galvanic exchange process during electrode rotation it was found that more uniform deposit can be obtained [100]. The effect of Cl^- ions on the exchange process when substituting Cu is contested. It has been suggested that presence of Cl^- improves dissolution of Cu [100] or can form complex with Cu(I)

[101] which could lead to non-uniform deposits. This is contrasted by Sheridan et al. who showed that the presence of excess Cl^- lead to complexation of Pd ions slowing down the deposition process and lead to more uniform deposits [102].

Physical deposition methods include plasma-assisted vapour deposition [103], chemical vapour deposition (CVD) [104, 105], physical vapour deposition [38], atomic layer deposition (ALD) [106–108] and magnetron sputtering [54, 109]. While these methods can provide small particles, the shape control is difficult to achieve. Khalily et al. demonstrated size control of the particles using ALD by increasing the number of cycles, however with higher number of cycles agglomeration became more prominent, furthermore it is difficult to assign the dispersion and size of the particles to the method alone since the deposition was done on N-doped carbon nanofibers [108]. While shape control is generally not shown in these physical methods Papandrew and co-workers prepared Pd nanotubes using CVD, however, their performance in alkaline solution was not much better in comparison to commercial Pd/C [105]. Another negative side for physical methods is that the equipment requirement is higher compared to chemical and electrochemical methods, and vapour deposition methods usually use ultrahigh vacuum (UHV) increasing the cost of preparation of these materials. However, one place where physical methods could shine is preparing multiple objects with minor differences over a short period of time. Abruña and co-workers showed a sputtering method for obtaining binary alloys on glassy carbon and compared them in alkaline media, where PdCu outperformed various other alloys for ORR, which could be obtained in relatively short time, suggesting it to be a relatively good screening tool for binary alloys [109]. Screening of Pt alloys has also been done using physical methods by Cooper and McGinn, where they used plasma sputtering and multicell to scan through various thin-film combinatorial libraries [110].

5. EXPERIMENTAL

5.1 Electrode preparation

Working electrodes were obtained by mounting a glassy carbon (GC) disc (GC-20SS, Tokai Carbon, Japan) with a 5 mm diameter into a Teflon holder. These electrodes were polished on 1.0 and 0.3 μm alumina slurries (Buehler), after which the electrodes were cleaned from the residue by sonicating in isopropanol and water, at least 5 minutes in each.

5.1.1 Preparation of spherical Pd nanoparticles

Spherical PdNPs were prepared using citrate method [26, 90], which used the mixture of K_2PdCl_4 and sodium citrate, where ice cold $NaBH_4$ solution was added. After the synthesis the nanoparticles were supported onto carbon by adding appropriate amount of carbon material to the mixture. The resulting dispersions were thoroughly mixed after which NaOH pellets were added followed by filtering and drying in the oven at 75 °C overnight.

5.1.2 Preparation of Pd nanocubes supported on carbon

30 nm Pd nanocubes were prepared using 10 mL of 10 mM H_2PdCl_4 and 200 mL of 12.5 mM CTAB mixture heated to 95 °C to which 1.6 mL of 100 mM ascorbic acid solution was added [89]. Reaction time was kept 20 min with constant temperature of 95 °C. 10 nm Pd nanocubes were prepared using PVP, K_2PdCl_4, KBr and ascorbic acid water solution, which was heated for 3 h at 80 °C [92]. 7 nm Pd nanocubes were prepared using a similar method, however, some of the bromide was replaced with chloride [93]. In the case of 7 and 10 nm Pd cubes an additional step was used for cleaning that was suggested by Zalineeva et al. [91]. This was followed by filtering and drying overnight at 75 °C.

5.1.3 Preparation of Pd/CDC catalysts

Carbide-derived carbon (CDC) materials were purchased from Skeleton Technologies OÜ (Estonia). Due to the large size, the CDC particles were ball-milled after which PdNPs were deposited on them. Four materials were studied: CDC1 from TiC (post-activated with water vapour treatment) [111], CDC2 from TiC, CDC4 from Mo_2C and CDC5 from SiC. ZrO_2 grinding jar with 5 mm ZrO_2 balls was used for ball-milling. Ball-milling program was 3 cycles of 30 min milling at 800 rpm with 5 min breaks. 1 mM H_2PdCl_4 was used as a precursor solution for Pd/CDC catalyst preparation, which was prepared using $PdCl_2$ (Sigma-Aldrich) and 40 % HCl (Sigma-Aldrich) and Milli-Q water. Synthesis process used 20 mg of CDC material dispersed in 47 ml of 1 mM H_2PdCl_4 to which 0.94 ml of 0.1 M $NaBH_4$ was added. The obtained material was filtered and dried overnight in oven at 60 °C. Same deposition process was also carried out on Vulcan carbon XC-72R (Cabot Corp.) support for comparison.

5.1.4 Preparation of electrodeposited Pd/C catalysts

Cleaned GC electrodes were covered by drop-coating graphene nanoplatelets (GNP, Strem Chemicals, Inc.), graphene nanopowder (GNS, Graphene supermarket), carbon black (CB, Vulcan XC-72R, Cabot Corp.), carbon nanotubes (CNT, NanoLab, Inc.), and the mixture of GNP and CNT (CNT-GNP) suspensions. Carbon inks were prepared with 1 mg of carbon material dispersed in 1 ml of isopropanol. Activation of the carbon surfaces was carried out electrochemically by potential cycling between 0.1 and 1.6 V at 50 mV s^{-1} in Ar-saturated 0.1 M KOH solution. Electrochemical deposition was carried out in deaerated 0.05 M H_2SO_4 solution (prepared from 96% H_2SO_4, Suprapur, Merck) containing 1 mM H_2PdCl_4 (prepared from $PdCl_2$ (Sigma-Aldrich), HCl (Sigma-Aldrich) and Milli-Q water). Two different deposition overpotentials were used with stepping that consisted of 500 steps. First overpotential was 0 V (vs SCE) while second one was –0.25 V (vs SCE), while the non-depositing step for both procedures was 0.85 V (vs SCE). Step duration for deposition was 250 ms, while non-deposition step was 3 s at an electrode rotation rate of 1000 rpm.

5.1.5 Pd/C catalysts prepared using plasma-assisted synthesis

He/H_2 (95/5) mixture (purity of gases 5.0) was used in experiments of plasma-assisted processing. Pd nanoparticles were synthesised on different supports using a simple one-step method as described in [112, 113]. Atmospheric pressure bipolar pulsed (13 kHz) discharge in He/H_2 gas jet with a continuous gas flow of 150 sccm was used for the net injection of electrons and plasma active species into the H_2PdCl_4 solutions with small additives of carbon support. On plasma-liquid interface high local density of solvated electrons is generated, which serve as strongly reducing species for the Pd ions. Current peak of 5 mA was used with estimated current density of 0.4 A cm^{-2}. Synthesis was carried out in sealed silica cell with a volume of 4 ml and temperature not exceeding 40 °C. The solution was deaerated using helium gas prior to the ignition of plasma. During the plasma treatment the solution was sonicated with low-power ultrasonic transducer connected to the bottom of the silica cell. During the deposition absorption bands were measured and complete reduction of Pd ions could be observed in 15 min, however with GO sample, additional reduction time was applied till absorption band of GO at 230 nm shifted to about 270 nm, which indicates partial restoration of electronic conjugation and aromatic structure of rGO [114].

5.1.6 Preparation of Pd nanostructures with galvanic exchange of Cu

Cu films were deposited onto clean GC surface using electron beam evaporation method employing a Vacuum Service OY evaporation device at base pressure of around 1×10^{-6} Torr. Immediately after the deposition process the electrodes were submerged into deaerated 1 mM H_2PdCl_4 solution for 30 min. When the galvanic exchange process was done, the electrodes were rinsed with Milli-Q water. Sacrificial Cu layer thickness was varied between 0.5 and 10 nm. Same deposition process was applied for GC plates used in X-ray photoelectron spectroscopy (XPS) and scanning electron microscopy (SEM) measurements.

5.2 Physical characterisation

For TEM measurements transmission electron microscope JEM-2010 (JEOL), Titan 200 (FEI) or JEM-1400 (JEOL) were used. Sample materials were dispersed and drop-coated on a carbon-covered Cu mesh. Thermogravimetric analysis was carried out with either Mettler-Toledo TGA/SDTA851 thermobalance or Setaram Labsys Evo 1600 thermoanalyzer, with 20% oxygen oxidative atmosphere. High-resolution scanning electron microscopy (HR-SEM) and energy dispersive X-ray spectroscopy (EDX) studies were done using Helios™ NanoLab 600 (FEI) microscope with EDX analyser INCA Energy 350 (Oxford Instruments). SCIENTA SES-100 spectrometer was used for X-ray photoelectron spectroscopy (XPS) analysis. Specific surface area and porosity of the catalyst material were determined using N_2 adsorption-desorption method using NOVAtouch LX2 instrument (Quantachrome Instruments). Raman spectroscopy was performed using a Renishaw inVia spectrometer.

5.3 Electrochemical characterisation

The electrolyte solutions for electrochemical measurements were made from KOH (p.a., Sigma-Aldrich) H_2SO_4 (Suprapur, Merck), $HClO_4$ (Sigma-Aldrich) and Milli-Q water. The used gasses were supplied by AGA with purities of Ar (99.999%), O_2 (99.999%) and CO (99.997%). The electrochemical testing was done in a standard three-electrode glass cell with platinum or gold wire counter electrode and reference electrode was reversible hydrogen electrode (RHE) and all potentials in this work unless stated otherwise are measured and given with respect to RHE. The potential was applied with an Autolab PGSTAT30 potentiostat/galvanostat controlled with General Purpose Electrochemical System (GPES) software. Before the ORR studies, cyclic voltammetry (CV) measurements were carried out in deaerated 0.1 M KOH, 0.5 M H_2SO_4, 0.05 M H_2SO_4 and/or 0.1 M $HClO_4$ solution by scanning potential between 0.1 and 0.8 V with the potential scan rate (v) of 50 mV s^{-1}. Background current was measured in deaerated solution and was subtracted from ORR polarisation data. For CO-stripping experiments CO was adsorbed to Pd by bubbling CO gas at electrode potential of 0.1 V, blockage of Pd was confirmed by potential cycling between 0.1 and 0.4 V, where absence of H_{UPD} region was noted [87]. After which CO was purged from the solution using Ar. The CO was electrochemically oxidised from the Pd surface by scanning to the potential to 1 V at 20 mV s^{-1}. The oxygen reduction measurements were performed in O_2-saturated 0.1 M KOH, 0.5 M H_2SO_4, 0.05 M H_2SO_4 and/or 0.1 M $HClO_4$ solutions by scanning the potential at a rate of 10 mV s^{-1}. For the rotating disk electrode (RDE) experiments electrode rotation was applied using an EDI101 rotator and a CTV101 speed control unit (Radiometer). Rotation rate (ω) of the working electrode was varied between 360 and 4600 rpm. All electrochemical experiments were conducted at room temperature (23 ± 1 °C).

The ORR data was analysed using the Koutecky-Levich (K-L) equation [115]:

$$\frac{1}{j} = \frac{1}{j_k} + \frac{1}{j_d} = -\frac{1}{nFkC_{O_2}^b} - \frac{1}{0.62nFD_{O_2}^{2/3}\nu^{-1/6}C_{O_2}^b\omega^{1/2}} \quad (7)$$

j is the measured ORR current density, j_k and j_d refer to its kinetic and diffusion-limited components, respectively. F is the Faraday constant (96,485 C mol^{-1}), k is the electrochemical rate constant , n is the number of electrons transferred, C^b_{O2} is O_2 concentration in bulk solution, D_{O2} is O_2 diffusion coefficient, v is the kinematic viscosity (ν = 0.01 cm^2 s^{-1} [116]) and ω is the rotation rate of the electrode . For 0.5 M H_2SO_4 solution these values are:, C^b_{O2} = 1.13×10^{-6} mol cm^{-3} [117] and D_{O2} = 1.8×10^{-5} cm^2 s^{-1} [117]. In case of 0.1 M $HClO_4$ these values were used instead: C^b_{O2} = 1.22×10^{-6} mol cm^{-3} and D_{O2} = 1.93×10^{-5} cm^2 s^{-1} [118]. For 0.1 M KOH these values are: C^b_{O2} = 1.2×10^{-6} mol cm^{-3} and D_{O2} = 1.9×10^{-5} cm^2 s^{-1} [119].

To determine the intrinsic activity of the catalyst specific activity (SA) values were calculated:

$$SA = I_k/ESA \quad (8)$$

where I_k stands for kinetic current at given potential and ESA is electrochemically active surface area. Mass activities (MA) were calculated according to:

$$MA = I_k/m_{Pd} \quad (9)$$

where the m_{Pd} corresponds to the mass of palladium on the electrode.

For membrane-electrode assembly (MEA) preparation for anion exchange membrane fuel cell (AEMFC) tests the catalyst inks were prepared by dispersing catalyst and ionomer in 3:1 mixture of methanol and Milli-Q water. Dispersion consisted of 1 wt% solids with 85/15 catalyst/membrane ionomer ratio. Anion exchange ionomer used was hexamethyl-*p*-terphenyl-poly(benzimidazolium) (HMT-PMBI) [120]. This dispersion was pipetted on gas-diffusion layers (GDL) with geometric area of 5 cm^2. Loading of 0.4 mg cm^{-2} on cathode and 0.8 mg cm^{-2} on anode (PtRu/C, 50% Pt, 25% Ru, Alfa Aesar) was employed. Single cell AEM fuel cell performance was evaluated at 60 °C using Greenlight Fuel Cell Test Station (G40 Fuel cell system, Hydrogenics, Vancouver, Canada) with back-pressure of 200 kPa.

6. RESULTS AND DISCUSSION

6.1 Oxygen reduction on spherical Pd nanoparticles supported on ECS

In this part of the work three mesoporous carbon materials were used as supports for spherical Pd nanoparticles synthesised using citrate method [I]. All of these supports are nitrogen-doped, however ECS-003604 is also Nb-doped. Specific surface areas (provided by producer) of the engineered catalyst support (ECS) materials were 730 m^2 g^{-1} for ECS-003604, 730 m^2 g^{-1} for ECS-004201 and 820 m^2 g^{-1} for ECS-004601. The ECS-004601 material differs from ECS-004201 by having higher proportion of larger mesopores (15–50 nm). The purpose of this work was to evaluate these materials in comparison to Vulcan carbon as a Pd/C ORR catalyst support material. These materials were evaluated for ORR in both 0.1 M KOH and 0.5 M H_2SO_4 solutions using the RDE method. 40% Pd loading ECS-003604 and Vulcan were compared using single-cell AEMFC. Materials are named as PdX/Y, where X designates Pd loading and Y corresponds to the support material.

6.1.1 TEM studies of Pd/ECS

From Figure 1 it can be observed that the Pd particle dispersion is better on the ECS-003604 and ECS-004601 supports as compared to Vulcan carbon and ECS-004201. Better dispersion of metal nanoparticles has usually been attributed to higher porosity and N-doping [66, 67]. Particle sizes were counted from the TEM images and since PdNPs were prepared in a single batch the sizes of the particles were same with average size of 3.9 ± 0.6 nm. Worse dispersion on the ECS-004201 material could be explained by the difference in porosity as ECS-004201 has less large mesopores and more of smaller mesopores.

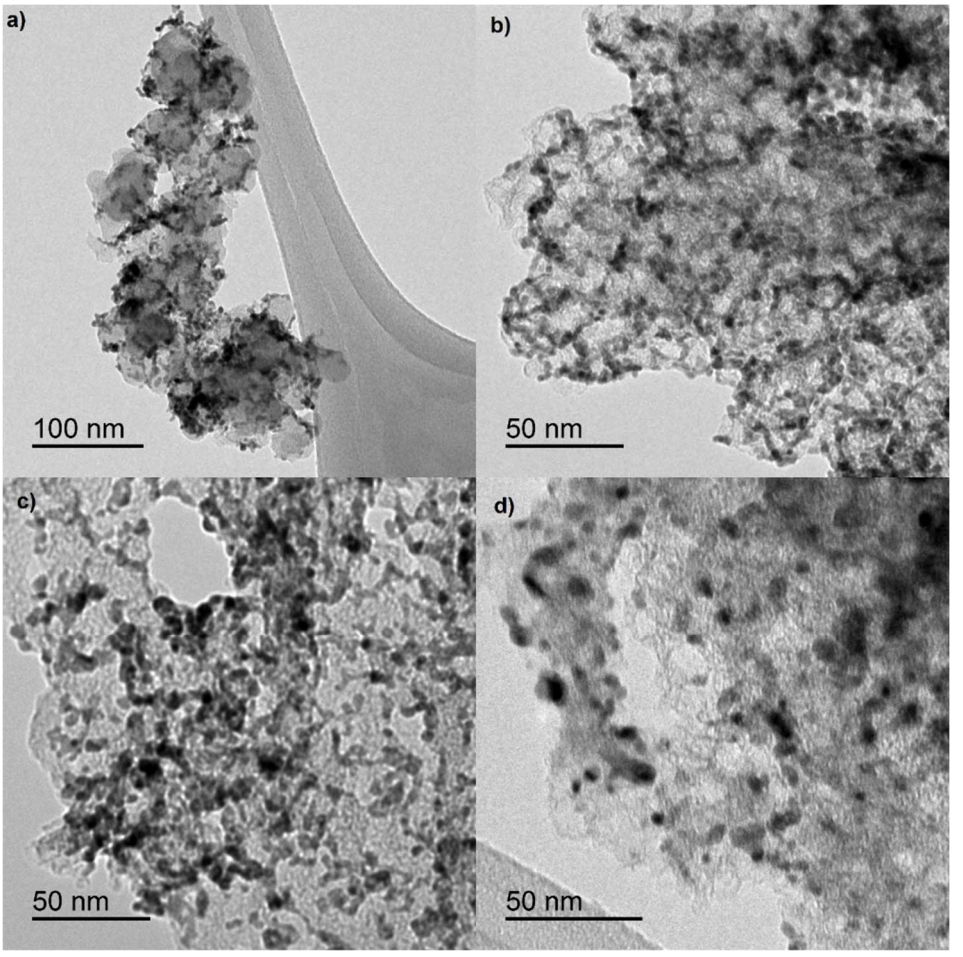

Figure 1. TEM images of (a) Pd40/Vulcan, (b) Pd40/ECS-003604, (c) Pd40/ECS-004601 and (d) Pd40/ECS-004201 samples.

6.1.2 CV and CO experiments on Pd/ECS

Figure 2 presents the CV and CO-stripping profiles measured in Ar-saturated 0.5 M H_2SO_4 solution. When comparing the pseudo-capacitive region of these materials one can clearly see the difference promoted by the variation in the specific surface areas. Three main areas on the CV (Figure 2a) profile can be observed with the peaks between 0.1–0.3 V corresponding to hydrogen desorption and adsorption, then from 0.7 to 1.4 V the increase in current corresponds to Pd surface oxidation, reduction of these oxides can be seen in the reverse scan by a peak centred at 0.7 V. Shifts in the PdO reduction peak location have been attributed to particle size as demonstrated by Jiang et al. when they decreased Pd particle size from 16.7 to 3 nm and observed roughly a 50 mV negative potential shift [36].

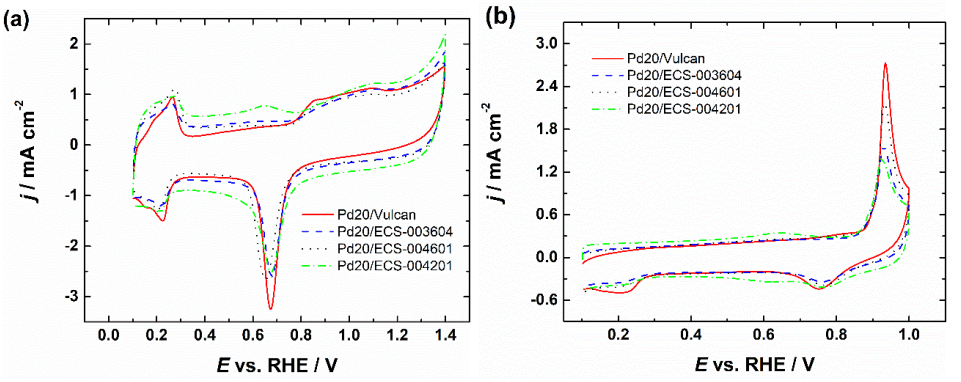

Figure 2. (a) Cyclic voltammograms of Pd/C catalysts in Ar-saturated 0.5 M H_2SO_4 solution, $v = 50$ mV s^{-1} and (b) electro-oxidation of pre-adsorbed CO on Pd/C catalysts, $v = 20$ mV s^{-1}.

With these materials a slight shift of the peak towards more negative potentials can be observed in comparison to Pd/Vulcan, which could be due to higher degree of agglomeration on Pd/Vulcan. These shifts have also been observed on PtNPs in acidic media, where the shift was attributed to stronger adsorption of OH on smaller particles as compared to larger ones [121]. This effect has also been studied by Markovic and co-workers who measured potential of zero charge during OH adsorption with various Pt particle sizes [122].

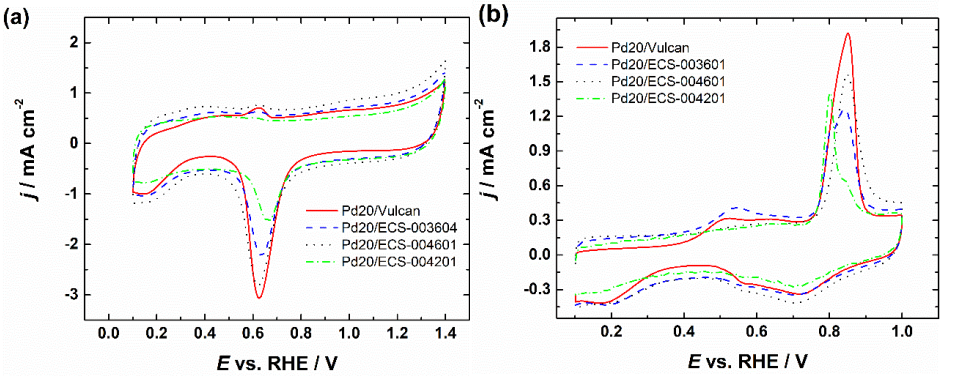

Figure 3. (a) Cyclic voltammograms of Pd/C catalysts in Ar-saturated 0.1 M KOH solution, $v = 50$ mV s^{-1} and (b) electro-oxidation of pre-adsorbed CO on Pd/C catalysts, $v = 20$ mV s^{-1}.

CO-stripping profiles and CV curves in alkaline solution are provided in Figure 3. Compared to acidic media the hydrogen adsorption and desorption region is suppressed, which is typical for Pd catalysts in alkaline media [123]. By looking at Pd/ECS-004201 a shift of the PdO reduction peak to more positive potentials can be observed, while CO oxidation peak shifted negative, which could be due to unique bimodal porosity or larger degree of agglomeration that was observed on TEM images. Peak splitting and shifts for CO oxidation peak have been

studied in acidic media for Pt, where the effect was ascribed to agglomeration [124]. This shift however is only present in alkaline solution, which could suggest that these shifts are promoted by the support material. In Figure 4, a comparison of CVs of different Pd loading on ECS-004601 is displayed in both alkaline and acidic environments. Since higher loading promotes agglomeration then similar negative peak shifts as discussed earlier can also be seen when increasing the Pd loading. ESA values were calculated assuming that scanning of potential to 1.4 V creates a monolayer of PdO and thus integrating the area under the reduction peak of PdO and dividing by its corresponding charge density (424 μC cm^{-2}) [125].

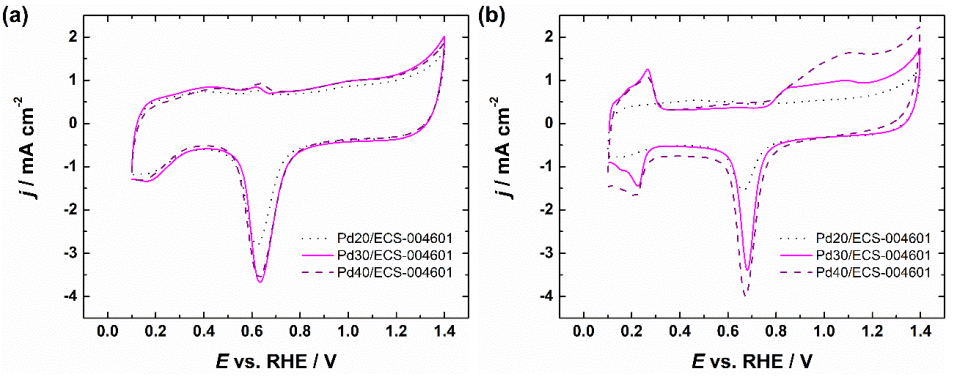

Figure 4. (a) CV curves of Pd/C catalysts in Ar-saturated (a) 0.1 M KOH and (b) 0.5 M H_2SO_4 solutions, v = 50 mV s^{-1}.

6.1.3 ORR in 0.5 M H_2SO_4 on Pd/ECS catalyst materials

After CV and CO-stripping studies, the electrodes were moved to O_2-saturated solution for ORR studies. Potential was scanned between 0.1 and 0.95 V at 10 mV s^{-1}. RDE polarisation curves for a 30% Pd loaded ECS-003604 catalyst are provided in Figure 5. Slightly lower than theoretical limiting current densities are observed, which has been attributed to Nafion film in the literature [126].

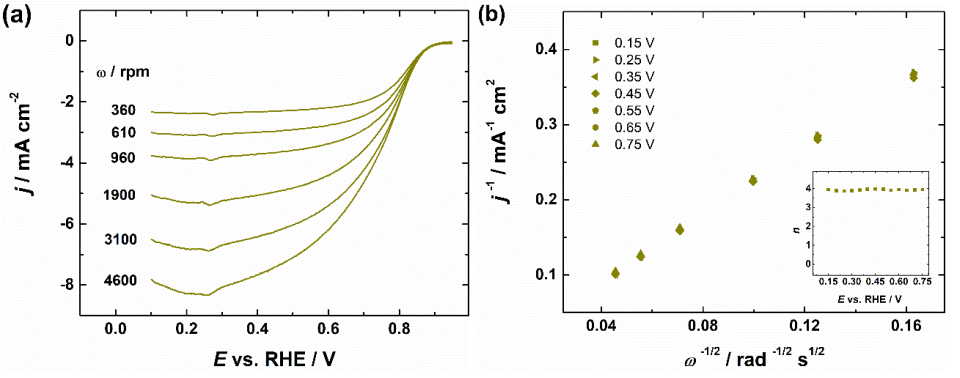

Figure 5. (a) RDE polarisation curves for oxygen reduction on a Pd30/ECS-003604 catalyst at various rotation rates in O_2-saturated 0.5 M H_2SO_4 solution. v = 10 mV s^{-1}. (b) K-L plots for ORR (data derived from a). The inset shows the potential dependence of n.

The RDE polarisation data was analysed using Eq. (7), and calculated n values were close to 4 (inset to Figure 5b), which suggest predominantly a $4e^-$ pathway for ORR on these catalysts.

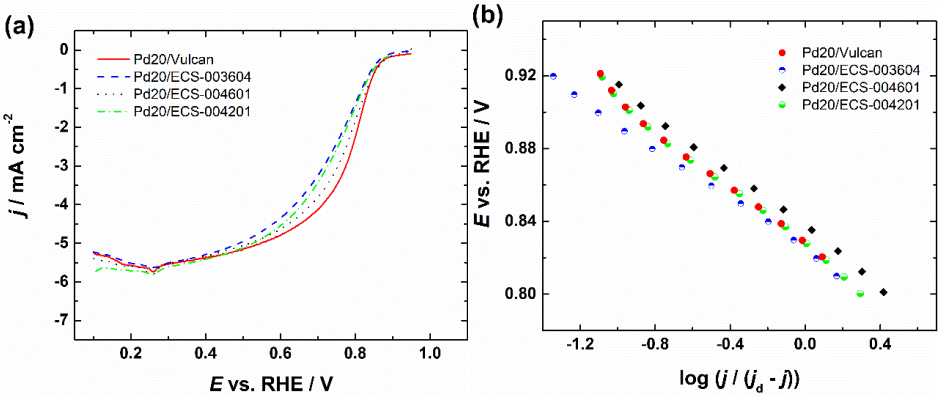

Figure 6. (a) Comparison of RDE results for ORR in O_2-saturated 0.5 M H_2SO_4 solution on 20 wt% Pd/C catalysts. (b) Mass-transfer corrected Tafel plots for ORR, data derived from (a). ω = 1900 rpm, v = 10 mV s^{-1}. Current densities are normalised to the geometric area of GC.

In Figure 6a a comparison of the ORR results for 20% Pd loading is presented for all supports with corresponding Tafel plots displayed in Figure 6b. Tafel slopes between –60 and –80 mV were observed in 0.5 M H_2SO_4. Pd nanoparticles supported on Vulcan carbon exhibit the highest $E_{1/2}$ out of all the materials, which might be due to their higher ESA values. Similarly, all the catalyst materials exhibit an increase in the ESA value (Table 1) when the Pd loading is increased.

Table 1. Kinetic parameters for ORR on Pd/C materials with varied Pd loadings in 0.5 M H_2SO_4. ω = 1900 rpm.

Catalyst	ESA (cm^2)	$E_{1/2}$ (V)	SA at 0.85 V (mA cm^{-2})	Tafel slope (V)
Pd20/Vulcan	2.07	0.78	0.042	–0.079
Pd30/Vulcan	2.67	0.80	0.059	–0.076
Pd40/Vulcan	3.28	0.81	0.063	–0.069
Pd20/ECS-003604	1.60	0.73	0.049	–0.064
Pd30/ECS-003604	2.67	0.75	0.036	–0.079
Pd40/ECS-003604	2.72	0.78	0.077	–0.074
Pd20/ECS-004601	1.96	0.76	0.050	–0.073
Pd30/ECS-004601	2.02	0.79	0.063	–0.063
Pd40/ECS-004601	2.98	0.79	0.057	–0.072
Pd20/ECS-004201	1.75	0.73	0.044	–0.076
Pd30/ECS-004201	2.17	0.76	0.069	–0.067
Pd40/ECS-004201	2.74	0.79	0.083	–0.070

In order to compare intrinsic activity of these catalysts the SA values for ORR were calculated using Eq. (8). Generally specific activity is lower at lower Pd loadings, which suggests agglomeration, as it has been shown that larger particles have higher SA values [36]. From the studied ECS materials the ECS-004601 shows similar increase of SA to Vulcan carbon, while bimodal ECS-004201 support shows improved activity. Nitrogen-doped mesoporous carbons have shown to have higher activity when compared to undoped materials, however, the pore size distribution within the mesoporous carbon material has not been discussed [67]. Synergistic effects have been reported by Guo et al. with non-doped carbon showing lower activity but diffusion limited currents suggest other issues that might affect the activity of the catalysts besides N-doping [127]. Nitrogen-doped graphene as a catalyst support has been reported to reduce the energy barrier for O_2 dissociation [128], but due to much higher activity of metal nanoparticles as compared to N-doped carbon in acidic solutions [129] the likelihood of reaction occurring on the support is very low. Another claim to increased activity for the N-doped carbon supports is attributed to their ability to facilitate more anchoring sites for Pd nanoparticles leading to better dispersion of PdNPs [88, 130]. Increase in support conductivity due to N-doping leading to improved ORR activity has also been suggested [131]. Increase in activity due to presence of atomic Pd-N sites has been studied where significant proportion of activity increase was attributed to these sub-nanometre Pd sites [66, 70].

6.1.4 ORR in 0.1 M KOH on Pd/ECS catalyst materials

ORR polarisation curves for a Pd30/ECS-003604 catalyst in 0.1 M KOH are provided in Figure 7a with corresponding K-L plots in Figure 7b.

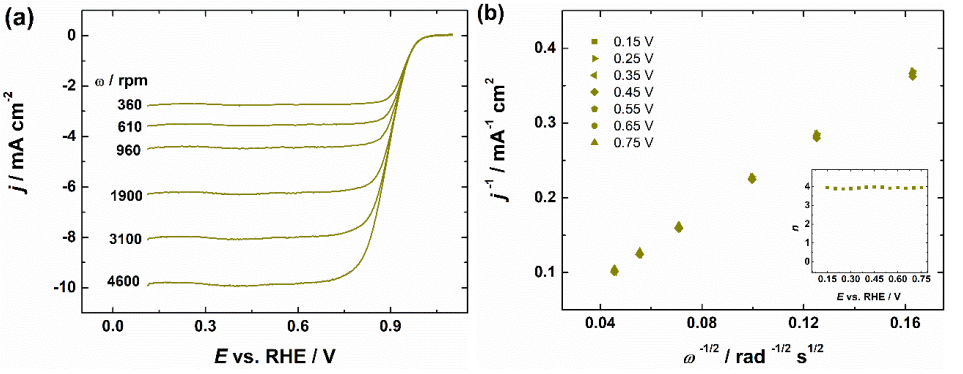

Figure 7. (a) RDE polarisation curves for oxygen reduction on a Pd30/ECS-003604 catalyst at various rotation rates in O_2-saturated 0.1 M KOH solution. $v = 10$ mV s^{-1}. (b) K-L plots for ORR (data derived from a). The inset shows the potential dependence of n.

Using the K-L analysis the n values were calculated by Eq. (7) and these values are shown in the inset of Figure 7b. The K-L analysis for all the materials gave n values close to four which suggests a $4e^-$ ORR pathway.

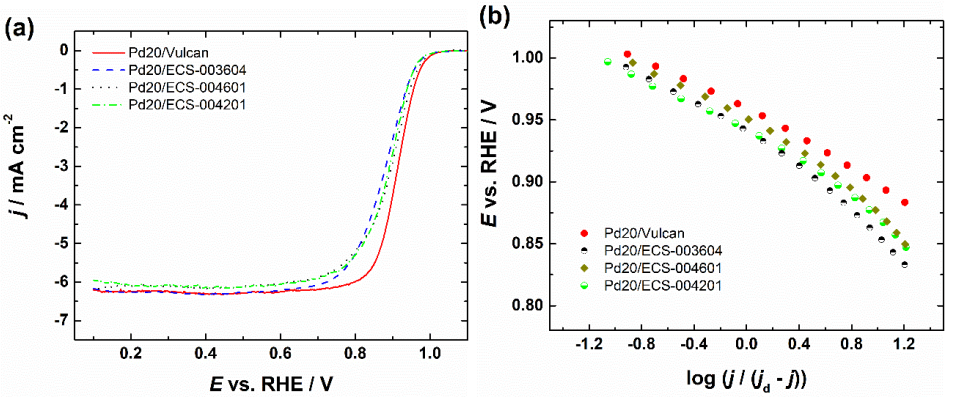

Figure 8. (a) Comparison of RDE results for ORR in O_2-saturated 0.1 M KOH solution on Pd/C catalysts. (b) Mass-transfer corrected Tafel plots for ORR, data derived from (a). ω = 1900 rpm, v = 10 mV s^{-1}. Current densities are normalised to the geometric area of GC.

20% Pd-loaded catalysts were compared in 0.1 M KOH and this comparison is displayed in Figure 8a with the corresponding Tafel plots in Figure 8b. SA values calculated using Eq. (8) are provided in Table 2.

Table 2. Kinetic parameters of ORR for Pd/C catalysts with different loadings in 0.1 M KOH. ω = 1900 rpm.

Catalyst	ESA (cm^2)	$E_{1/2}$ (V)	SA at 0.95 V (mA cm^{-2})	Tafel slope (V)
Pd20/Vulcan	3.18	0.91	0.081	–0.065
Pd30/Vulcan	3.50	0.92	0.092	–0.060
Pd40/Vulcan	3.94	0.92	0.078	–0.068
Pd20/ECS-003604	2.08	0.88	0.064	–0.072
Pd30/ECS-003604	2.57	0.89	0.076	–0.078
Pd40/ECS-003604	3.14	0.91	0.073	–0.065
Pd20/ECS-004601	2.75	0.90	0.068	–0.070
Pd30/ECS-004601	3.54	0.91	0.071	–0.061
Pd40/ECS-004601	3.95	0.91	0.078	–0.077
Pd20/ECS-004201	1.69	0.89	0.080	–0.061
Pd30/ECS-004201	1.83	0.89	0.077	–0.065
Pd40/ECS-004201	2.55	0.90	0.082	–0.067

The SA values determined in alkaline solution show a significantly lower variation between the materials as compared to the results obtained in H_2SO_4. As a support material the bimodal ECS-004201 outperforms the unimodal

ECS-004601 in terms of specific activity, but ESA values for these materials differ greatly, which might play a role in the SA difference. Analogously to acidic conditions, the Tafel slope values vary between –60 and –80 mV. –60 mV Tafel slope is suggested to correspond to Pd catalyst covered by oxides [132] with rate-determining step being the transfer of the first electron to the O_2 molecule [22, 133]. Higher slope values observed in this work could suggest that N-doping reduces the oxide coverage of Pd, which could result in higher Tafel slope values. Similarly, higher Tafel slope values have been attributed to lower oxide coverage in case of Pd nanocubes [134].

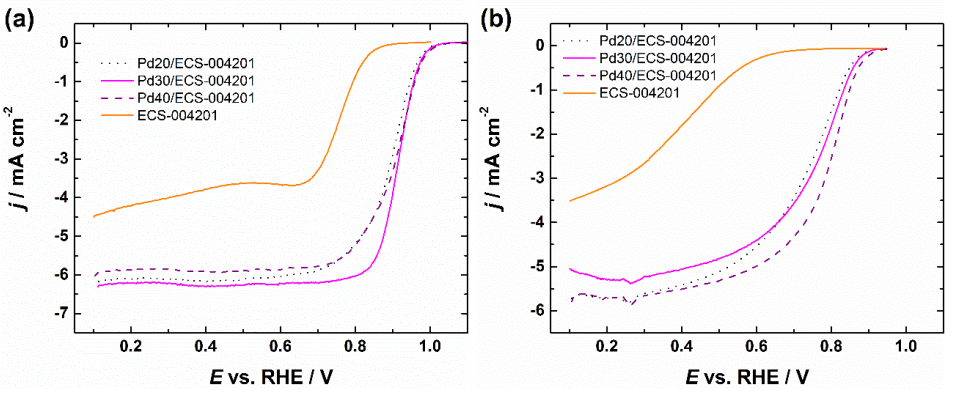

Figure 9. Comparison of RDE results for ORR on Pd/ECS-004201 catalysts of various Pd loading in (a) O_2-saturated 0.1 M KOH and (b) 0.5 M H_2SO_4 solutions. ω = 1900 rpm, v = 10 mV s^{-1}. Current densities are normalised to the geometric area of GC.

Figure 9 presents the electrochemical ORR behaviour of different loadings of Pd on the ECS-004201 support in both alkaline (9a) and acidic (9b) media. A slight increase in $E_{1/2}$ can be observed with increasing Pd loading. Furthermore, by comparing these support materials with Pd/C materials a significant increase in ORR activity can be observed in both alkaline and especially in acidic conditions.

6.1.5 AEMFC single cell testing with Pd40/ECS-003604 cathode

AEMFC single cell comparison for 40% Pd loading on Vulcan and ECS-003604 are provided in Figure 10. By comparing the peak power density (P_{max}) values between these two materials it is evident that significant increase on engineered carbon support can be observed. Since the Pd particles for both catalysts have same size, the increase could be attributed to either mesoporosity or N-doping of the support. Mesoporosity could provide better mass transport, while N-doping could facilitate better Pd particle dispersion on the catalyst and provide better AEMFC performance. Similar P_{max} increase has been previously noted on N-doped graphene supported Pd catalyst when comparing to Pd/Vulcan as P_{max} increased from 189 to 250 mW cm^{-2} [135]. By comparing undoped Pd/CNT and Pd/Vulcan the P_{max} increase from 26.2 to 42 mW cm^{-2} could be observed [136].

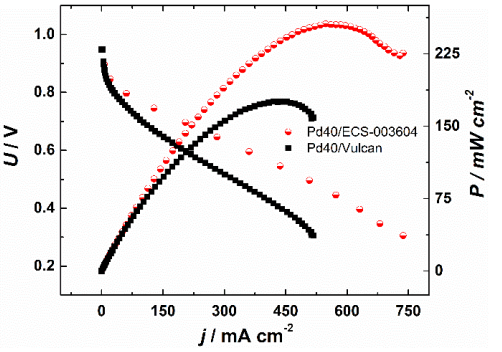

Figure 10. Single cell AEMFC polarisation and power density curves with Pd40/ECS-003604 and Pd40/Vulcan cathodes (loading 0.4 mg_{Pd} cm^{-2}) and HMT-PMBI AEM. The anode was a commercial PtRu/C (loading 0.8 mg_{PtRu} cm^{-2}). T = 60 °C, 100% RH, backpressure = 200 kPa.

6.2 Oxygen reduction on cubic PdNPs supported on Vulcan carbon

In this part of the work cubic PdNPs were studied on Vulcan carbon support [II, III]. Three different sized Pd nanocubes (~30, ~10 and ~7 nm) were studied. The catalysts prepared with a loading of 20% Pd are named PdCub1-20, PdCub2-20, PdCub3-20 for ~30, ~10 and ~7 nm Pd nanocubes, respectively. With ~30 nm cubes 50% loading was also tested (PdCub1-50). These results were compared to 2–5 nm spherical particles PdSph-20 with 20 wt% Pd.

6.2.1 Physical characterisation of cubic Pd/C catalysts

In Figure 11 a set of TEM images of Pd nanocubes supported on Vulcan carbon can be seen. Majority of these Pd particles have cubic shape. Size of the particles depends on the chosen synthesis method with sizes being about 30 nm for synthesis that used CTAB while 10 and 7 nm particles used the PVP method. Spherical Pd particles prepared using citrate method with sizes around 2–5 nm can be seen in Figure 11d. The particles prepared by the CTAB method have been previously studied without carbon support [25, 90, 137], so we can safely assume that the prevailing crystal facet on these nanoparticles is Pd(100).

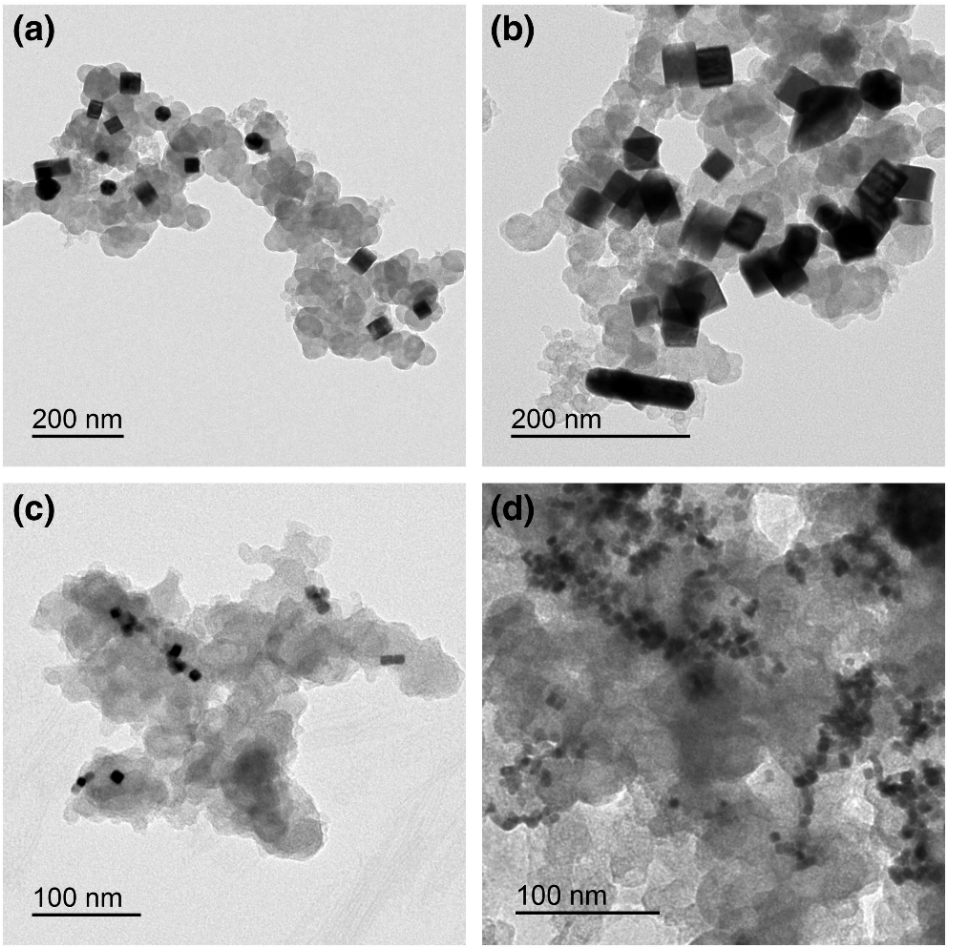

Figure 11. TEM images of carbon-supported Pd nanocubes (a) PdCub1-20, (b) PdCub1-50, (c) PdCub2-20 and (d) PdCub3-20.

6.2.2 CO-stripping and CV studies on cubic Pd/C catalysts

Before the ORR experiments, the electrocatalyst materials were cleaned and characterised with cyclic voltammetry and using CO adsorption followed by its electro-oxidation. CO was oxidised by scanning up to 1 V, which resulted in a peak at around ~0.8 V. For ESA calculation the electrodes were cycled between 0.1 and 1.4 V. Typical CV curves for Pd nanocubes can be seen in Figure 12, similar cyclic voltammograms have been observed in alkaline solution in the previous part of this thesis [II]. Slight shift of PdO reduction peak to more negative potentials with decreasing the Pd particle size can be observed. This could be explained similarly to previous work, where it was found that the smaller Pd particles adsorb OH^- ions more strongly [36].

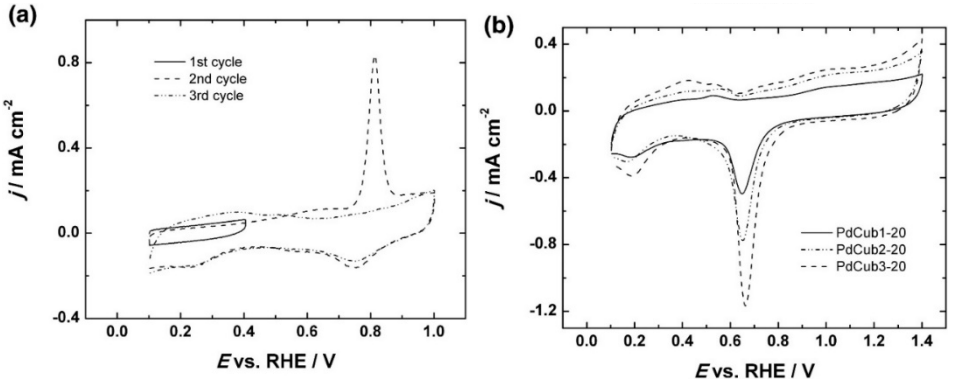

Figure 12. (a) Electro-oxidation of pre-adsorbed CO on PdCub3-20, $v = 20$ mV s^{-1}. (b) CVs of carbon-supported Pd nanocubes in Ar-saturated 0.1 M KOH, $v = 50$ mV s^{-1}. Current densities are normalised to the geometric area of GC.

6.2.3 Oxygen reduction in 0.1 M $HClO_4$ on cubic Pd/C catalysts

RDE data comparison with corresponding Tafel plots can be seen in Figure 13. The n values calculated using Eq. (7) were close to 4 for all of the catalysts studied.

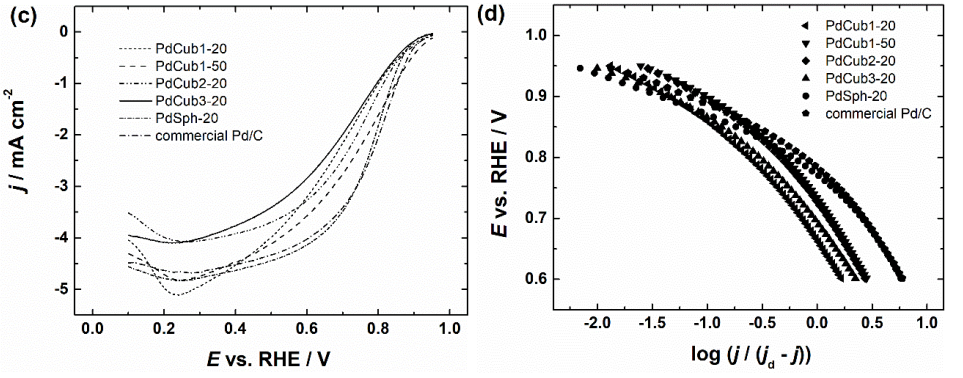

Figure 13. (a) Comparison of RDE voltammetry curves for ORR on Pd/C catalysts in O_2-saturated 0.1 M $HClO_4$ and (b) the corresponding Tafel plots. $\omega = 1900$ rpm, $v = 10$ mV s^{-1}.

By comparing the polarisation curves of different Pd loading we can see an obvious increase in onset and half-wave potential values. Half-wave potentials follow the order: PdCub1-20 < PdCub3-20 ≈ PdCub2-20 < PdCub1-50 < PdSph-20, which is dependent on the Pd particle size, since smaller particles have higher ESA value at similar loading.

For better comparison of the ORR activity between these catalysts the values of SA are calculated using Eq. (8). By comparing the SA values of PdCub1-20 and PdCub1-50 we can conclude that the SA values are independent of Pd loading. The ORR kinetic parameters in Table 3 indicate that the SA values for PdCub1

are higher than those of PdCub2 and PdCub3. This, however, could be explained by the particle size effect, since it has been shown that larger particles tend to have higher specific activity [38, 85]. Another reason for the lower activity of smaller particles may be due to varying proportion of the most active (100) facets that may be lower in case of smaller nanocubes due to truncations. Third possible reason for the lower activity of Pd nanocubes prepared by PVP method is insufficient removal of PVP. If PVP is not completely removed from the catalyst surface it can block the active sites and reduce the accessibility of O_2 molecules to PdNP sites [138]. Around 2 times higher specific activity can be observed for cubic PdNPs (PdCub1-20, 0.20 mA cm^{-2}**)** in comparison to spherical particles PdSph-20 (0.08 mA cm^{-2}), which can be attributed to smaller size of spherical particles and different surface crystallography. When comparing cubic particles in $HClO_4$ solution Shao et al. showed 10 times activity difference between cubic and octahedral particles, which reinforces notion of this activity increase being due to shape control [134]. To further evaluate the ORR activity of these particles the MA values were also calculated. Mass activities follow the trend of smaller particles to have higher mass activity. However, the catalyst with 50% Pd loading showed lower MA suggesting poor Pd utilisation at such high loadings.

Table 3. Kinetic parameters for oxygen reduction on Pd/C catalysts in 0.1 M $HClO_4$. ω = 1900 rpm.

Catalyst	Tafel slope (mV)	$E_{1/2}$ (V)	SA at 0.85 V (mA cm^{-2})	MA at 0.85 V (A g^{-1})
PdCub1-20	–136	0.65	0.24	26
PdCub1-50	–140	0.74	0.27	21
PdCub2-20	–138	0.69	0.18	28
PdCub3-20	–120	0.69	0.16	29
PdSph-20	–124	0.77	0.12	37
comm. Pd/C	–124	0.78	0.13	34

Two regions of different Tafel slope values were distinguished. Tafel slopes at low current densities were near –90 mV but increased to above –120 mV at higher current densities. Slope value for spherical PdNPs and commercial Pd/C was around –65 mV, which increased to –120 mV in high current density ranges. The obtained Tafel slope values for non-spherical particles are somewhat higher than the usually observed –120 mV, however unsupported Pd nanocubes have previously given slope values of up to –150 mV [25]. Higher values in the low current density region might be due to lower oxide coverage of these particles similar to discussion in [I]. Lower oxide coverage on Pd nanocubes was also noted by Shao et al., when observing oxygen-containing species on Pd nanocubes and octahedra [134]. Generally, the Tafel slope values close to –120 mV suggest that electrode is free from PdO and the ORR proceeds with rate-limiting step being transfer of the first electron to O_2 molecule [22, 25, 133].

6.2.4 Oxygen reduction in 0.1 M KOH on cubic Pd/C catalysts

Typical RDE results for PdCub3-20 obtained in 0.1 M KOH are provided in Figure 14a. Eq. (7) was used to obtain the K-L plots (Figure 14b), with the inset of Figure 14b displaying *n*-*E* dependence. Current density plateaus observed in Figure 14c are slightly lower than those observed for bulk Pd [25], which could be attributed to Nafion [126] as it has been show that Nafion promotes 2-electron ORR and thus decreases limiting current density. Tafel plots derived from the RDE data are presented in Figure 14d. The variations observed in the diffusion-limited currents can be attributed to uneven thickness of the catalyst layer or geometric area of the electrode.

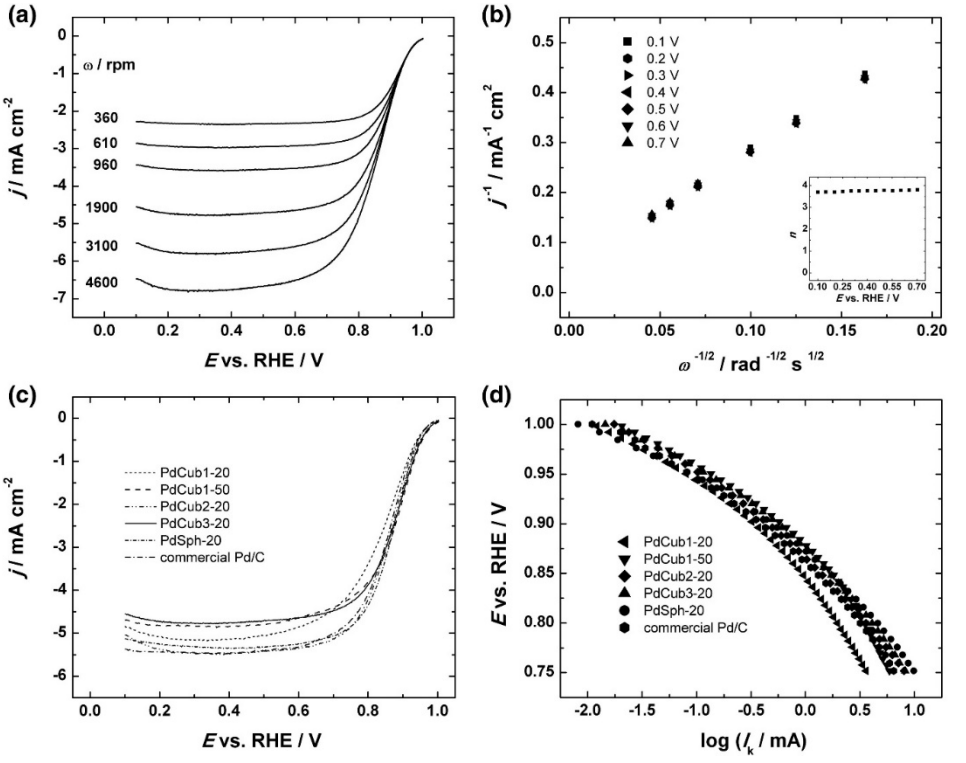

Figure 14. (a) A set of RDE results of PdCub3-20 in O_2-saturated 0.1 M KOH and (b) corresponding K–L plots, inset shows the potential dependence of *n*. (c) Comparison of RDE voltammetry curves for oxygen reduction on Pd/C catalysts in O_2-saturated 0.1 M KOH and (d) corresponding Tafel plots, ω = 1900 rpm, v = 10 mV s^{-1}.

Half-wave potentials follow the order: PdCub1-50 > PdCub3-20 > PdCub2-20 ≈ PdSph-20 ≈ commercial Pd/C > PdCub1-20. Both SA and MA values were calculated according to Eqs. (8) and (9), respectively. The SA values at 0.9 V increased in the following order: PdSph-20 (0.15 ± 0.08 mA cm^{-2}) < commercial Pd/C (0.21 ± 0.09 mA cm^{-2}) < PdCub3-20 (0.37 ± 0.10 mA cm^{-2}) < PdCub2-20 (0.42 ± 0.05 mA cm^{-2}) < PdCub1-50 (0.50 ± 0.08 mA cm^{-2}) < PdCub1-20

(0.55 ± 0.08 mA cm^{-2}). Threefold increase of SA values can be observed for PdCub1-20 as compared to spherical particles. Lower SA values for PdCub2-20 and PdCub3-20 might be due to truncation or smaller particle size. Lower SA values of spherical particles are in good agreement with literature [25]. However, contradicting results have been obtained by Shao et al. in alkaline solution where no structural dependence between Pd nanocubes, octahedra and conventional spherical particles was observed [31]. It has also been shown that the SA increases with the Pd particle size [36] in which case the activity increase could be either attributed to increase in particle size and/or to the relative amount of Pd(100) crystal facets. The MA values at 0.9 V decreased in the order of PdSph-20 (101 ± 13 A g^{-1}) > PdCub3-20 (87 ± 16 A g^{-1}) ≈ commercial Pd/C (87 ± 12 A g^{-1}) > PdCub2-20 (62 ± 11 A g^{-1}) > PdCub1-20 (59 ± 12 A g^{-1}) > PdCub1-50 (38 ± 9 A g^{-1}), which similarly to acidic conditions follow the particle sizes, and like in acid a lower mass activity can be observed for 50 wt% Pd catalyst due to poor Pd utilisation. However, the mass activity of commercial Pd/C was matched by PdCub3-20. It has been reported that Pd/C in alkaline media has a maximum MA at ~5 nm particle size [36] suggesting that further optimisation of these nanocubes could be done.

To further analyse the RDE data Tafel plots were constructed. In alkaline media the Tafel slope values were around –65 mV at low current densities and –120 mV at high current densities, suggesting that no change in the reaction mechanism or oxide coverage of these catalysts occurred in the potential regions chosen for analysis as these are typical Tafel slope values as reported in literature [25, 27, 30, 36, 133].

6.3 ORR on Pd/CDC electrocatalysts

Due to their tuneable porosity CDC materials could provide an opportunity to optimise the dispersion and accessibility of Pd particles for ORR [IV]. Within this part, 4 different CDC materials were studied as Pd catalyst supports, where Pd particles were prepared with simple borohydride reaction. The CDCs were prepared from TiC, Mo_2C and SiC. With CDC1 and CDC2 being from TiC, CDC4 from Mo_2C and CDC5 from SiC. These CDC-supported Pd catalyst materials were studied in 0.1 M KOH and 0.1 M $HClO_4$ solutions.

6.3.1 Study of textural properties of Pd/CDC materials

The initial specific surface areas of these CDC materials were measured: CDC1 (S_{BET}=1493 $m^2\,g^{-1}$), CDC2 (S_{BET}=1997 $m^2\,g^{-1}$), CDC4 (S_{BET}=1735 $m^2\,g^{-1}$), CDC5 (S_{BET}=1548 $m^2\,g^{-1}$). Since the CDC particles were too large to apply as catalyst support materials, they were ball-milled to reduce their grain size, however this process destroys some of the micro- and mesoporosity of these supports. After ball-milling and Pd deposition the measured BET surface areas were: Pd/CDC1

(S_{BET}=355 m^2 g^{-1}), Pd/CDC2 (S_{BET}=517 m^2 g^{-1}), Pd/CDC4 (S_{BET}=365 m^2 g^{-1}) and Pd/CDC5 (S_{BET}=746 m^2 g^{-1}). Pore size distribution (PSD) graphs for these Pd catalysts are provided in Figure 15. From PSD graph we can see that all of these materials are microporous with very small sub 1 nm pores but Pd/CDC5 has higher number of larger 1–3 nm pores available.

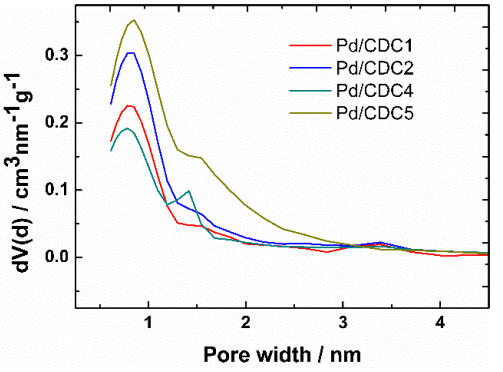

Figure 15. Pore size distribution of Pd/CDC samples.

6.3.2 Raman analysis of Pd/CDC materials

First-order Raman spectra of Pd/CDC materials are provided in Figure 16. Raman spectra were first normalised to the intensity of G peak and then fitted according to the recommendation of Sadezky et al. [139] with four curves: three Lorentzian (D4~1180 cm^{-1}, D1~1350 cm^{-1}, G~1580 cm^{-1}) and one Gaussian peak (D3~1500 cm^{-1}). The I_{D1}/I_G ratio values were calculated for Pd/CDC1 (1.83), Pd/CDC2 (1.60), Pd/CDC4 (1.64), Pd/CDC5 (2.01) and Pd/Vulcan (1.79). The D bands were analysed with D1 corresponding to high number of defects and disorder and D3 and D4 are associated with amorphous carbon [140]. The I_{D1}/I_G ratio suggests the presence of high level of disorder and defects on all of these catalyst materials.

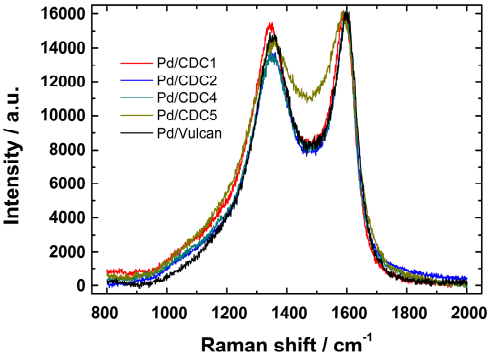

Figure 16. Raman spectra of Pd/CDC materials.

6.3.3 Surface characterisation of Pd/CDC materials

SEM images in Figure 17 show that Pd/CDC4 catalyst displays higher degree of agglomeration in comparison to the rest of the catalysts. From less zoomed versions of these images also larger CDC particles could be seen that milling was uneven and some larger CDC particles were present (up to 6 μm in case of CDC4 and CDC5 and up to 2 μm in case of CDC1 and CDC2). From SEM images Pd particle sizes of around 8 nm could be observed on all CDC materials.

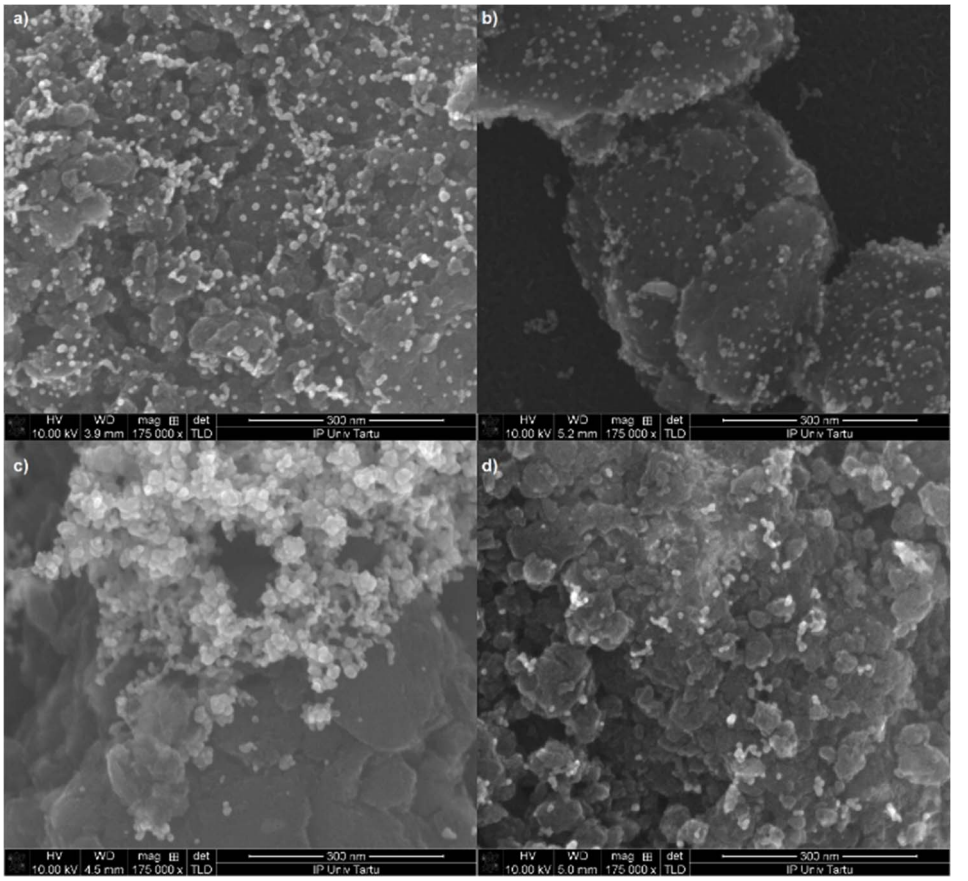

Figure 17. SEM images of (a) Pd/CDC1, (b) Pd/CDC2, (c) Pd/CDC4 and (d) Pd/CDC5 samples.

For better particle size determination, the TEM images were obtained. Average particle sizes counted from Figure 18 are listed in Tables 4 and 5. Best dispersion of Pd nanoparticles was observed on Pd/CDC2 catalyst, which can be due to higher amount of smaller micropores, where the deposition of metal can occur. Similar effect has been also observed by Kumar et al. who showed that lower number of micropores result in agglomerated Pd particles [49].

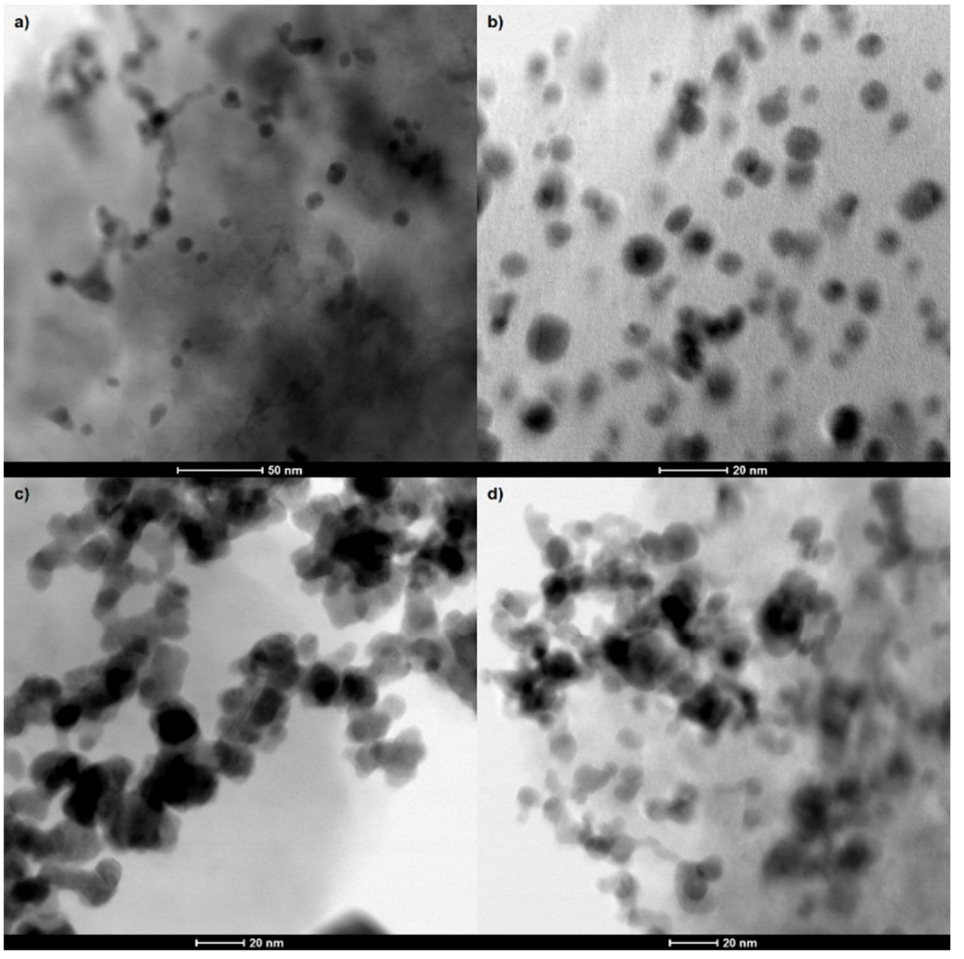

Figure 18. TEM images of (a) Pd/CDC1, (b) Pd/CDC2, (c) Pd/CDC4 and (d) Pd/CDC5 samples.

6.3.4 Thermogravimetry and MP-AES of Pd/CDC materials

TGA curves for Pd/CDC5 in comparison to Pd/Vulcan are provided in Figure 19. We can see that higher than 20% of mass remained, which can be attributed to ZrO_2 introduced during intensive ball-milling process. For this reason, MP-AES was used to evaluate the true Pd content in all these materials. The Pd content of the catalysts were following: Pd/CDC1 19.2%, Pd/CDC2 22.8%, Pd/CDC4 15.7%, Pd/CDC5 20.8% and Pd/Vulcan 16.2%.

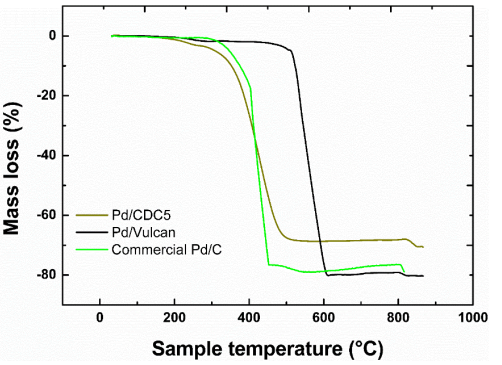

Figure 19. TGA curves of CDC5 and Vulcan carbon-supported palladium catalysts in comparison to commercial Pd/C catalyst.

6.3.5 CV and CO-stripping studies of Pd/CDC materials

Similarly, to previous parts of this thesis [I,II and III] CV and CO-stripping was employed for surface characterisation and cleaning. Typical cyclic voltammetry profiles for Pd catalysts in both alkaline (Figure 20a) and acidic media (Figure 21a) were observed.

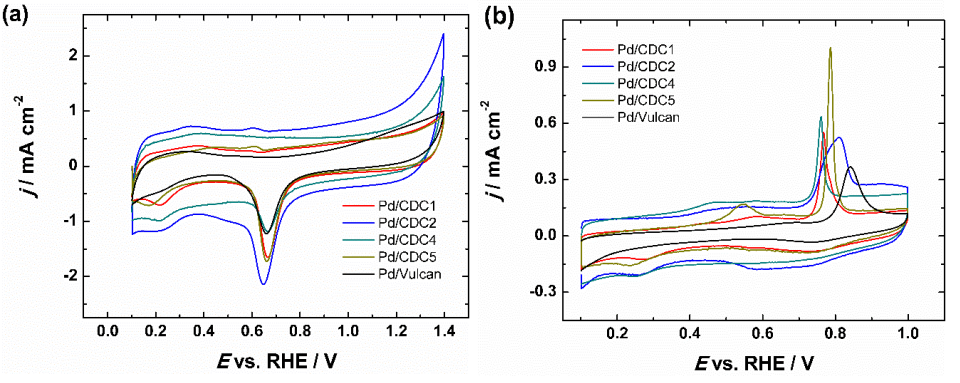

Figure 20. (a) Cyclic voltammograms of Pd/C catalysts in Ar-saturated 0.1 KOH solution, v = 50 mV s^{-1} and (b) electro-oxidation of pre-adsorbed CO, v = 10 mV s^{-1}.

Within this part of the work the value of ESA was also calculated using the CO oxidation peak. There was a good agreement between the ESA values calculated from CV and CO-stripping peaks, so only ESA values determined from the cyclic voltammograms are provided in Tables 4 and 5. Similarly, to work done on Pajarito Powder engineered catalyst supports [I] we can observe that the CO-stripping peak in alkaline solution is shifted (Figure 20b), while in acidic media (Figure 21b) it remains same. There should not be any crystallographic difference between the obtained catalysts in both works (since ECS-supported Pd particles were prepared using one-pot method) and the N-doping is present in only in part

(section 6.1) of this work, these shifts are most likely due to the porosity of the support material. Furthermore, crystallographic differences between Pd particles should be visible in the CO-stripping study in acidic conditions [141]. In Table 5 the lower ESA value of Pd/CDC4 is reflective of the agglomeration of Pd particles observed during the SEM studies.

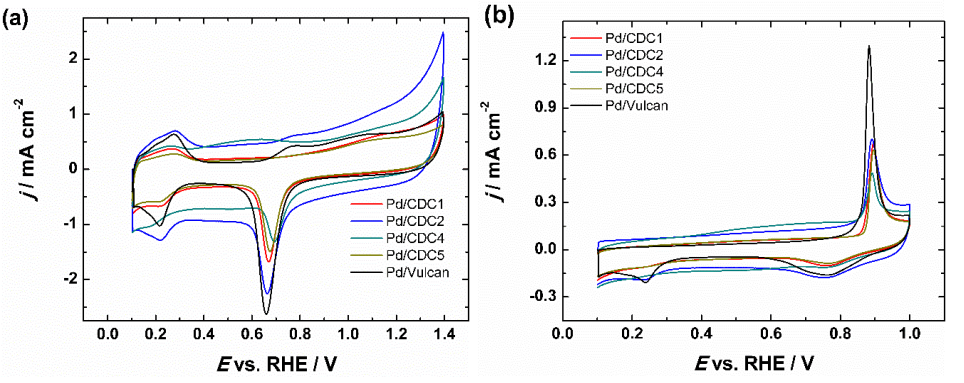

Figure 21. (a) Cyclic voltammograms of Pd/CDC catalysts in Ar-saturated 0.1 M $HClO_4$ solution, v = 50 mV s^{-1} and (b) electro-oxidation of pre-adsorbed CO, v = 10 mV s^{-1}.

6.3.6 Oxygen reduction in 0.1 M $HClO_4$ on Pd/CDC materials

The K-L analysis was used according to Eq. (7). All of the catalysts showed the n value close to 4 suggesting predominantly a 4-electron pathway for the ORR. Slightly lower n values in the presence of Nafion have been previously noted since on Nafion the ORR proceeds through $2e^{-}$+$2e^{-}$ pathway [126, 142].

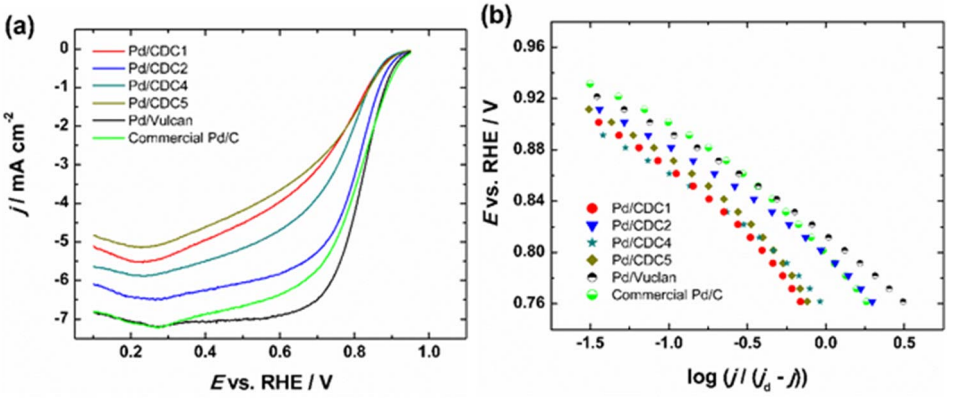

Figure 22. (a) Comparison of RDE results for ORR in O_2-saturated 0.1 M $HClO_4$ solution on Pd/CDC and Pd/C catalysts. (b) Mass-transfer-corrected Tafel plots for ORR (data derived from a). ω = 1900 rpm, v = 10 mV s^{-1}.

Comparison between the catalyst materials at a single electrode rotation rate in perchloric acid solution can be found in Figure 22a with corresponding Tafel plots in Figure 22b.

Table 4. Kinetic parameters for ORR on different Pd/C catalysts in 0.1 M $HClO_4$ solution. ω = 1900 rpm.

Catalyst	Particle size (nm)	ECSA (cm^2)	SA at 0.9 V (mA cm^{-2})	Tafel slope (mV)	$E_{1/2}$ (V)
Pd/CDC1	7.9 ± 1.9	1.04 ± 0.12	0.035 ± 0.006	–76 ± 7	0.721 ± 0.009
Pd/CDC2	7.3 ± 1.8	1.06 ± 0.04	0.057 ± 0.008	–60 ± 3	0.798 ± 0.002
Pd/CDC4	10.3 ± 2.2	0.60 ± 0.07	0.057 ± 0.002	–76 ± 6	0.769 ± 0.013
Pd/CDC5	9.0 ± 1.4	0.88 ± 0.04	0.055 ± 0.010	–68 ± 3	0.722 ± 0.004
Pd/Vulcan	5.9 ± 1.4	1.25 ± 0.12	0.015 ± 0.005	–57 ± 2	0.82 ± 0.003
Comm. Pd/C[a]	3.5	3.6	0.036	–58	0.80

[a] values taken from [IV]

By comparing the SA values in Table 4, we can see the agglomerated Pd/CDC4 has similar specific activity to Pd/CDC5 and PdCDC2. The SA difference of Pd/CDC1 and Pd/CDC4 can be ascribed to either larger particle size or higher availability of mesopores. Better ORR performance of Pd/CDC2 as compared to Pd/CDC1 might be due to the treatment of the CDC1 material with water vapour. Comparing the CDC4 material which had the lowest number of micropores and highest degree of Pd agglomeration to literature then similar effects have been noted where a collapse of micropores led to Pd agglomeration [49]. The Raman spectra of all the Pd/CDC catalyst materials were rather similar, thus the CDC supports used should be of fairly similar structure. Tafel slope values for these Pd/CDC materials were only determined at low current densities and showed slightly higher values than the usual –60 mV.

6.3.7 Oxygen reduction in 0.1 M KOH on Pd/CDC materials

The *n* values determined for all the Pd/CDC catalysts were close to 4. Different catalysts are compared at the same electrode rotation speed and are provided in Figure 23. Differences in the diffusion-limited currents could be due to differences in the CDC grain sizes, which varied somewhat and thus affect the coverage of the working electrode.

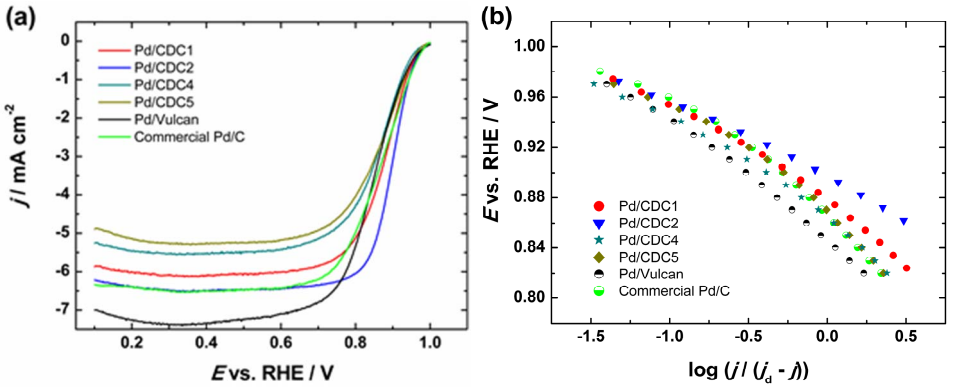

Figure 23. (a) Comparison of RDE results for ORR in O_2-saturated 0.1 M KOH solution on Pd/CDC and Pd/C catalysts. (b) Mass-transfer-corrected Tafel plots for ORR (data derived from a). ω = 1900 rpm, v = 10 mV s^{-1}.

Table 5. Kinetic parameters for ORR on different Pd/C catalysts in 0.1 M KOH solution. ω = 1900 rpm.

Catalyst	Particle size (nm)	ESA (cm^2)	SA at 0.95 V (mA cm^{-2})	Tafel slope (mV)	$E_{1/2}$ (V)
Pd/CDC1	7.9 ± 1.9	1.07 ± 0.11	0.100 ± 0.018	–67 ± 3	0.878 ± 0.003
Pd/CDC2	7.3 ± 1.8	1.06 ± 0.05	0.131 ± 0.014	–61 ± 2	0.896 ± 0.004
Pd/CDC4	10.3 ± 2.2	0.53 ± 0.13	0.159 ± 0.017	–71 ± 4	0.873 ± 0.009
Pd/CDC5	9.0 ± 1.4	1.21 ± 0.09	0.095 ± 0.010	–79 ± 2	0.867 ± 0.006
Pd/Vulcan	5.9 ± 1.4	1.22 ± 0.09	0.086 ± 0.012	–81 ± 4	0.848 ± 0.008
Comm. Pd/C[a]	3.5	3.42	0.04	–92	0.87

[a] values taken from [IV]

Due to PdNP agglomeration, a higher SA could be observed for Pd/CDC4, which had agglomerated Pd particles as seen in SEM images (Figure 17). In an earlier work it has been shown that larger Pd particles have higher SA value [6]. All Pd/CDC catalysts prepared within this part surpassed the SA of commercial Pd/C catalyst, but it might be due to the smaller particle size of the commercial Pd/C, which was around 3.5 nm [V]. $E_{1/2}$ comparison shows that the Pd/Vulcan and Pd/CDC4 possess the lowest values. These results show that higher SA values could be achieved by using CDC as a support material in comparison to conventional carbon black. Similarly, using 3D graphene nanosheets as a Pd catalyst support, a better dispersion of PdNPs could be achieved in comparison to Vulcan carbon [51]. Applying Tafel analysis the slope values about –60 mV could be observed, however with some materials increase to –90 mV could be observed. Higher Tafel slope values have been previously reported for PdNPs supported on carbon materials [3, 25, 143].

6.3.8 Stability testing of Pd/CDC2 electrocatalyst

Stability testing in alkaline solution was carried out with the catalyst that displayed the best ORR performance (Pd/CDC2). Figure 24 shows the ORR polarisation curves measured before and after the 2000 potential cycles between 0.4–0.9 V at 100 mV s^{-1}. After 2000 cycles the catalyst Pd/CDC2 lost about 22% of its ESA and 3.5% of its SA. The $E_{1/2}$ value decreased by 20 mV after stability testing.

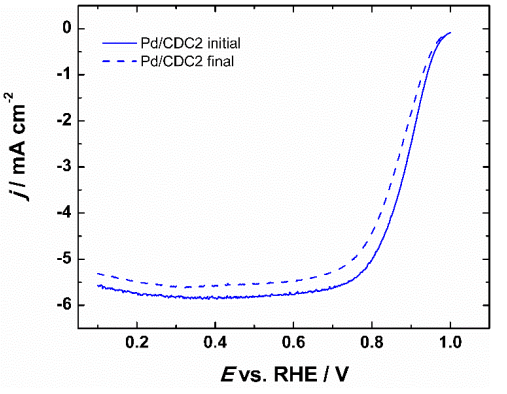

Figure 24. ORR polarisation curves of Pd/CDC2 before and after 2000 potential cycles between 0.4 and 0.9 V in O_2-saturated 0.1 M KOH solution. ν = 10 mV s^{-1}, ω = 1900 rpm.

6.4 Electrodeposited Pd/C as ORR catalyst

In this part of the work Pd was electrodeposited on various carbon supports [V]. Eight different support materials were used and two different deposition pulse potentials were employed. Carbon nanotubes and CNT containing materials were studied as support before electrochemical activation and after electrochemical activation, this activation process was tried out on GNP-CNT support as well. Rest of the supports were Vulcan carbon, graphene nanosheets and graphene nanopellets. Materials were named as Pd/used material with letter 'a' at the end indicating electrochemical activation. Subscript at the end of H or L were used for high and low overpotential deposition, respectively.

6.4.1 SEM and TEM studies of electrodeposited Pd/C

SEM images for the electrodeposited Pd catalysts at higher overpotential are presented in Figure 25. When looking at the Pd deposits on the CNT surface (Figure 25a) the Pd catalyst is concentrated on the defects and ends of CNTs. By comparing these deposits with the ones prepared using lower overpotential, not much difference could be seen (image not shown). On the surface of GNS a more uniform dispersion of Pd spherical particles with very little agglomeration can be observed (Figure 25c), however with TEM some larger dendrites of Pd are present (Figure 26d).

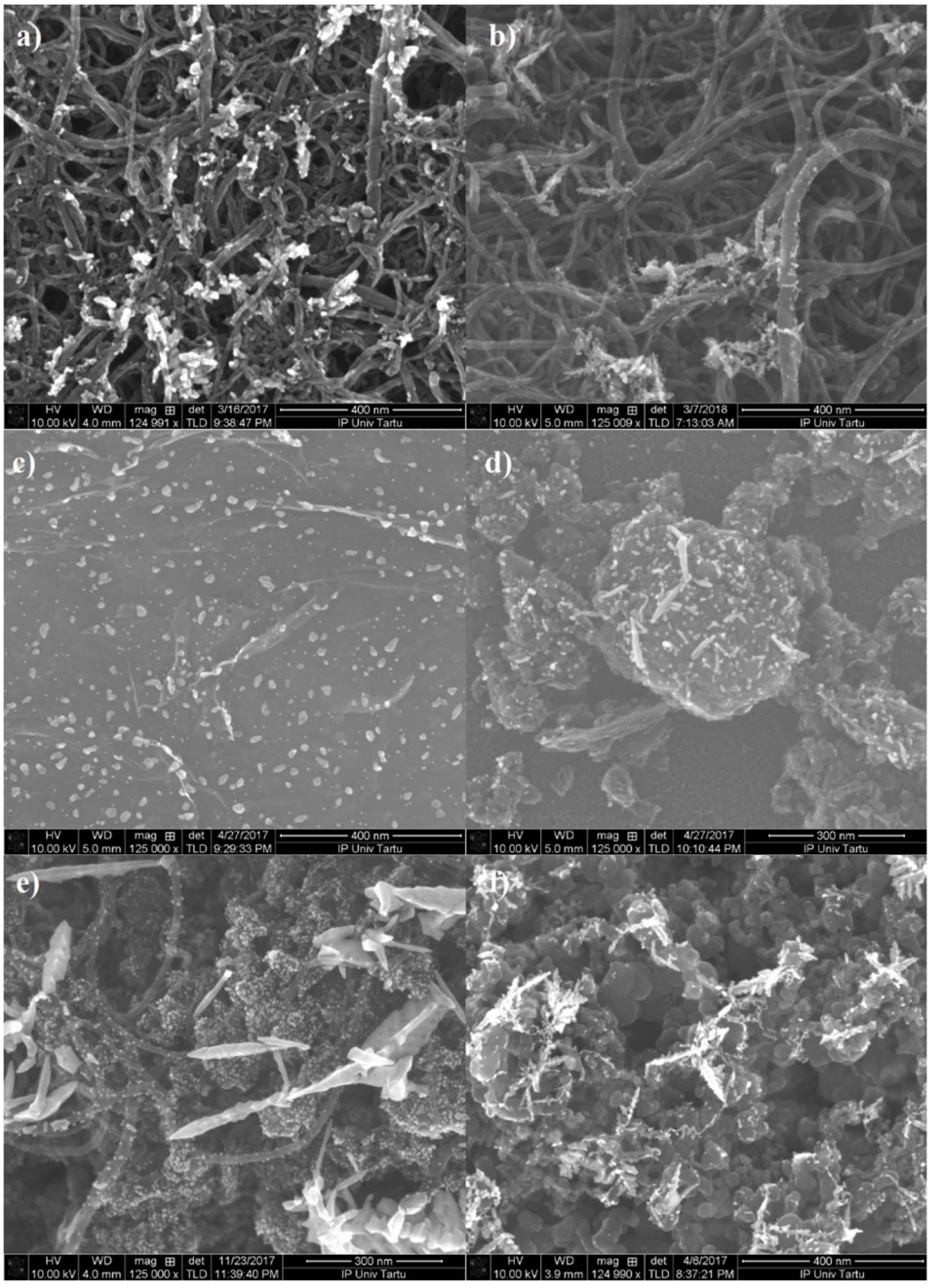

Figure 25. SEM images of: (a) Pd/CNT_H, (b) Pd/$CNTa_H$, (c) Pd/GNS_H, (d) Pd/GNP_H, (e) Pd/CNT-GNP_H and (f) Pd/CB_H samples.

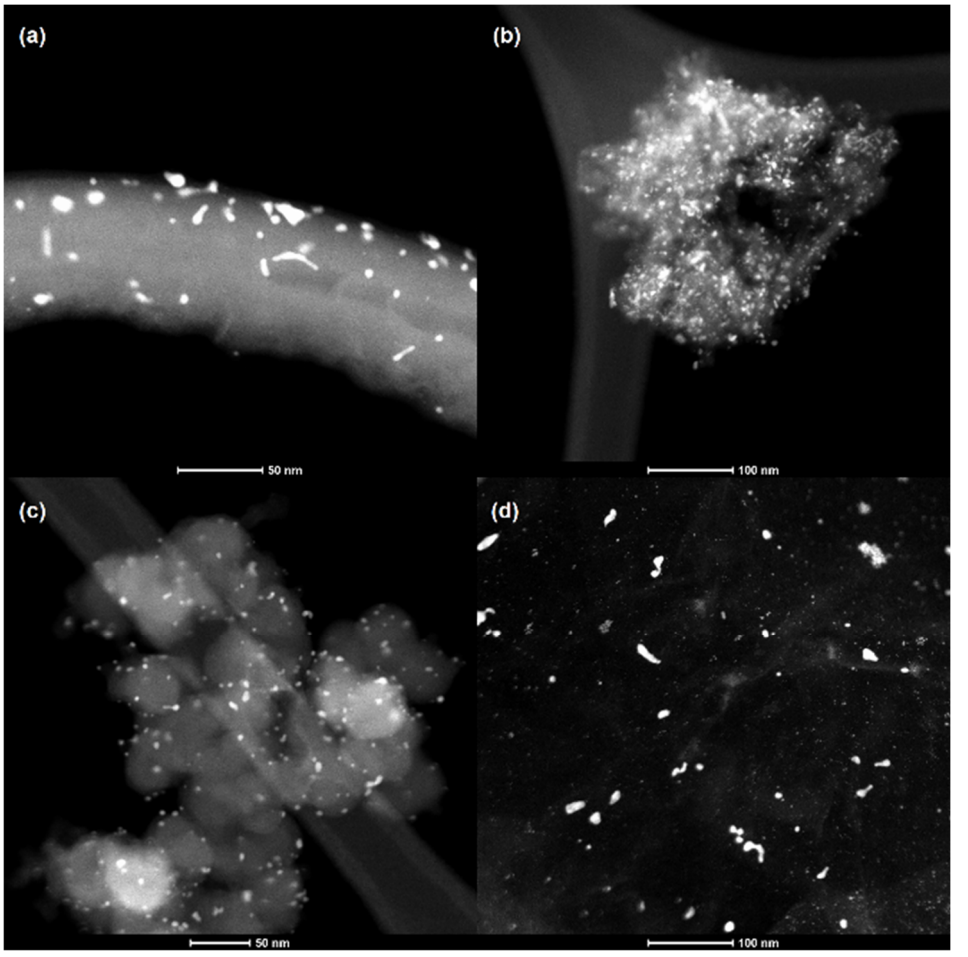

Figure 26. TEM images of Pd/C catalysts: (a) Pd/CNTa, (b) Pd/GNP, (c) Pd/CB and (d) Pd/GNS samples.

For electrodeposited Pd on the GNP surface (Figure 25d) we can see larger Pd particles, but there are also smaller particles formed. At lower overpotential we can observe less of these Pd particles as compared to higher overpotential deposition, however, increase in the number of smaller particles was accompanied by growth of the larger particles. Mendoza-Huizar et al. noticed similar increase on HOPG [144]. These larger Pd deposits on graphene are mostly shaped as nanowires. Similarly, Xiao and others have noted nanowire deposition without any additives and attributed the shape-controlled growth to Cl^- anions [33]. Since the deposition on CNTs was rather uneven a composite of CNT-GNP material was also tested as a support (Figure 25c). Again, at a higher overpotential increased number of smaller particles could be observed but regardless of the overpotential leaf-like growth of larger Pd particles was noted. With composite support we could observe some of the Pd particles were depositing on the surface of CNTs at higher

overpotential, which was not the case for direct deposition onto CNT surfaces. Vulcan carbon and GNP both resulted in Pd nanowire-like structures, however with CB at higher overpotential flower-like structures of Pd could be observed. When studying the effects of electrochemical activation of the CNTs an increased number of sites for Pd deposition is evident from Figure 25b and Pd coverage on CNTs has improved, with nanowire and spherical particles can now be found on the surface of CNTs. Aggregates of PdNPs, which could be observed on the non-activated Pd/CNT, however, remain. Depositing on the surface of CNTa at lower overpotential no Pd particles were seen on the TEM images suggesting that Pd did not deposit.

Average Pd particle sizes for CNT (5.4 nm), GNP (5.2 nm), CB (4.2 nm) and GNS (2.3 nm) supports were counted from TEM images (Figure 26). From these results we can see how the support material can affect the deposited particle size. By comparing particle sizes obtained from lower overpotential to higher overpotential, we could observe that the particle sizes were larger at lower overpotential. This effect was most prominent in the case of GNS where at lower overpotential the formed PdNPs varied in size between 2 and 15 nm, while at higher overpotential well-dispersed smaller Pd particles were observed. It was also noticed that graphene and carbon black supports promote dendritic growth of PdNPs.

6.4.2 CV and CO studies of electrodeposited Pd/C

After Pd deposition the electrodes were washed and moved to an electrochemical cell containing deaerated 0.1 M KOH, in which CO adsorption and oxidation was carried out in order to clean the catalyst materials from chloride contamination. CO-stripping voltammograms are shown in Figure 27.

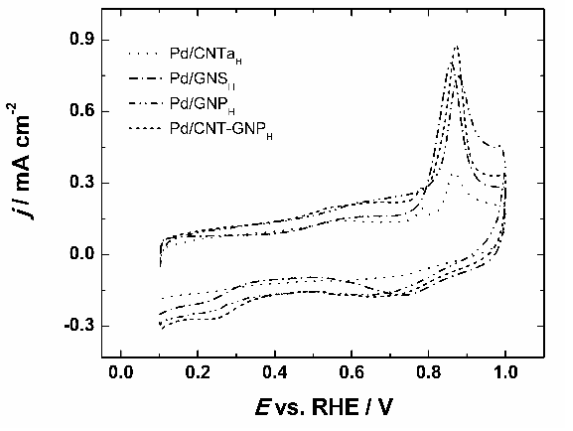

Figure 27. Oxidation of pre-adsorbed CO on Pd/C catalysts in Ar-saturated 0.1 M KOH solution, v = 20 mV s^{-1}. Current densities are normalised to the geometric area of GC.

Slight shifts in CO oxidation peaks could be observed. For CNT-supported Pd particles there are two peaks observed. In acidic media the shifts of CO oxidation peak have been shown to be influenced by the exposed Pd facet [141]. While no similar study has been carried out in alkaline. However, previous works [I] and [IV] have shown that the support material porosity can have an effect on the CO-oxidation peak location.

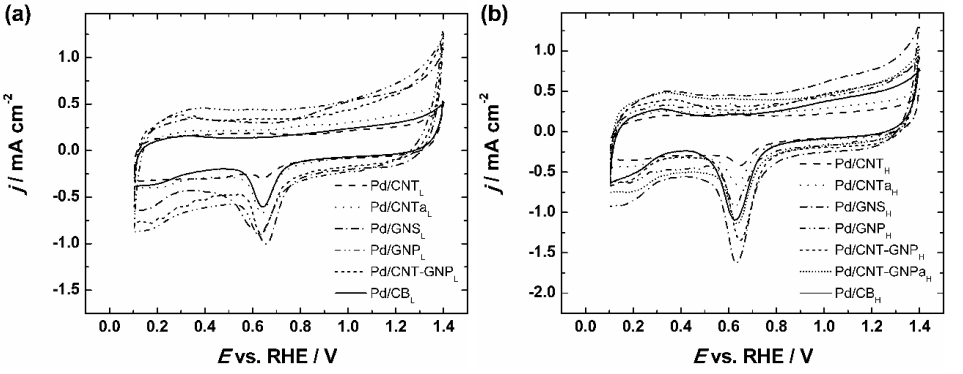

Figure 28. Cyclic voltammograms of Pd/C catalysts in Ar-saturated 0.1 M KOH solution electrodeposited at (a) lower overpotential and (b) higher overpotential, v = 50 mV s^{-1}. Current densities are normalised to geometric area of GC.

CV curves between 0.1 and 1.4 V were recorded before and after the CO oxidation experiment, around 15% increase in ESA values was observed. This suggests that the CO oxidation was necessary for cleaning of the Pd nanoparticles as it has been shown that chloride is strongly adsorbed on Pd surfaces in acidic conditions [145]. Figure 28 shows the CV curves measured after the CO-stripping. Good agreement between the PdO reduction and CO oxidation peak areas was noted. ESA values are provided in Table 6. Typical CV curves of Pd catalysts deposited at lower (Figure 28a) and higher overpotential (Figure 28b) show the PdO reduction peak centred at 0.65 V.

6.4.3 ORR in 0.1 M KOH on electrodeposited Pd/C

After CV studies the electrodes were moved to oxygen-saturated solution. The K-L analysis of RDE data was carried out using Eq. (7). The n values were calculated for all the catalyst materials and it was found to be close to 4.

The ORR results of the first batch of catalysts that were prepared with 500 cycles by stepping between 0 and 0.85 V can be seen in Figure 29a. A well-defined diffusion-limited current plateau is formed for all of the catalysts. Again, differences in the diffusion-limited currents between the different supports can be seen, which most likely comes from different coverage of the working electrode. It can be seen that $E_{1/2}$ decreases with ESA with Pd/GNS_L having the highest ESA value. Tafel plots for these catalysts are presented in Figure 29b.

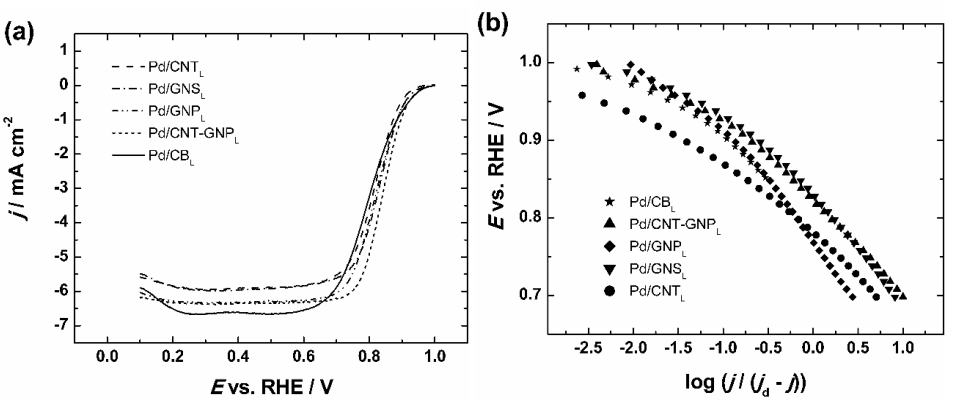

Figure 29. (a) Comparison of RDE results for ORR in O_2-saturated 0.1 M KOH solution on Pd/C catalysts deposited at a lower overpotential. (b) Mass-transfer corrected Tafel plots for ORR. ω = 1900 rpm, v = 10 mV s^{-1}.

Second batch of catalysts deposited at a higher overpotential is shown in Figure 30. O_2 reduction half-wave potential has improved significantly as compared to the catalysts deposited at lower overpotential. Highest impact on the $E_{1/2}$ value is observed in the case of Pd/CNT and Pd/GNP, which improved by 20 mV and 50 mV respectively. Mass of these Pd deposits is not determined since the current efficiency of Pd deposition is unknown, but it is worth noting that there has been a study showing a lower than 4% current efficiency at –0.6 V (vs SCE) for Pd deposition [146]. Tafel plots for the materials deposited at high overpotential are provided in Figure 30b.

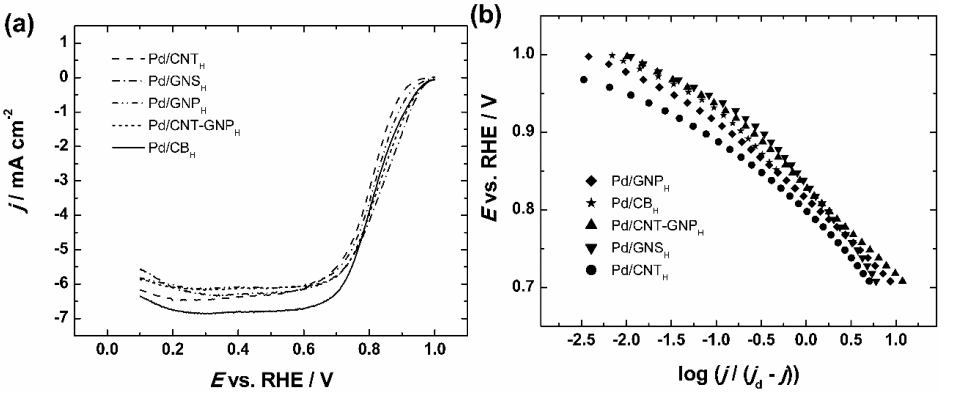

Figure 30. (a) Comparison of RDE results for ORR in O_2-saturated 0.1 M KOH solution on Pd/C catalysts deposited at a higher overpotential. (b) Mass-transfer corrected Tafel plots for ORR. ω = 1900 rpm, v = 10 mV s^{-1}.

Surface activation of the carbon material has been studied in several publications in order to obtain better dispersion of nanoparticles [49, 147, 148]. On electro-chemically activated carbon black Maniam et al. showed good dispersion of

PdNPs [147]. Since the electrocatalytic activity of the Pd/CNT catalyst materials obtained in this part of work was poor, the electrochemical activation process was employed. Effects of the activation process can be seen in Figure 31a with corresponding Tafel plots in Figure 31b. Comparing non-activated CNTs with the activated ones we can see that the activation process increased the ESA (Figure 28) and electrocatalytic activity for ORR (Figure 31). Contrasting results were obtained with the CNT-GNP composite as the effect was reversed, however, in case of CNT-GNP most of the Pd catalyst is deposited on the surface of graphene. When we employed this activation process for the GNP support a similar loss in ESA could be observed. In literature, similar effect of reduction of the ESA value was observed on GO, when it was not sufficiently reduced, the resulting decreased conductivity led to lower ESA values [52]. On the other hand the reduction of GO can lead to improved peroxide production during the ORR process [149].

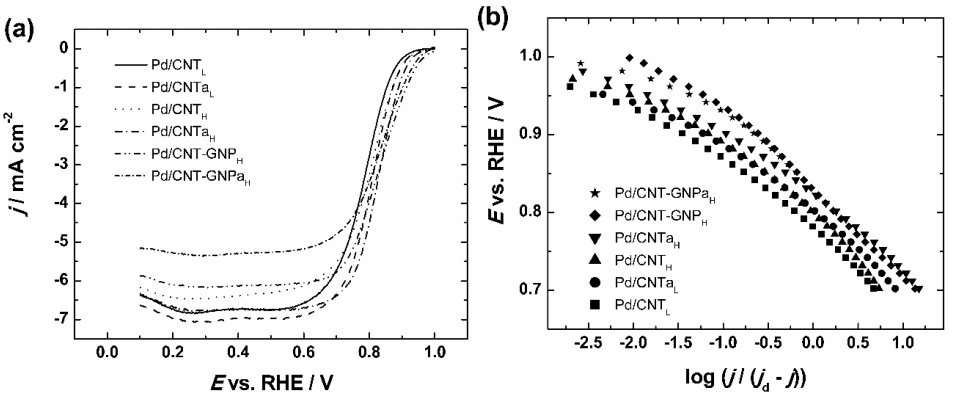

Figure 31. (a) Comparison of RDE voltammetry curves for ORR in O_2-saturated 0.1 M KOH solution on Pd/C catalysts with or without electrochemically activating the carbon material. (b) Corresponding Tafel plots for ORR. ω = 1900 rpm, v = 10 mV s^{-1}. Current densities are normalised to the geometric area of GC.

SA values were calculated in order to compare the intrinsic ORR electrocatalytic activity of these catalysts using Eq. (8) and are listed in Table 6.

Comparing the ESA values, we can see 1.5–2-fold increase between low and high overpotentials applied during the electrodeposition with the exception of GNP where the increase was only 10 %. Looking at the effectiveness of activation for CNTs we can see that the activation process doubled ESA value while a decrease was noted on CNT-GNP. The observed high SA values of Pd/CNT materials may be due to the low ESA that could skew the results, since the determination of ESA values might not be as accurate and PdO reduction peak could combine with quinone peaks that can be found near the same potentials [150]. This could also explain the decrease of SA with activated CNTs as compared to non-activated material since significantly higher ESA could be observed with CNTa. High SA values for all of the catalysts were observed, with

similar activity to 7 nm Pd nanocubes observed in publication [III] and we can see 1.5-fold increase in SA as compared to commercial Pd/C.

Table 6. Kinetic parameters for ORR of different Pd/C catalysts in 0.1 M KOH solution. ω = 1900 rpm.

Catalyst	A_r (cm^2)	SA at 0.9 V (mA cm^{-2})	Tafel slope[a] (mV)	Tafel slope[b] (mV)	$E_{1/2}$ (V)
Pd/CNT$_L$	0.08	0.67	–57	–74	0.78
Pd/CNTa$_L$	0.18	0.41	–51	–76	0.81
PdCNT$_H$	0.19	0.44	–61	–82	0.80
Pd/CNTa$_H$	0.40	0.31	–59	–78	0.83
Pd/GNS$_L$	0.59	0.38	–78	–113	0.83
Pd/GNS$_H$	1.17	0.37	–79	–134	0.84
Pd/GNP$_L$	0.43	0.34	–92	–133	0.77
Pd/GNP$_H$	0.50	0.34	–78	–99	0.82
Pd/CNT-GNP$_L$	0.57	0.35	–74	–111	0.82
Pd/CNT-GNP$_H$	0.85	0.32	–90	–123	0.83
Pd/CNT-GNPa$_H$	0.67	0.26	–75	–110	0.83
Pd/CB$_L$	0.41	0.41	–78	–117	0.80
Pd/CB$_H$	0.99	0.27	–89	–127	0.81
Comm. Pd/C	3.42	0.19	–92	–136	0.87

[a]Low current density region, [b]High current density region

Comparing these electrodeposited catalysts with chemically synthesised PdNPs supported on graphene quantum dot we can see that higher SA values were obtained [151]. Similarly, shape-controlled particles synthesised by Shao et al. showed activity comparable to commercial Pd/C [31]. By preparing PdNPs chemically on CNT surfaces Jukk et al. noted even lower SA values as compared to bulk Pd [152]. The improved activity of these electrodeposited materials as compared to chemically deposited PdNPs might come from the lack of intrusive additives, which might hamper the performance of catalyst materials. In continuation Jukk et al. prepared PdNPs supported on CNT using magnetron sputtering and obtained SA values that were comparable to those of bulk Pd [54]. Pd/CNT has been shown to be a good electrocatalyst for the ORR [153]. Using linkers to improve the activity of Pd/CNT, the activity enhancement compared to conventional Pd/CNT catalyst has been reported [56]. Higher mass and specific activities have been obtained using Pd/GNS catalysts as compared to Pt/GNS [4]. Excellent PEMFC performance has been obtained with PdNPs prepared by electrodeposition [154] and pulse microwave synthesis [155]. In this part of the present thesis the most promising material for Pd nanoparticle support was GNS with the best dispersion and smallest PdNPs. Furthermore, it has been shown that graphene support for PdNPs give excellent results when nitrogen doping is introduced [135, 156].

The ESA value of Pd catalysts deposited on the CNT-GNP composite material is higher than on the two supports separately. This suggests that these composites are efficient electrodeposited catalyst support materials. The Tafel slope values in the high current density region are close to –120 mV with the exception of CNT supported Pd catalysts. Similar slope values have been also noted with magnetron-sputtered Pd/CNT [54], which suggests that surface oxidation of Pd particles differs on CNT supports. Tafel slope values in the low overpotential region is typically –60 mV for Pd, however slightly higher values are observed with all carbon-supported Pd catalysts that were electrochemically deposited.

6.5 Plasma-assisted synthesis of Pd/C catalysts for ORR

In this part of the work Pd nanoparticles were deposited on various carbon supports (rGO, NrGO and Vulcan carbon) using plasma jet treatment in aqueous solution [VI]. GO and NGO were co-reduced with Pd ions during plasma treatment and Vulcan carbon was used as a support for comparison. These catalyst materials were studied in 0.1 M KOH solution. Furthermore, these catalysts were evaluated vs commercial Pd/C. Catalyst materials were named with Pd/support.

6.5.1 SEM and TEM studies of Pd/C prepared by plasma-assistance

From Figure 32 we can see well-dispersed PdNPs covering all of the carbon supports. With carbon black in Figure 32c we can see ca 50 nm carbon particles covered with PdNPs, with graphene some collection of particles on the edges can be seen. Pd particle deposition to edge sites of graphene occurs most likely due to preferential deposition on defect sites of the carbon material [157], similar effect was also noted in the electrodeposition part of this thesis [V] in which Pd particles deposited preferentially on the ends of CNTs. Particle sizes were determined from TEM images (Figure 33) with average Pd particle sizes being: 2.9 ± 0.6 nm (Pd/rGO), 2.3 ± 0.5 nm (Pd/NrGO) and 2.8 ± 0.6 nm (Pd/Vulcan). Comparing these Pd particle sizes there is no statistical difference between Vulcan carbon supported and rGO supported PdNPs. In contrast, N-doped graphene facilitates deposition of smaller Pd particles compared to the other two supports. Particle sizes of 2.4–2.7 nm were observed on N-doped carbon black support prepared by Yang et al., while regular CB yielded 2.8–3.2 nm particles [158]. Similar particle sizes (2.35 ± 0.51 nm) using the same method for Pt/NrGO preparation were obtained by our workgroup, which suggest this method of particle preparation could be employed for preparing small well dispersed metal nanoparticles on carbon supports [112]. The citrate method used within this work previously (I–III) resulted in Pd spheres of sizes of around 2.8 ± 0.4 nm which is comparable to the Pd nanoparticles obtained on the non-doped carbon materials using the plasma method.

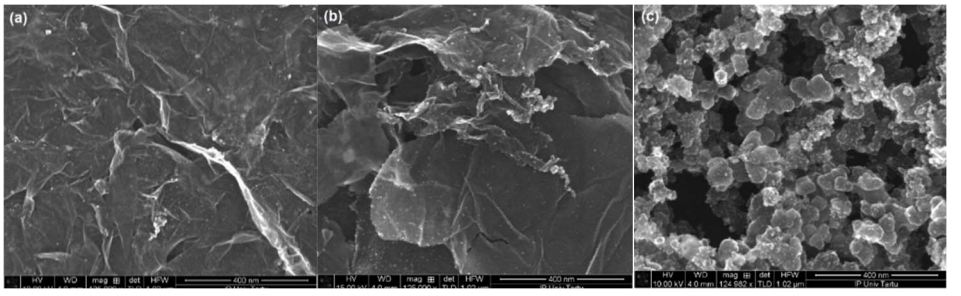

Figure 32. SEM images of (a) Pd/rGO, (b) Pd/NrGO and (c) Pd/Vulcan samples.

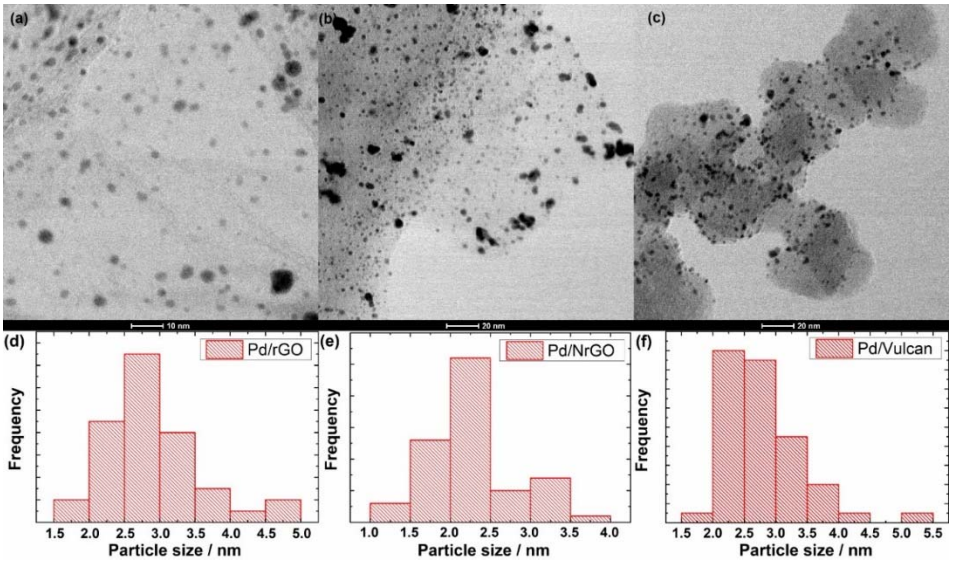

Figure 33. TEM images of (a) Pd/rGO, (b) Pd/NrGO and (c) Pd/Vulcan samples and corresponding particle size histograms (d–f).

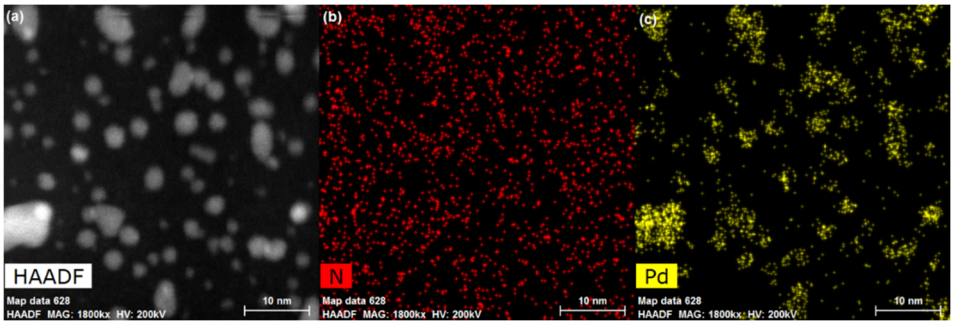

Figure 34. (a) High-angle annular dark-field image of Pd/NrGO catalyst and elemental maps of the same area imaging distribution of (b) nitrogen and (c) palladium.

Pd/NrGO was further studied using STEM with HAADF (Figure 34) showing PdNPs fixed on both sides of the NrGO nanosheet. Element mapping of Pd shows good coincidence with particles of the HAADF imaging. Nitrogen and oxygen mapping (data not shown) revealed uniform distribution on the NrGO surface.

6.5.2 XPS studies of Pd/C materials prepared by plasma-assistance

In Figure 35 XPS spectra for Pd/NrGO are presented. Peak locations for Pd3d are at 335.5 and 338.8 eV showing metallic Pd [159]. The wide shoulders at high binding energy side of the Pd3d peaks might refer to higher oxidation states due to Pd-N or Pd-O. Vinayan and others have observed a similar widening of the Pd peak on N-doped graphene supported PdNPs suggesting that this could originate from Pd-N bonding [160].

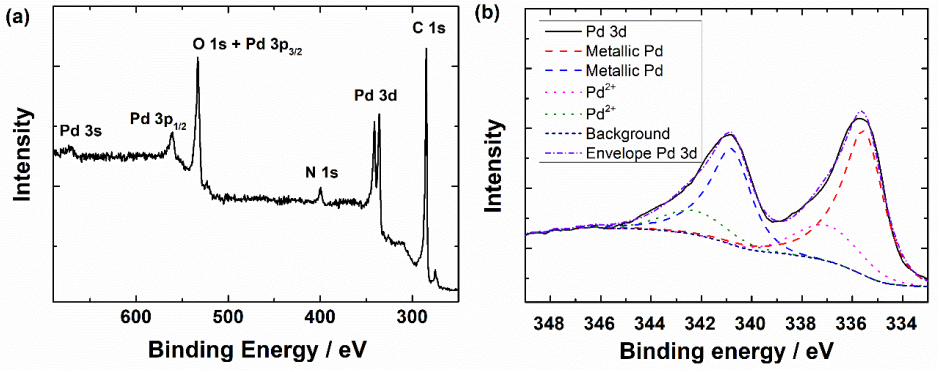

Figure 35. Wide-scan XPS spectrum of a Pd/NrGO sample (a) and detailed spectrum in the Pd 3d region (b).

6.5.3 CV and CO studies of Pd/C catalysts prepared by plasma-assistance

Similarly to [I–V] before the ORR studies, the electrodes were characterised and cleaned using CV and CO-stripping methods. CO oxidation profiles presented in Figure 36b show significant shifts in the CO-stripping peak location. Furthermore, Pd/rGO has two peaks with first peak matching that of Pd/Vulcan. In the case of Pt electrodes, the shift towards lower CO oxidation potentials has been noted on agglomerated Pt particles [124]. However, similar to previous discussions [I, IV, V], these shifts could be caused by the difference in support material or even crystallographic structure. Typical CV profile can be seen similarly to [I–V]. Very slight shift in the PdO peak location in comparison to Pd/Vulcan for the other two materials can be seen, which might suggest agglomeration on Pd/Vulcan as has been concluded in [I–V]. The ESA values are listed in Table 7.

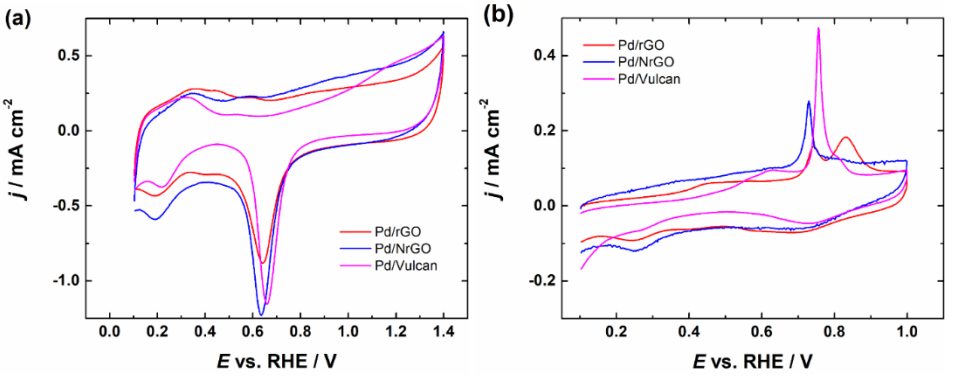

Figure 36. (a) Cyclic voltammograms of Pd/C catalysts in Ar-saturated 0.1 M KOH solution, v = 50 mV s^{-1} and (b) electro-oxidation of pre-adsorbed CO on Pd/C catalysts, v = 10 mV s^{-1}.

6.5.4 ORR studies in 0.1 M KOH on Pd/C catalysts prepared by plasma-assistance

After CO-stripping and CV measurements, the electrocatalytic properties of these Pd/C catalysts were tested in 0.1 M KOH solution for ORR using the RDE method. For comparison of the different Pd/C materials the RDE polarisation data are displayed in Figure 37a with corresponding Tafel plots shown in Figure 37b.

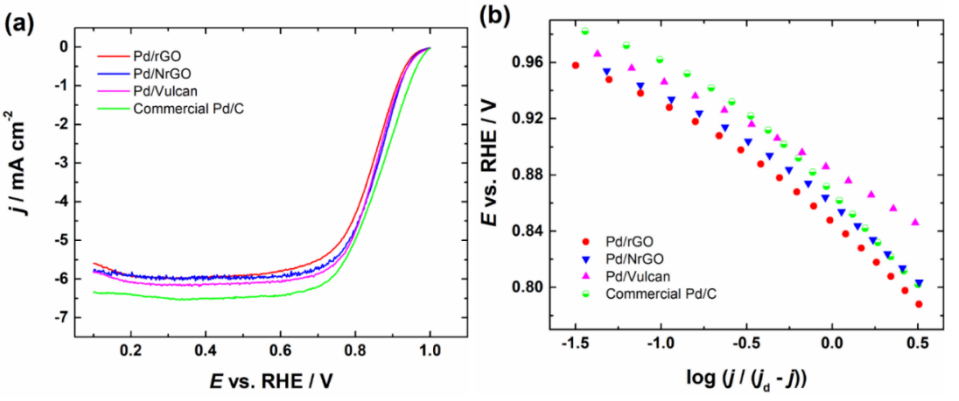

Figure 37. (a) Comparison of RDE results for ORR in O_2-saturated 0.1 M KOH solution on Pd/C catalysts. (b) Mass-transfer corrected Tafel plots for ORR, data derived from (a). ω = 1900 rpm, v = 10 mV s^{-1}. Current densities are normalised to the geometric area of GC.

Table 7. Kinetic parameters for ORR on different Pd/C catalysts in 0.1 M KOH solution. ω = 1900 rpm.

Catalyst	ESA (cm^2)	$E_{1/2}$ (V)	Tafel slope (mV)	SA at 0.9 V (mA cm^{-2})
Pd/rGO	0.73	0.85	–65	0.36
Pd/NrGO	0.94	0.86	–64	0.38
Pd/Vulcan	0.98	0.89	–62	0.52
Comm. Pd/C	3.42	0.87	–92	0.04

This shows that the plasma method along with N-doping can achieve smaller PdNPs in comparison to undoped carbon support materials. Decrease in $E_{1/2}$ in order of: Pd/Vulcan > Pd/NrGO > Pd/C commercial > Pd/rGO can be noted. Similarly to previous works [I–V] the SA values were calculated using Eq. (8) for better comparison of intrinsic electrocatalytic activities of these materials. Calculated SA values for all the catalysts were very close with the exception of Pd/Vulcan, which possesses higher specific activity. Comparing the rGO supported catalyst with NrGO supported one we can see a slight increase in specific activity. Similarly, to the N-doped supports discussed previously [I] most of the Pd particles formed using the plasma-assisted method are larger than couple of Pd atoms, thus the impact of N-doping on the Pd electron structure should be minimal [66]. Increase in the ORR activity has been noted by Perini et al., where PdNPs deposited on mesoporous N-doped carbon showed higher activity as compared to Pd catalyst on undoped support [67] and the activity increase was attributed to the interaction between nitrogen-induced defects and Pd nanoparticles. Lower than expected activity of rGO supported PdNPs might be due to overreduction of GO [52], which could lower the number of deposition sites available as compared to NrGO that has N-induced sites. Underperformance of the N-doped material in terms of the SA value might also be due to the lower average particle size, as it has been reported that the SA value decreases with particle size about three-fold when decreasing the size of the Pd particle from 16.7 to 3 nm [36]. A reason for the lower activity of graphene supported PdNPs in comparison to CB supported counterparts has been investigated by Molina-Garcia and Rees by elucidating the difference between Pt/CB, Pt/rGO, Pt/GO and Pt/MWCNT catalysts, where the higher activity of Pt/CB was explained by graphene promoting $2e^-$ pathway [161]. Zhang et al. have discussed how the Pt-C interactions on graphene support are not optimal for ORR and solved the problem using B-doping to reduce the bond strength between graphene and Pd resulting in higher ESA value [162].

6.6 Pd catalysts for ORR prepared by galvanic exchange

Galvanic exchange of Pd was studied on thin copper films with thicknesses from 0.5 to 10 nm [VII]. Core-shell structures can provide very high mass activities and galvanic exchange is one of the methods that can be used to produce such catalyst structures. Catalyst materials are assigned names with CuxPd, where the x represents the initial nominal Cu layer thickness in nm.

6.6.1 XPS studies of galvanically exchanged CuxPd

XPS spectra for all of the catalyst materials are presented in Figure 38, where Pd 3d doublet at 334.9 and 340.3 eV corresponds to metallic Pd [163–165]. Binding energy shifts which could indicate alloying as observed by Kariuki et al. are not present in these films [163]. No peaks could be observed between 930 and 950 eV, which is the typical BE range for copper indicating that Cu was either completely replaced or covered by Pd.

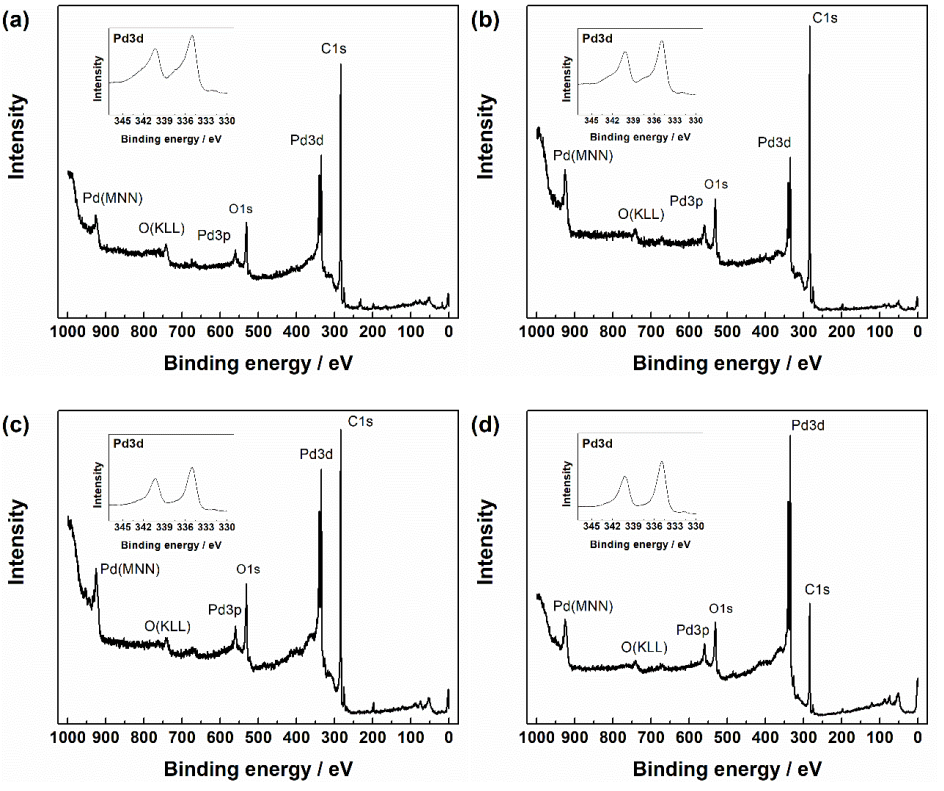

Figure 38. XPS wide scan spectra for PdCu/GC samples. Sacrificial Cu layer thicknesses: (a) 0.5 nm, (b) 1 nm, (c) 2 nm and (d) 5 nm. Insets show high-resolution Pd 3d XPS spectra.

6.6.2 SEM and EDX analysis of galvanically exchanged CuxPd

SEM micrographs in Figure 39 show that 2 nm sacrificial layer produces few growth islands and with 5 nm an uneven overlayer is formed. Agglomeration can be noted on the 5 nm layer with cubic shape. This could be due to the exchange taking place in solution that contains Cl^- ions that have been used in the synthesis of cubic PdNPs [93]. However, the number of these cubic particles is low, and their shape is unrefined and no improvement in catalytic activity is expected as was seen with cubic Pd particles during previous work [III]. Changing the sacrificial

Cu layer from 5 to 10 nm we can see growth of the Pd layer and agglomerates, but the shape of agglomerates has evolved to spherical. Nominal 10 nm films of Pt [166] and Pd [167] deposited directly on the GC surface resulted in spherical deposits. The structure of the deposits obtained using galvanic exchange changed into porous Pd film. On the basis of the SEM images, we can assume that the exchange process is not only switching out the topmost atoms but there are dissolution zones and deposition zones on the surface. Observation of deposition and dissolution regions has also been reported previously [99]. In a previous work by our group with thin Pt films [166], a 5 nm film was sufficient to cover the GC electrode surface, however with galvanic exchange the film still has extensive areas that are not covered by Pd. EDX measurements were carried out in order to determine if there is some remaining copper after galvanic exchange. By EDX copper was detected with 5 and 10 nm coatings, while no copper was detected by XPS. This suggests that all of the remaining copper is buried underneath the Pd agglomerates.

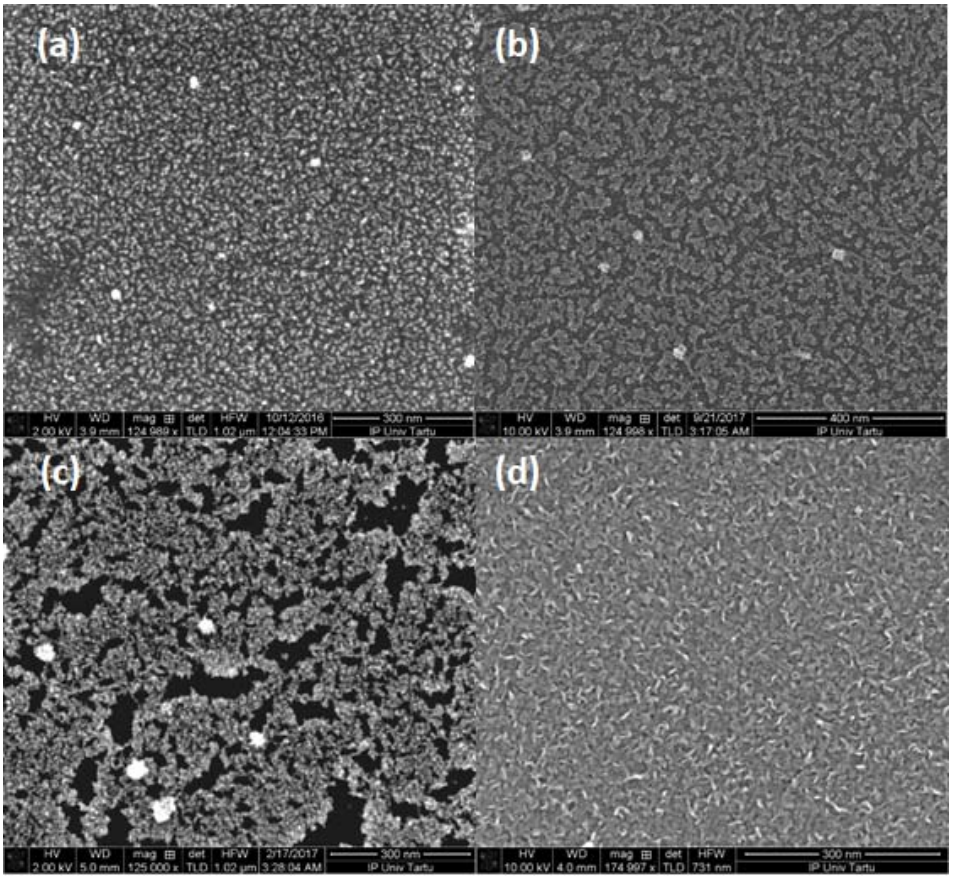

Figure 39. SEM micrographs of the Pd overlayers formed by galvanic exchange. Sacrificial Cu layer thicknesses: (a) 2 nm, (b) 5 nm and (c) 10 nm and (d) polished GC electrode.

6.6.3 CV of galvanically exchanged CuxPd

These electrodes were studied and cleaned using CV. The cyclic voltammograms obtained (Figure 40) resemble typical CVs of polycrystalline palladium in 0.1 KOH similarly with previous articles [I–VI]. During potential cycling no extra peaks that could indicate presence of Cu were observed fortifying the results obtained by XPS and EDX, which suggested no surface Cu. PdO reduction peak for the 0.5 nm Cu sacrificial layer material is shifted 10 mV towards negative potentials. Similar shifts have been observed previously [I–VI] and generally attributed to smaller Pd particles. Such shifts were also observed with thin Pd films, where oxide reduction peaks of 0.25 nm films shifted negative by 60 mV as compared to 10 nm film [167]. As expected, the ESA value of Pd increased with the sacrificial layer thickness.

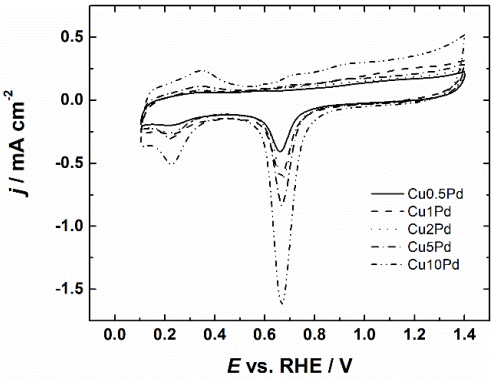

Figure 40. Cyclic voltammograms of CuxPd catalysts in Ar-saturated 0.1 M KOH solution, v = 50 mV s^{-1}. Current densities are normalised to geometric area of GC.

6.6.4 ORR in 0.1 M KOH on galvanically exchanged CuxPd catalysts

Using the K-L analysis it was found that the n values for all the electrodes studied was close to 4, with exception of Cu0.5Pd which had n value of 3.7. Lower n value could be attributed to low surface coverage and similar effect was observed on thin Pd films [167]. Since the ORR on the GC surface proceeds through $2e^-$ pathway, it could facilitate parallel ORR reaction due to the low loading of Pd.

Comparison of the RDE results for oxygen reduction collected with electrodes using different sacrificial layer thicknesses is shown in Figure 41. Diffusion-limited current plateau for all the catalysts is well defined, with two of the lower thicknesses having slightly lower diffusion-limited current density in comparison with the rest of the catalysts. This is most likely due to lower coverage of the working electrode. The ORR onset potentials (E_{onset}) provided in Table 8 were determined at −0.1 mA cm^{-2}. The E_{onset} increases with ESA.

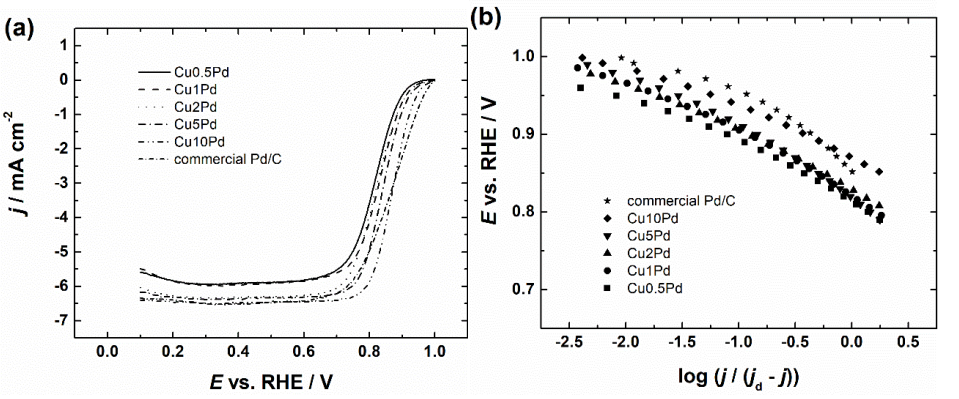

Figure 41. (a) Comparison of RDE voltammetry curves for ORR on CuxPd catalysts and commercial Pd/C in O_2-saturated 0.1 M KOH and (b) corresponding Tafel plots for ORR. ω = 1900 rpm, v = 10 mV s^{-1}.

Table 8. Kinetic parameters for ORR on CuxPd electrodes with different Cu sacrificial layer thicknesses in 0.1 M KOH solution. ω = 1900 rpm.

Catalyst	ESA (cm^2)	Tafel slope (mV)	$E_{1/2}$ (V)	E_{onset} (V)	SA at 0.9 V (mA cm^{-2})
Cu0.5Pd	0.29	–52	0.82	0.94	0.34
Cu1Pd	0.39	–61	0.83	0.95	0.38
Cu2Pd	0.42	–64	0.83	0.96	0.37
Cu5Pd	0.57	–65	0.84	0.96	0.38
Cu10Pd	1.20	–62	0.87	0.98	0.42
Comm. Pd/C	3.42	–92	0.87	0.99	0.19

Similarly to the work with Pd thin films [167] no impact on the SA for oxygen reduction can be observed with varying sacrificial film thickness. While the CV suggested that 0.5 nm could have lower SA value due to its smaller particle size hinted with the shift of the PdO reduction peak the decrease of SA might be due to the effects that were described previously [I–IV] suggesting that the OH^- adsorption on smaller Pd particles is stronger and results in lower SA values [36]. Comparing the SA values of these catalysts to commercial Pd/C [V] a higher ORR activity can be seen. Interestingly, the Pd films electrodeposited on GC possess higher specific activity [168]. Similarly, to [I, III–VI] the Tafel plots were analysed and only one slope of –60 mV was observed, and similarly to previous discussions this refers to Pd that is covered by a layer of surface oxide. Tafel slope of –90 mV for commercial Pd/C could be due to the influence of carbon support as various Pd/C catalysts studied within this work [I–VI] had higher slope values than the expected –60 mV.

7. SUMMARY

Electrocatalytic activity of nanostructured Pd catalyst materials for the oxygen reduction reaction was evaluated in either sulphuric acid, perchloric acid or potassium hydroxide solution using the rotating disc electrode method. Methods for the preparation of Pd nanoparticle on various supports varied from electrochemical to physical to chemical methods.

In the first part commercial porous N-doped carbon materials were evaluated as Pd catalyst supports. Pd nanoparticles were prepared by citrate method and dispersed on these mesoporous support materials. Higher dispersion of PdNPs on the N-doped carbon materials compared to Vulcan carbon was observed. Pd catalyst dispersed on N-doped carbon materials showed higher specific activity in acidic conditions and a similar activity in alkaline solution in comparison to Vulcan carbon supported Pd nanoparticles. An anion exchange membrane fuel cell with N-doped carbon-supported Pd cathodes showed good fuel cell performance.

In the second part cubic Pd nanoparticles of varying sizes were supported on Vulcan carbon. In this study Pd nanocubes possessed higher specific activity in comparison to spherical PdNPs in both alkaline and acidic conditions. However due to cubic particles being larger than spherical Pd nanoparticles the mass activity values were highest for spherical particles in both alkaline and acidic media.

In the next part Pd was deposited onto carbide-derived carbon materials using borohydride method. The CDC material with the highest amount of smaller micropores showed the best dispersion of Pd particles and smallest Pd particle size out of the Pd/CDC materials studied. In both alkaline and acidic conditions Pd/CDC materials outperformed Pd/Vulcan in terms of the specific activity for oxygen reduction.

In the fourth part of work electrodeposition was employed to deposit Pd nanoparticles onto various nanocarbon supports such as graphene and carbon nanotubes. Higher deposition overpotential resulted in a higher amount of smaller Pd particles on the support materials. Electrodeposition on the CNT surface was not easily feasible, however the electrochemical activation of the CNTs led to better dispersion of Pd particles on their surface. From all the materials used, Pd deposited onto graphene nanosheets showed the highest electrochemical surface area and had the highest specific activity values, suggesting it to be an excellent support for PdNPs.

In the next part of the thesis plasma-assisted synthesis of PdNPs was employed. N-doped and undoped graphene oxide were compared to Vulcan carbon as support materials for the synthesised Pd particles. Accompanying the Pd precursor reduction GO was also reduced to rGO. On these materials smallest Pd particles and best dispersion were observed on the Pd/NrGO material. However, the SA values were similar for both Pd/rGO and Pd/NrGO catalysts, but slightly lower than that of Pd/Vulcan.

In the last part of this work the galvanic exchange of Cu was employed as a deposition method of nanostructured Pd. Cu films with varying thicknesses from 0.5 to 10 nm were deposited onto glassy carbon using electron beam evaporation.

Energy dispersive X-ray spectroscopy could only detect Cu on 5 and 10 nm sacrificial layer thicknesses on the galvanically exchanged Pd coatings, while the surface sensitive methods of X-ray photoelectron spectroscopy and cyclic voltammetry could not detect any copper. Specific activities in alkaline conditions increased with the film thickness, which could be due to larger Pd particles that have higher SA values.

All of the RDE data obtained in this work was evaluated using the Koutecky-Levich analysis. From the K-L equation the number of electrons transferred per O_2 molecule for the ORR was found. For most of the catalysts, the *n* value was close to four, however lower values were observed when Pd loading was lower in last part of the work. This value would suggest that the ORR on Pd/C catalysts prepared within this work proceeds through a $4e^-$ pathway. Rate-limiting step for the ORR was evaluated using the Tafel slope values and it was revealed to be the transfer of the first electron to the O_2 molecule.

8. REFERENCES

[1] E. Antolini, Palladium in fuel cell catalysis, Energy & Environmental Science 2(9) (2009) 915–931.

[2] M. Shao, Palladium-based electrocatalysts for hydrogen oxidation and oxygen reduction reactions, Journal of Power Sources 196(5) (2011) 2433–2444.

[3] H. Erikson, A. Sarapuu, J. Solla-Gullon, K. Tammeveski, Recent progress in oxygen reduction electrocatalysis on Pd-based catalysts, Journal of Electro-analytical Chemistry 780 (2016) 327–336.

[4] M.H. Seo, S.M. Choi, H.J. Kim, W.B. Kim, The graphene-supported Pd and Pt catalysts for highly active oxygen reduction reaction in an alkaline condition, Electrochemistry Communications 13(2) (2011) 182–185.

[5] R. Carrera-Cerritos, V. Baglio, A.S. Aricò, J. Ledesma-García, M.F. Sgroi, D. Pullini, A.J. Pruna, D.B. Mataix, R. Fuentes-Ramírez, L.G. Arriaga, Improved Pd electro-catalysis for oxygen reduction reaction in direct methanol fuel cell by reduced graphene oxide, Applied Catalysis B: Environmental 144 (2014) 554–560.

[6] L. Jiang, A. Hsu, D. Chu, R. Chen, Oxygen Reduction Reaction on Carbon Supported Pt and Pd in Alkaline Solutions, Journal of the Electrochemical Society 156(3) (2009) B370–B376.

[7] M.R. Tarasevich, A. Sadkowski, E. Yeager, in: B.E. Conway, J.O'M. Bockris, E. Yeager, S.U.M. Khan, R.E. White (Eds.), Comprehensive treatise of electro-chemistry. vol. 7, Plenum Press, New York, 1983, pp. 301–398.

[8] F.D. Sanij, P. Balakrishnan, P. Leung, A. Shah, H. Su, Q. Xu, Advanced Pd-based nanomaterials for electro-catalytic oxygen reduction in fuel cells: A review, International Journal of Hydrogen Energy 46(27) (2021) 14596–14627.

[9] N.M. Marković, T.J. Schmidt, V. Stamenković, P.N. Ross, Oxygen Reduction Reaction on Pt and Pt Bimetallic Surfaces: A Selective Review, Fuel Cells 1(2) (2001) 105–116.

[10] S. Sui, X.Y. Wang, X.T. Zhou, Y.H. Su, S. Riffatc, C.J. Liu, A comprehensive review of Pt electrocatalysts for the oxygen reduction reaction: Nanostructure, activity, mechanism and carbon support in PEM fuel cells, Journal of Materials Chemistry A 5(5) (2017) 1808–1825.

[11] J.S. Spendelow, A. Wieckowski, Electrocatalysis of oxygen reduction and small alcohol oxidation in alkaline media, Physical Chemistry Chemical Physics 9(21) (2007) 2654–2675.

[12] D. Pletcher, S. Sotiropoulos, A study of cathodic oxygen reduction at platinum using microelectrodes, Journal of Electroanalytical Chemistry 356(1) (1993) 109–119.

[13] N.M. Markovic, H.A. Gasteiger, P.N. Ross, Oxygen Reduction on Platinum Low-Index Single-Crystal Surfaces in Sulfuric Acid Solution: Rotating Ring-Pt(hkl) Disk Studies, The Journal of Physical Chemistry 99(11) (1995) 3411–3415.

[14] N. Markovic, H. Gasteiger, P.N. Ross, Kinetics of Oxygen Reduction on Pt(hkl) Electrodes: Implications for the Crystallite Size Effect with Supported Pt Electro-catalysts, Journal of The Electrochemical Society 144(5) (1997) 1591–1597.

[15] I. Srejic, Z. Rakocevic, M. Nenadovic, S. Strbac, Oxygen reduction on poly-crystalline palladium in acid and alkaline solutions: topographical and chemical Pd surface changes, Electrochimica Acta 169 (2015) 22–31.

[16] G.V. Fortunato, E. Pizzutilo, E.S.F. Cardoso, M.R.V. Lanza, I. Katsounaros, S.J. Freakley, K.J.J. Mayrhofer, G. Maia, M. Ledendecker, The oxygen reduction

reaction on palladium with low metal loadings: The effects of chlorides on the stability and activity towards hydrogen peroxide, Journal of Catalysis 389 (2020) 400–408.
[17] L.L. Zhang, Q.W. Chang, H.M. Chen, M.H. Shao, Recent advances in palladium-based electrocatalysts for fuel cell reactions and hydrogen evolution reaction, Nano Energy 29 (2016) 198–219.
[18] H. Meng, D. Zeng, F. Xie, Recent Development of Pd-Based Electrocatalysts for Proton Exchange Membrane Fuel Cells, Catalysts 5(3) (2015) 1221–1274.
[19] K. Khan, S. Derindere Köseoğlu, Is palladium price in bubble?, Resources Policy 68 (2020) 101780.
[20] D. Bao, Dynamics and correlation of platinum-group metals spot prices, Resources Policy 68 (2020) 101772.
[21] A. Zadick, L. Dubau, U.B. Demirci, M. Chatenet, Effects of Pd Nanoparticle Size and Solution Reducer Strength on Pd/C Electrocatalyst Stability in Alkaline Electrolyte, Journal of The Electrochemical Society 163(8) (2016) F781–F787.
[22] L.M. Vracar, D.B. Sepa, A. Damjanovic, Palladium Electrode in Oxygen – Saturated Aqueous Solutions: Reduction of Oxygen in the Activation – Controlled Region, Journal of The Electrochemical Society 133(9) (1986) 1835–1839.
[23] S. Kondo, M. Nakamura, N. Maki, N. Hoshi, Active Sites for the Oxygen Reduction Reaction on the Low and High Index Planes of Palladium, The Journal of Physical Chemistry C 113(29) (2009) 12625–12628.
[24] A. Hitotsuyanagi, S. Kondo, M. Nakamura, N. Hoshi, Structural effects on the oxygen reduction reaction on n(111)–(100) series of Pd, Journal of Electroanalytical Chemistry 657(1) (2011) 123–127.
[25] H. Erikson, A. Sarapuu, N. Alexeyeva, K. Tammeveski, J. Solla-Gullon, J.M. Feliu, Electrochemical reduction of oxygen on palladium nanocubes in acid and alkaline solutions, Electrochimica Acta 59 (2012) 329–335.
[26] H. Erikson, A. Sarapuu, K. Tammeveski, J. Solla-Gullon, J.M. Feliu, Enhanced electrocatalytic activity of cubic Pd nanoparticles towards the oxygen reduction reaction in acid media, Electrochemistry Communications 13(7) (2011) 734–737.
[27] C.-L. Lee, H.-P. Chiou, C.-R. Liu, Palladium nanocubes enclosed by (100) planes as electrocatalyst for alkaline oxygen electroreduction, International Journal of Hydrogen Energy 37(5) (2012) 3993–3997.
[28] C.-L. Lee, H.-P. Chiou, Methanol-tolerant Pd nanocubes for catalyzing oxygen reduction reaction in H2SO4 electrolyte, Applied Catalysis B: Environmental 117–118 (2012) 204–211.
[29] N. Arjona, M. Guerra-Balcázar, L. Ortiz-Frade, G. Osorio-Monreal, L. Álvarez-Contreras, J. Ledesma-García, L.G. Arriaga, Electrocatalytic activity of well-defined and homogeneous cubic-shaped Pd nanoparticles, Journal of Materials Chemistry A 1(48) (2013) 15524-15529.
[30] K. Huang, Z. Liu, C. Lee, Truncated palladium nanocubes: Synthesis and the effect of OH- concentration on their catalysis of the alkaline oxygen reduction reaction, Electrochimica Acta 157 (2015) 78–87.
[31] M.H. Shao, J. Odell, M. Humbert, T.Y. Yu, Y.N. Xia, Electrocatalysis on Shape-Controlled Palladium Nanocrystals: Oxygen Reduction Reaction and Formic Acid Oxidation, Journal of Physical Chemistry C 117(8) (2013) 4172–4180.
[32] S. Choi, H. Jeong, K.-h. Choi, J.Y. Song, J. Kim, Electrodeposition of Triangular Pd Rod Nanostructures and Their Electrocatalytic and SERS Activities, ACS Applied Materials & Interfaces 6(4) (2014) 3002–3007.

[33] L. Xiao, L. Zhuang, Y. Liu, J.T. Lu, H.D. Abruna, Activating Pd by Morphology Tailoring for Oxygen Reduction, Journal of the American Chemical Society 131(2) (2009) 602–608.
[34] A. Zadick, L. Dubau, A. Zalineeva, C. Coutanceau, M. Chatenet, When cubic nanoparticles get spherical: An Identical Location Transmission Electron Microscopy case study with Pd in alkaline media, Electrochemistry Communications 48 (2014) 1–4.
[35] W. Zhou, M. Li, O.L. Ding, S.H. Chan, L. Zhang, Y. Xue, Pd particle size effects on oxygen electrochemical reduction, International Journal of Hydrogen Energy 39(12) (2014) 6433–6442.
[36] L. Jiang, A. Hsu, D. Chu, R. Chen, Size-Dependent Activity of Palladium Nanoparticles for Oxygen Electroreduction in Alkaline Solutions, Journal of the Electrochemical Society 156(5) (2009) B643–B649.
[37] W. An, P. Liu, Size and Shape Effects of Pd@Pt Core–Shell Nanoparticles: Unique Role of Surface Contraction and Local Structural Flexibility, The Journal of Physical Chemistry C 117(31) (2013) 16144–16149.
[38] A. Anastasopoulos, J.C. Davies, L. Hannah, B.E. Hayden, C.E. Lee, C. Milhano, C. Mormiche, L. Offin, The Particle Size Dependence of the Oxygen Reduction Reaction for Carbon-Supported Platinum and Palladium, ChemSusChem 6(10) (2013) 1973–1982.
[39] R. Jiang, S.o. Tung, Z. Tang, L. Li, L. Ding, X. Xi, Y. Liu, L. Zhang, J. Zhang, A review of core-shell nanostructured electrocatalysts for oxygen reduction reaction, Energy Storage Materials 12 (2018) 260–276.
[40] J.L. Zhang, M.B. Vukmirovic, Y. Xu, M. Mavrikakis, R.R. Adzic, Controlling the catalytic activity of platinum-monolayer electrocatalysts for oxygen reduction with different substrates, Angewandte Chemie-International Edition 44(14) (2005) 2132–2135.
[41] V. Stamenkovic, B.S. Mun, K.J.J. Mayrhofer, P.N. Ross, N.M. Markovic, J. Rossmeisl, J. Greeley, J.K. Norskov, Changing the activity of electrocatalysts for oxygen reduction by tuning the surface electronic structure, Angewandte Chemie-International Edition 45(18) (2006) 2897–2901.
[42] M.H. Shao, P. Liu, J.L. Zhang, R. Adzic, Origin of enhanced activity in palladium alloy electrocatalysts for oxygen reduction reaction, Journal of Physical Chemistry B 111(24) (2007) 6772–6775.
[43] M.H. Shao, T. Huang, P. Liu, J. Zhang, K. Sasaki, M.B. Vukmirovic, R.R. Adzic, Palladium Monolayer and Palladium Alloy Electrocatalysts for Oxygen Reduction, Langmuir 22(25) (2006) 10409–10415.
[44] M.H. Shao, K. Sasaki, R.R. Adzic, Pd-Fe nanoparticles as electrocatalysts for oxygen reduction, Journal of the American Chemical Society 128(11) (2006) 3526–3527.
[45] G.M. Jiang, X.W. Li, X.S. Lv, L. Chen, Core/shell FePd/Pd catalyst with a superior activity to Pt in oxygen reduction reaction, Science Bulletin 61(16) (2016) 1248–1254.
[46] G. Chao, L. Zhang, T. Xue, J. Tian, W. Fan, T. Liu, Lattice-strain and electron-density modulation of palladium nanocatalysts for highly efficient oxygen reduction, Journal of Colloid and Interface Science 602 (2021) 159–167.
[47] Y. Chen, J. Cai, P. Li, G. Zhao, G. Wang, Y. Jiang, J. Chen, S.X. Dou, H. Pan, W. Sun, Hexagonal Boron Nitride as a Multifunctional Support for Engineering

Efficient Electrocatalysts toward the Oxygen Reduction Reaction, Nano Letters 20(9) (2020) 6807–6814.
[48] C. Alegre, A. Stassi, E. Modica, C. Lo Vecchio, A.S. Aricò, V. Baglio, Investigation of the activity and stability of Pd-based catalysts towards the oxygen reduction (ORR) and evolution reactions (OER) in iron–air batteries, RSC Advances 5(32) (2015) 25424–25427.
[49] S.M.S. Kumar, J.S. Herrero, S. Irusta, K. Scott, The effect of pretreatment of Vulcan XC-72R carbon on morphology and electrochemical oxygen reduction kinetics of supported Pd nano-particle in acidic electrolyte, Journal of Electroanalytical Chemistry 647(2) (2010) 211–221.
[50] S. Kabir, A. Serov, A. Zadick, K. Artyushkova, P. Atanassov, Palladium Nanoparticles Supported on Three-Dimensional Graphene Nanosheets: Superior Cathode Electrocatalysts, Chemelectrochem 3(10) (2016) 1655–1666.
[51] S. Kabir, A. Serov, P. Atanassov, 3D-Graphene supports for palladium nanoparticles: Effect of micro/macropores on oxygen electroreduction in Anion Exchange Membrane Fuel Cells, Journal of Power Sources 375 (2018) 255–264.
[52] A.P. Liu, M. Yuan, M. Zhao, C.D. Lu, T.Y. Zhao, P.G. Li, W.H. Tang, Graphene modulated assembly of PtPd bimetallic catalysts for electro-oxidation of methanol, Journal of Alloys and Compounds 586 (2014) 99–104.
[53] T.G. Nikiforova, Y.V. Kabeneva, O.A. Runova, Carbon-supported palladium catalysts for fuel cells, Russian Journal of Applied Chemistry 83(6) (2010) 1001–1009.
[54] K. Jukk, N. Alexeyeva, A. Sarapuu, P. Ritslaid, J. Kozlova, V. Sammelselg, K. Tammeveski, Electroreduction of oxygen on sputter-deposited Pd nanolayers on multi-walled carbon nanotubes, International Journal of Hydrogen Energy 38(9) (2013) 3614–3620.
[55] K. Jukk, N. Alexeyeva, P. Ritslaid, J. Kozlova, V. Sammelselg, K. Tammeveski, Electrochemical Reduction of Oxygen on Heat-Treated Pd Nanoparticle/Multi-Walled Carbon Nanotube Composites in Alkaline Solution, Electrocatalysis 4(1) (2013) 42–48.
[56] D.L. Wang, S.F. Lu, S.P. Jiang, Pd/HPW-PDDA-MWCNTs as effective non-Pt electrocatalysts for oxygen reduction reaction of fuel cells, Chemical Communications 46(12) (2010) 2058–2060.
[57] X. Zhang, P. Yang, S.P. Jiang, Pd nanoparticles assembled on Ni- and N-doped carbon nanotubes towards superior electrochemical activity, International Journal of Hydrogen Energy 46(2) (2021) 2065–2074.
[58] D. Kim, M.S. Ahmed, S. Jeon, Different length linkages of graphene modified with metal nanoparticles for oxygen reduction in acidic media, Journal of Materials Chemistry 22(32) (2012) 16353–16360.
[59] S.H. Joo, S.J. Choi, I. Oh, J. Kwak, Z. Liu, O. Terasaki, R. Ryoo, Ordered nanoporous arrays of carbon supporting high dispersions of platinum nanoparticles, Nature 412(6843) (2001) 169–172.
[60] X. Sun, J. He, J. Tang, T. Wang, Y. Guo, H. Xue, G. Li, Y. Ma, Structural and electrochemical characterization of ordered mesoporous carbon-reduced graphene oxide nanocomposites, Journal of Materials Chemistry 22(21) (2012) 10900–10910.
[61] S. Urbonaite, J.M. Juárez-Galán, J. Leis, F. Rodríguez-Reinoso, G. Svensson, Porosity development along the synthesis of carbons from metal carbides, Microporous and Mesoporous Materials 113(1) (2008) 14–21.

[62] L. Borchardt, F. Hasche, M.R. Lohe, M. Oschatz, F. Schmidt, E. Kockrick, C. Ziegler, T. Lescouet, A. Bachmatiuk, B. Buchner, D. Farrusseng, P. Strasser, S. Kaskel, Transition metal loaded silicon carbide-derived carbons with enhanced catalytic properties, Carbon 50(5) (2012) 1861–1870.
[63] E. Hark, R. Jager, E. Lust, Effect of Platinum Nanoparticle Loading on Oxygen Reduction at a Pt Nanocluster-Activated Microporous-Mesoporous Carbon Support, Electrocatalysis 6(3) (2015) 242–254.
[64] R. Jager, E. Hark, P.E. Kasatkin, E. Lust, Investigation of a Carbon-Supported Pt Electrode for Oxygen Reduction Reaction in 0.1M KOH Aqueous Solution, Journal of the Electrochemical Society 161(9) (2014) F861–F867.
[65] K. Vaarmets, J. Nerut, E. Hark, E. Lust, Electrochemical and physical characterisation of Pt-nanocluster activated molybdenum carbide derived carbon electrodes, Electrochimica Acta 104 (2013) 216–227.
[66] Q. Liu, Y. Peng, Q. Li, T. He, D. Morris, F. Nichols, R. Mercado, P. Zhang, S. Chen, Atomic Dispersion and Surface Enrichment of Palladium in Nitrogen-Doped Porous Carbon Cages Lead to High-Performance Electrocatalytic Reduction of Oxygen, ACS Applied Materials & Interfaces 12(15) (2020) 17641–17650.
[67] L. Perini, C. Durante, M. Favaro, V. Perazzolo, S. Agnoli, O. Schneider, G. Granozzi, A. Gennaro, Metal–Support Interaction in Platinum and Palladium Nanoparticles Loaded on Nitrogen-Doped Mesoporous Carbon for Oxygen Reduction Reaction, ACS Applied Materials & Interfaces 7(2) (2015) 1170–1179.
[68] N. Roy, S. Yasmin, A. Ejaz, H. Soon Han, S. Jeon, Influence of pyrrolic and pyridinic-N in the size and distribution behaviour of Pd nanoparticles and ORR mechanism, Applied Surface Science 533 (2020) 147500.
[69] K. Kakaei, M. Rahnavardi, Synthesis of nitrogen-doped reduced graphene oxide and its decoration with high efficiency palladium nanoparticles for direct ethanol fuel cell, Renewable Energy 163 (2021) 1277–1286.
[70] R. Arrigo, M.E. Schuster, Z. Xie, Y. Yi, G. Wowsnick, L.L. Sun, K.E. Hermann, M. Friedrich, P. Kast, M. Hävecker, A. Knop-Gericke, R. Schlögl, Nature of the N–Pd Interaction in Nitrogen-Doped Carbon Nanotube Catalysts, ACS Catalysis 5(5) (2015) 2740–2753.
[71] S.Z. Zhang, L.K. Wang, L.P. Fang, Y.L. Tian, Y. Tang, X.L. Niu, Y.P. Hao, Z.F. Li, A Facile Method to Prepare Ultrafine Pd Nanoparticles Embedded into N-Doped Porous Carbon Nanosheets as Highly Efficient Electrocatalysts for Oxygen Reduction Reaction, Journal of the Electrochemical Society 167(5) (2020) 054508.
[72] H.J. Huang, S.B. Yang, R. Vajtai, X. Wang, P.M. Ajayan, Pt-Decorated 3D Architectures Built from Graphene and Graphitic Carbon Nitride Nanosheets as Efficient Methanol Oxidation Catalysts, Advanced Materials 26(30) (2014) 5160–5165.
[73] W. Ju, M. Favaro, C. Durante, L. Perini, S. Agnoli, O. Schneider, U. Stimming, G. Granozzi, Pd Nanoparticles deposited on nitrogen-doped HOPG: New Insights into the Pd-catalyzed Oxygen Reduction Reaction, Electrochimica Acta 141 (2014) 89–101.
[74] M. Rezaei, S.H. Tabaian, D.F. Haghshenas, Nucleation and growth of Pd nanoparticles during electrocrystallization on pencil graphite, Electrochimica Acta 59 (2012) 360–366.

[75] S. Salome, R. Rego, A. Querejeta, F. Alcaide, M.C. Oliveira, An electrochemical route to prepare Pd nanostructures on a gas diffusion substrate for a PEMFC, Electrochimica Acta 106 (2013) 516–524.
[76] D. Xu, X.H. Yan, P. Diao, P.G. Yin, Electrodeposition of Vertically Aligned Palladium Nanoneedles and Their Application as Active Substrates for Surface-Enhanced Raman Scattering, Journal of Physical Chemistry C 118(18) (2014) 9758–9768.
[77] H. Naohara, S. Ye, K. Uosaki, Electrochemical deposition of palladium on an Au(111) electrode: effects of adsorbed hydrogen for a growth mode, Colloids and Surfaces a-Physicochemical and Engineering Aspects 154(1–2) (1999) 201–208.
[78] H. Naohara, S. Ye, K. Uosaki, Electrochemical layer-by-layer growth of palladium on an Au(111) electrode surface: Evidence for important role of adsorbed Pd complex, Journal of Physical Chemistry B 102(22) (1998) 4366–4373.
[79] J. Tang, M. Petri, L.A. Kibler, D.M. Kolb, Pd deposition onto Au(111) electrodes from sulphuric acid solution, Electrochimica Acta 51(1) (2005) 125–132.
[80] Y. Soldo-Olivier, M. De Santis, W. Liang, E. Sibert, Growth mechanisms of Pd nanofilms electrodeposited onto Au(111): an in situ grazing incidence X-ray diffraction study, Physical Chemistry Chemical Physics 18(4) (2016) 2830–2839.
[81] J.S. Yu, T. Fujita, A. Inoue, T. Sakurai, M.W. Chen, Electrochemical synthesis of palladium nanostructures with controllable morphology, Nanotechnology 21(8) (2010) 085601.
[82] Y.R. Kim, S.C.S. Lai, K. McKelvey, G.H. Zhang, D. Perry, T.S. Miller, P.R. Unwin, Nucleation and Aggregative Growth of Palladium Nanoparticles on Carbon Electrodes: Experiment and Kinetic Model, Journal of Physical Chemistry C 119(30) (2015) 17389–17397.
[83] K.K. Maniam, V. Muthukumar, R. Chetty, Approaches towards improving the dispersion of electrodeposited palladium on carbon supports, 4 International Conference on Advances in Energy Research (Icaer 2013) 54 (2014) 281–291.
[84] L. Perini, C. Durante, M. Favaro, S. Agnoli, G. Granozzi, A. Gennaro, Electrocatalysis at palladium nanoparticles: Effect of the support nitrogen doping on the catalytic activation of carbonhalogen bond, Applied Catalysis B: Environmental 144 (2014) 300–307.
[85] W. Ju, T. Brülle, M. Favaro, L. Perini, C. Durante, O. Schneider, U. Stimming, Palladium Nanoparticles Supported on Highly Oriented Pyrolytic Graphite: Preparation, Reactivity and Stability, ChemElectroChem 2(4) (2015) 547–558.
[86] Y. Holade, N.E. Sahin, K. Servat, T.W. Napporn, K.B. Kokoh, Recent Advances in Carbon Supported Metal Nanoparticles Preparation for Oxygen Reduction Reaction in Low Temperature Fuel Cells, Catalysts 5(1) (2015) 310–348.
[87] J. Solla-Gullon, V. Montiel, A. Aldaz, J. Clavilier, Electrochemical characterisation of platinum nanoparticles prepared by microemulsion: how to clean them without loss of crystalline surface structure, Journal of Electroanalytical Chemistry 491(1–2) (2000) 69–77.
[88] A. Ejaz, S. Jeon, The individual role of pyrrolic, pyridinic and graphitic nitrogen in the growth kinetics of PdNPs on N-rGO followed by a comprehensive study on ORR, International Journal of Hydrogen Energy 43(11) (2018) 5690–5702.
[89] W. Niu, Z.-Y. Li, L. Shi, X. Liu, H. Li, S. Han, J. Chen, G. Xu, Seed-Mediated Growth of Nearly Monodisperse Palladium Nanocubes with Controllable Sizes, Crystal Growth & Design 8(12) (2008) 4440–4444.

[90] F.J. Vidal-Iglesias, R.M. Arán-Ais, J. Solla-Gullón, E. Garnier, E. Herrero, A. Aldaz, J.M. Feliu, Shape-dependent electrocatalysis: formic acid electrooxidation on cubic Pd nanoparticles, Physical Chemistry Chemical Physics 14(29) (2012) 10258–10265.
[91] A. Zalineeva, S. Baranton, C. Coutanceau, G. Jerkiewicz, Electrochemical Behavior of Unsupported Shaped Palladium Nanoparticles, Langmuir 31(5) (2015) 1605–1609.
[92] B. Lim, M. Jiang, J. Tao, P.H.C. Camargo, Y. Zhu, Y. Xia, Shape-Controlled Synthesis of Pd Nanocrystals in Aqueous Solutions, Advanced Functional Materials 19(2) (2009) 189–200.
[93] M.S. Jin, H.Y. Liu, H. Zhang, Z.X. Xie, J.Y. Liu, Y.N. Xia, Synthesis of Pd Nanocrystals Enclosed by {100} Facets and with Sizes < 10 nm for Application in CO Oxidation, Nano Research 4(1) (2011) 83–91.
[94] X. Li, X. Peng, Y. Wang, B. Yan, Synthesis of Pd nanonetworks with abundant defects for oxygen reduction electrocatalysis, New Journal of Chemistry 45(5) (2021) 2814–2819.
[95] Y. Wang, Z. Zhu, K. Xu, W. Guo, T. Yu, M. He, W. Wei, T. Yang, Palladium Nanobelts with Expanded Lattice Spacing for Electrochemical Oxygen Reduction in Alkaline Media, ACS Applied Nano Materials 4(2) (2021) 2118–2125.
[96] H. Yu, T. Zhou, Z. Wang, Y. Xu, X. Li, L. Wang, H. Wang, Defect-Rich Porous Palladium Metallene for Enhanced Alkaline Oxygen Reduction Electrocatalysis, Angewandte Chemie International Edition 60(21) (2021) 12027–12031.
[97] L.A. Porter, H.C. Choi, A.E. Ribbe, J.M. Buriak, Controlled electroless deposition of noble metal nanoparticle films on germanium surfaces, Nano Letters 2(10) (2002) 1067–1071.
[98] L.B. Sheridan, J. Czerwiniski, N. Jayaraju, D.K. Gebregziabiher, J.L. Stickney, D.B. Robinson, M.P. Soriaga, Electrochemical Atomic Layer Deposition (E-ALD) of Palladium Nanofilms by Surface Limited Redox Replacement (SLRR), with EDTA Complexation, Electrocatalysis 3(2) (2012) 96–107.
[99] M. Mohl, D. Dobo, A. Kukovecz, Z. Konya, K. Kordas, J.Q. Wei, R. Vajtai, P.M. Ajayan, Formation of CuPd and CuPt Bimetallic Nanotubes by Galvanic Replacement Reaction, Journal of Physical Chemistry C 115(19) (2011) 9403–9409.
[100] S. Baek, K.H. Kim, M.J. Kim, J.J. Kim, Morphology control of noble metal catalysts from planar to dendritic shapes by galvanic displacement, Applied Catalysis B-Environmental 217 (2017) 313–321.
[101] A. Papaderakis, I. Mintsouli, J. Georgieva, S. Sotiropoulos, Electrocatalysts Prepared by Galvanic Replacement, Catalysts 7(3) (2017) 80.
[102] L.B. Sheridan, D.K. Gebregziabiher, J.L. Stickney, D.B. Robinson, Formation of Palladium Nanofilms Using Electrochemical Atomic Layer Deposition (E-ALD) with Chloride Complexation, Langmuir 29(5) (2013) 1592–1600.
[103] S. Takahashi, N. Takahashi, N. Todoroki, T. Wadayama, Dealloying of Nitrogen-Introduced Pt–Co Alloy Nanoparticles: Preferential Core–Shell Formation with Enhanced Activity for Oxygen Reduction Reaction, ACS Omega 1(6) (2016) 1247–1252.
[104] B. Ha, O.H. Han, Platinum-catalyzed carbon nanotubes for durability enhancement of low-temperature fuel cells, Journal of Power Sources 223 (2013) 246–253.

[105] S. St. John, R.W. Atkinson, O. Dyck, C.-J. Sun, T.A. Zawodzinski, A.B. Papandrew, Segregated Pt on Pd nanotubes for enhanced oxygen reduction activity in alkaline electrolyte, Chemical Communications 51(93) (2015) 16633–16636.
[106] A.A. Dameron, S. Pylypenko, J.B. Bult, K.C. Neyerlin, C. Engtrakul, C. Bochert, G.J. Leong, S.L. Frisco, L. Simpson, H.N. Dinh, B. Pivovar, Aligned carbon nanotube array functionalization for enhanced atomic layer deposition of platinum electrocatalysts, Applied Surface Science 258(13) (2012) 5212–5221.
[107] T. Shu, S.-J. Liao, C.-T. Hsieh, A.K. Roy, Y.-Y. Liu, D.-Y. Tzou, W.-Y. Chen, Fabrication of platinum electrocatalysts on carbon nanotubes using atomic layer deposition for proton exchange membrane fuel cells, Electrochimica Acta 75 (2012) 101–107.
[108] M.A. Khalily, B. Patil, E. Yilmaz, T. Uyar, Atomic Layer Deposition of Pd Nanoparticles on N-Doped Electrospun Carbon Nanofibers: Optimization of ORR Activity of Pd-Based Nanocatalysts by Tuning Their Nanoparticle Size and Loading, ChemNanoMat 5(12) (2019) 1540–1546.
[109] A.R. Van Wassen, M.J. Murphy, A. Molina Villarino, C.N. Gannett, R.B. van Dover, H.D. Abruña, Electrochemical Screening of Metallic Oxygen Reduction Reaction Catalyst Thin Films Using Getter Cosputtering, ACS Combinatorial Science 22(7) (2020) 339–347.
[110] J.S. Cooper, P.J. McGinn, Combinatorial screening of fuel cell cathode catalyst compositions, Applied Surface Science 254(3) (2007) 662–668.
[111] M. Käärik, M. Arulepp, M. Kook, U. Mäeorg, J. Kozlova, V. Sammelselg, A. Perkson, J. Leis, Characterisation of steam-treated nanoporous carbide-derived carbon of TiC origin: structure and enhanced electrochemical performance, Journal of Porous Materials 25(4) (2018) 1057–1070.
[112] S. Hussain, H. Erikson, N. Kongi, A. Treshchalov, M. Rahn, M. Kook, M. Merisalu, L. Matisen, V. Sammelselg, K. Tammeveski, Oxygen Electroreduction on Pt Nanoparticles Deposited on Reduced Graphene Oxide and N-doped Reduced Graphene Oxide Prepared by Plasma-assisted Synthesis in Aqueous Solution, Chemelectrochem 5(19) (2018) 2902–2911.
[113] A. Treshchalov, H. Erikson, L. Puust, S. Tsarenko, R. Saar, A. Vanetsev, K. Tammeveski, I. Sildos, Stabilizer-free silver nanoparticles as efficient catalysts for electrochemical reduction of oxygen, Journal of Colloid and Interface Science 491 (2017) 358–366.
[114] F. Li, Y. Bao, J. Chai, Q. Zhang, D. Han, L. Niu, Synthesis and Application of Widely Soluble Graphene Sheets, Langmuir 26(14) (2010) 12314–12320.
[115] A.J. Bard, L.R. Faulkner, Electrochemical Methods, Wiley, New York, 2001.
[116] D.R. Lide, CRC handbook of chemistry, physics, CRC Press, Boca Raton, 2001.
[117] S. Gottesfeld, I.D. Raistrick, S. Srinivasan, Oxygen Reduction Kinetics on a Platinum RDE Coated with a Recast Nafion Film, Journal of The Electrochemical Society 134(6) (1987) 1455–1462.
[118] R.R. Adžić, J. Wang, B.M. Ocko, Structure of metal adlayers during the course of electrocatalytic reactions: O2 reduction on Au(111) with Tl adlayers in acid solutions, Electrochimica Acta 40(1) (1995) 83–89.
[119] R.E. Davis, G.L. Horvath, C.W. Tobias, The solubility and diffusion coefficient of oxygen in potassium hydroxide solutions, Electrochimica Acta 12(3) (1967) 287–297.

[120] A.G. Wright, J. Fan, B. Britton, T. Weissbach, H.-F. Lee, E.A. Kitching, T.J. Peckham, S. Holdcroft, Hexamethyl-p-terphenyl poly(benzimidazolium): a universal hydroxide-conducting polymer for energy conversion devices, Energy & Environmental Science 9(6) (2016) 2130–2142.
[121] S. Mukerjee, J. McBreen, Effect of particle size on the electrocatalysis by carbon-supported Pt electrocatalysts: an in situ XAS investigation, Journal of Electroanalytical Chemistry 448(2) (1998) 163–171.
[122] K.J.J. Mayrhofer, B.B. Blizanac, M. Arenz, V.R. Stamenkovic, P.N. Ross, N.M. Markovic, The Impact of Geometric and Surface Electronic Properties of Pt-Catalysts on the Particle Size Effect in Electrocatalysis, The Journal of Physical Chemistry B 109(30) (2005) 14433–14440.
[123] N. Hoshi, M. Nakamura, N. Maki, S. Yamaguchi, A. Kitajima, Structural effects on voltammograms of the low index planes of palladium and Pd(S)-[n(100)×(111)] surfaces in alkaline solution, Journal of Electroanalytical Chemistry 624(1) (2008) 134–138.
[124] A. López-Cudero, J. Solla-Gullón, E. Herrero, A. Aldaz, J.M. Feliu, CO electro-oxidation on carbon supported platinum nanoparticles: Effect of aggregation, Journal of Electroanalytical Chemistry 644(2) (2010) 117–126.
[125] M. Grden, M. Lukaszewski, G. Jerkiewicz, A. Czerwinski, Electrochemical behaviour of palladium electrode: Oxidation, electrodissolution and ionic adsorption, Electrochimica Acta 53(26) (2008) 7583–7598.
[126] M. Góral-Kurbiel, A. Drelinkiewicz, R. Kosydar, J. Gurgul, B. Dembińska, P.J. Kulesza, The effect of Nafion ionomer on electroactivity of palladium–polypyrrole catalysts for oxygen reduction reaction, Journal of Solid State Electrochemistry 18(3) (2014) 639–653.
[127] H. Guo, D.H. Wen, T. Wang, X.L. Fan, L. Song, H. Gong, W. Xia, B. Gao, L.H. Li, J.P. He, In situ palladium/nitrogen-doped ordered mesoporous carbon hybrids as highly active and durable electrocatalysts for oxygen reduction reaction, Journal of Porous Materials 26(2) (2019) 371–379.
[128] E. Gracia-Espino, X. Jia, T. Wågberg, Improved Oxygen Reduction Performance of Pt–Ni Nanoparticles by Adhesion on Nitrogen-Doped Graphene, The Journal of Physical Chemistry C 118(5) (2014) 2804–2811.
[129] N. Alexeyeva, E. Shulga, V. Kisand, I. Kink, K. Tammeveski, Electroreduction of oxygen on nitrogen-doped carbon nanotube modified glassy carbon electrodes in acid and alkaline solutions, Journal of Electroanalytical Chemistry 648(2) (2010) 169–175.
[130] X. Wang, Z. Chen, S. Chen, H. Wang, M. Huang, Nitrogen and Oxygen Co-Doping Assisted Synthesis of Highly Dispersed Pd Nanoparticles on Hollow Carbon Spheres as Efficient Electrocatalysts for Oxygen Reduction Reaction, Chemistry – A European Journal 26(55) (2020) 12589–12595.
[131] J. Cao, Y. Hu, L. Chen, J. Xu, Z. Chen, Nitrogen-doped carbon quantum dot/ graphene hybrid nanocomposite as an efficient catalyst support for the oxygen reduction reaction, International Journal of Hydrogen Energy 42(5) (2017) 2931–2942.
[132] G.F. Alvarez, M. Mamlouk, S.M.S. Kumar, K. Scott, Preparation and characterisation of carbon-supported palladium nanoparticles for oxygen reduction in low temperature PEM fuel cells, Journal of Applied Electrochemistry 41(8) (2011) 925–937.

[133] L.M. Vracar, D.B. Sepa, A. Damjanovic, Palladium Electrode in Oxygen – Saturated Aqueous Solutions: Potential Dependent Adsorption of Oxygen Containing Species and Their Effect on Oxygen Reduction, Journal of The Electrochemical Society 136(7) (1989) 1973–1977.
[134] M. Shao, T. Yu, J.H. Odell, M. Jin, Y. Xia, Structural dependence of oxygen reduction reaction on palladium nanocrystals, Chemical Communications 47(23) (2011) 6566–6568.
[135] S. Kabir, A. Serov, K. Artyushkova, P. Atanassov, Nitrogen-Doped Three-Dimensional Graphene-Supported Palladium Nanocomposites: High-Performance Cathode Catalysts for Oxygen Reduction Reactions, Acs Catalysis 7(10) (2017) 6609–6618.
[136] P. Zhang, R. Wang, T. Xiao, Z. Chang, Z. Fang, Z. Zhu, C. Xu, L. Wang, J. Cheng, The High-Performance Bifunctional Catalyst Pd/Ti3C2Tx–Carbon Nanotube for Oxygen Reduction Reaction and Hydrogen Evolution Reaction in Alkaline Medium, Energy Technology 8(7) (2020) 2000306.
[137] H. Erikson, A. Sarapuu, K. Tammeveski, J. Solla-Gullón, J.M. Feliu, Enhanced electrocatalytic activity of cubic Pd nanoparticles towards the oxygen reduction reaction in acid media, Electrochemistry Communications 13(7) (2011) 734–737.
[138] N. Naresh, F.G.S. Wasim, B.P. Ladewig, M. Neergat, Removal of surfactant and capping agent from Pd nanocubes (Pd-NCs) using tert-butylamine: its effect on electrochemical characteristics, Journal of Materials Chemistry A 1(30) (2013) 8553–8559.
[139] A. Sadezky, H. Muckenhuber, H. Grothe, R. Niessner, U. Poschl, Raman micro spectroscopy of soot and related carbonaceous materials: Spectral analysis and structural information, Carbon 43(8) (2005) 1731–1742.
[140] A.C. Ferrari, J. Robertson, Interpretation of Raman spectra of disordered and amorphous carbon, Physical Review B 61(20) (2000) 14095–14107.
[141] M. Hara, U. Linke, T. Wandlowski, Preparation and electrochemical characterization of palladium single crystal electrodes in 0.1 M H2SO4 and HClO4 part I. Low-index phases, Electrochimica Acta 52(18) (2007) 5733–5748.
[142] H. Yano, E. Higuchi, H. Uchida, M. Watanabe, Temperature dependence of oxygen reduction activity at Nafion-coated bulk Pt and Pt/carbon black catalysts, Journal of Physical Chemistry B 110(33) (2006) 16544–16549.
[143] G. Wu, A. Santandreu, W. Kellogg, S. Gupta, O. Ogoke, H. Zhang, H.-L. Wang, L. Dai, Carbon nanocomposite catalysts for oxygen reduction and evolution reactions: From nitrogen doping to transition-metal addition, Nano Energy 29 (2016) 83–110.
[144] L.H. Mendoza-Huizar, D. Garrido-Marquez, C.H. Rios-Reyes, M. Rivera, E. Garcia-Sanchez, C. Galan-Vidal, A Kinetic and AFM Study of the Electrodeposition of Palladium Nanoclusters onto Highly Oriented Pyrolytic Graphite (HOPG), Journal of Cluster Science 26(2) (2015) 337–346.
[145] S.Q. Zhu, X.M. Hu, M.H. Shao, Impacts of anions on the oxygen reduction reaction kinetics on platinum and palladium surfaces in alkaline solutions, Physical Chemistry Chemical Physics 19(11) (2017) 7631–7641.
[146] S. Gok, Y. Kim, T. Lim, H.J. Kim, O.J. Kwon, Performance of Pd Cathode Catalyst Electrodeposited on Gas Diffusion Layer in Polymer Electrolyte Membrane Fuel Cells, Electrocatalysis 9(1) (2018) 59–66.

[147] K.K. Maniam, V. Muthukumar, R. Chetty, Approaches towards Improving the Dispersion of Electrodeposited Palladium on Carbon Supports, Energy Procedia 54 (2014) 281–291.
[148] B.Z. Liu, M. Wang, Preparation and characterization of size-controlled silver nanoparticles decorated multi-walled carbon nanotubes and their electrocatalytic reduction properties for hydrogen peroxide, Russian Journal of Electrochemistry 50(5) (2014) 476–481.
[149] T. Kar, R. Devivaraprasad, B. Bera, R. Ramesh, M. Neergat, Investigation on the reduction of the oxides of Pd and graphite in alkaline medium and the simultaneous evolution of oxygen reduction reaction and peroxide generation features, Electrochimica Acta 191 (2016) 81–89.
[150] N. Alexeyeva, K. Tammeveski, Electrochemical reduction of oxygen on multi-walled carbon nanotube modified glassy carbon electrodes in acid media, Electrochemical and Solid State Letters 10(5) (2007) F18–F21.
[151] C.P. Deming, R. Mercado, V. Gadiraju, S.W. Sweeney, M. Khan, S.W. Chen, Graphene Quantum Dots-Supported Palladium Nanoparticles for Efficient Electrocatalytic Reduction of Oxygen in Alkaline Media, Acs Sustainable Chemistry & Engineering 3(12) (2015) 3315–3323.
[152] K. Jukk, N. Alexeyeva, C. Johans, K. Kontturi, K. Tammeveski, Oxygen reduction on Pd nanoparticle/multi-walled carbon nanotube composites, Journal of Electroanalytical Chemistry 666 (2012) 67–75.
[153] Y.H. Lin, X.L. Cui, X.R. Ye, Electrocatalytic reactivity for oxygen reduction of palladium-modified carbon nanotubes synthesized in supercritical fluid, Electrochemistry Communications 7(3) (2005) 267–274.
[154] C.-T. Hsieh, Y.-Y. Liu, A.K. Roy, Pulse electrodeposited Pd nanoclusters on graphene-based electrodes for proton exchange membrane fuel cells, Electrochimica Acta 64(Supplement C) (2012) 205–210.
[155] C.T. Hsieh, J.L. Gu, Y.C. Chen, D.Y. Tzou, Pulse microwave synthesis of palladium catalysts on graphene electrodes for proton exchange membrane fuel cells, Electrochimica Acta 98 (2013) 39–47.
[156] K. Jukk, N. Kongi, L. Matisen, T. Kallio, K. Kontturi, K. Tammeveski, Electroreduction of oxygen on palladium nanoparticles supported on nitrogen-doped graphene nanosheets, Electrochimica Acta 137 (2014) 206–212.
[157] Y. Lou, J. Xu, H. Wu, J. Liu, Hollow carbon anchored highly dispersed Pd species for selective hydrogenation of 3-nitrostyrene: metal-carbon interaction, Chemical Communications 54(94) (2018) 13248–13251.
[158] H. Yang, Y. Ko, W. Lee, A. Züttel, W. Kim, Nitrogen-doped carbon black supported Pt–M (M = Pd, Fe, Ni) alloy catalysts for oxygen reduction reaction in proton exchange membrane fuel cell, Materials Today Energy 13 (2019) 374–381.
[159] M. Hasik, A. Bernasik, A. Drelinkiewicz, K. Kowalski, E. Wenda, J. Camra, XPS studies of nitrogen-containing conjugated polymers–palladium systems, Surface Science 507–510 (2002) 916–921.
[160] B.P. Vinayan, K. Sethupathi, S. Ramaprabhu, Facile synthesis of triangular shaped palladium nanoparticles decorated nitrogen doped graphene and their catalytic study for renewable energy applications, International Journal of Hydrogen Energy 38(5) (2013) 2240–2250.
[161] M.A. Molina-García, N.V. Rees, Effect of catalyst carbon supports on the oxygen reduction reaction in alkaline media: a comparative study, RSC Advances 6(97) (2016) 94669–94681.

[162] C. Zhang, S. Yu, Y. Xie, W. Zhang, K. Zheng, N.E. Drewett, S.J. Yoo, Z. Wang, L. Shao, H. Tian, J.-G. Kim, W. Zheng, Suppressing the Pd-C interaction through B-doping for highly efficient oxygen reduction, Carbon 149 (2019) 370–379.
[163] N.N. Kariuki, X.P. Wang, J.R. Mawdsley, M.S. Ferrandon, S.G. Niyogi, J.T. Vaughey, D.J. Myers, Colloidal Synthesis and Characterization of Carbon-Supported Pd-Cu Nanoparticle Oxygen Reduction Electrocatalysts, Chemistry of Materials 22(14) (2010) 4144–4152.
[164] H. Erikson, A. Sarapuu, J. Kozlova, L. Matisen, V. Sammelselg, K. Tammeveski, Oxygen Electroreduction on Electrodeposited PdAu Nanoalloys, Electrocatalysis 6(1) (2015) 77–85.
[165] O. Ghodbane, L. Roue, D. Belanger, Study of the electroless deposition of Pd on Cu-modified graphite electrodes by metal exchange reaction, Chemistry of Materials 20(10) (2008) 3495–3504.
[166] A. Sarapuu, A. Kasikov, T. Laaksonen, K. Kontturi, K. Tammeveski, Electrochemical reduction of oxygen on thin-film Pt electrodes in acid solutions, Electrochimica Acta 53(20) (2008) 5873–5880.
[167] H. Erikson, A. Kasikov, C. Johans, K. Kontturi, K. Tammeveski, A. Sarapuu, Oxygen reduction on Nafion-coated thin-film palladium electrodes, Journal of Electroanalytical Chemistry 652(1–2) (2011) 1–7.
[168] H. Erikson, M. Liik, A. Sarapuu, J. Kozlova, V. Sammelselg, K. Tammeveski, Oxygen reduction on electrodeposited Pd coatings on glassy carbon, Electrochimica Acta 88 (2013) 513–518.

9. SUMMARY IN ESTONIAN

Hapniku elektroredutseerumine nanostruktuursetel pallaadiumkatalüsaatoritel

Doktoritöö eesmärk oli uurida nanostruktuursete Pd katalüsaatorite elektrokatalüütilist aktiivsust hapniku redutseerumisel nii happelises kui ka aluselises keskkonnas. Elektrokeemilised mõõtmised viidi läbi väävel- ja perkloorhappe ning kaaliumhüdroksiidi lahuses kasutades tsüklilise voltamperomeetria ja pöörleva ketaselektroodi meetodeid. Pd katalüsaatorid valmistati füüsikalise, keemilise ja elektrokeemilise sadestamise teel.

Esimeses osas uuriti kommertsiaalset päritolu (Pajarito Powder) lämmastikuga dopeeritud mesopoorseid süsinikmaterjale pallaadiumkatalüsaatori kandjana. Pd nanoosakesed valmistati tsitraadimeetodil ja dispergeeriti alusmaterjalidele. Lämmastikuga dopeeritud materjalidele kantud Pd nanoosakesed näitasid kõrgemat eriaktiivsust happelises keskkonnas ja sarnast eriaktiivsust aluselises keskkonnas võrreldes Vulcan süsinikule sadestatud Pd katalüsaatoriga. N-dopeeritud süsinikmaterjalidele kantud Pd katalüsaator näitas kõrget jõudlust, kui seda kasutati anioonvahetusmembraaniga kütuseelemendi katoodina.

Töö teises osas uuriti kuubikujulisi Pd nanoosakesi, mille alusmaterjaliks oli Vulcan süsinik, ja võrreldi neid sfääriliste Pd nanoosakestega. Võrdlus viidi läbi nii aluselises kui happelises keskkonnas ning mõlemal juhul näitasid suuremat eriaktiivsust kuubikujulised Pd osakesed. Kuna sfäärikujulised osakesed olid väiksemad kui kuubikujulised, siis massaktiivsus oli kõrgem sfäärikujulistel osakestel.

Järgnevalt sadestati Pd erinevatele karbiidset päritolu poorsetele süsinikmaterjalidele kasutades boorhüdriidi meetodit. Kõige ühtlasem Pd osakeste jaotus ja väikseim osakeste suurus saavutati süsinikmaterjalil, millel oli kõige rohkem mikropoore. Nii happelises kui ka aluselises keskkonnas andsid Pd/CDC materjalid paremaid eriaktiivsusi võrreldes Pd/Vulcan katalüsaatormaterjaliga.

Neljandas osas kasutati Pd nanoosakeste sadestamiseks erinevatele süsiniknanomaterjalidele elektrosadestamise meetodit. Sadestamisel suuremal ülepingel tekkis rohkem väikseid Pd osakesi alusmaterjali pinnale. Süsiniknanotorudele sadestamine ei olnud efektiivne, mistõttu kasutati elektrokeemilist aktivatsiooni, mis andis parema Pd nanoosakeste jaotuse süsiniknanotorudel. Selles töö osas sadestatud materjalidest oli kõige suurem elektrokeemiliselt aktiivne pindala ja üks kõrgematest eriaktiivsuse väärtustest grafeenile sadestatud Pd nanoosakestel, millest võiks järeldada, et grafeeni nanoliistakud on hea alusmaterjal Pd elektrosadestatud osakestele.

Järgmises töö osas uuriti plasma meetodil sünteesitud Pd/C katalüsaatoreid. Lämmastikuga dopeeritud ja dopeerimata grafeenoksiidi võrreldi katalüsaatorikandjana Vulcan süsinikuga. Sadestusprotsessi käigus redutseeriti ka grafeenoksiid rGO-ks. Kõige väiksemaid Pd osakesi täheldati lämmastikuga dopeeritud alusmaterjalil, aga eriaktiivsused olid võrreldavad mõlemal grafeenipõhisel alusmaterjalil, kuid jäid madalamaks kui Pd/Vulcan katalüsaatori eriaktiivsus.

Viimases osas kasutati Pd sadestamiseks vase galvaanilist vahetust. Õhukesed Cu kiled sadestati klaassüsinikelektroodidele elektronkiirtega aurustamise meetodil, varieerides kilede paksust vahemikus 0,5 kuni 10 nm. Pärast Pd sadestamist oli Cu detekteeritav EDX meetodil vaid 5 ja 10 nm kilede korral, samas kui pinnatundlike XPS ja tsüklilise voltaperomeetria meetodi puhul ei täheldatud vaske üheski neist materjalidest. Pd eriaktiivsus tõusis kile paksenedes, mis võib tuleneda sellest, et suuremad Pd osakesed on sageli aktiivsemad aluselises keskkonnas.

Kõik selles töös pöörleva ketaselektroodi meetodil kogutud hapniku redutseerumise andmed analüüsiti, kasutades Koutecky-Levichi võrrandit. Sellest analüüsist leiti üleminevate elektronide arv O_2 molekuli kohta. Enamiku Pd katalüsaatorite korral oli *n*-i väärtus 4, kuid väikese Pd koguse puhul täheldati ka madalamaid väärtusi. Saadud tulemuste põhjal saab järeldada, et hapniku elektroredutseerumine Pd katalüsaatoritel toimub valdavalt 4-elektronilise protsessina. Reaktsiooni limiteerivat staadiumit hinnati Tafeli tõusu väärtuse alusel. Enamik katalüsaatormaterjale andsid kompaktsele Pd-elektroodile sarnased Tafel tõusu väärtused ning hapniku redutseerumisreaktsiooni limiteerib esimese elektroni aeglane ülekanne O_2 molekulile.

10. ACKNOWLEDGEMENTS

First I would like to thank my supervisors Dr. Heiki Erikson and Assoc. Prof. Kaido Tammeveski for their time and advice, which helped me through my academic studies.

I would like to thank some of the staff at the Institute of Physics, who helped with physical characterisations and catalyst preparation. Dr. Aarne Kasikov prepared thin Cu films and Dr. Aleksei Treštšalov prepared Pd nanoparticles using the plasma method and conducted Raman spectroscopy measurements. Prof. Väino Sammelselg and his co-workers performed SEM, EDX, TEM and XPS measurements.

I am grateful to Dr. Jose Solla-Gullon and Prof. Juan M. Feliu who helped with nanoparticle synthesis on different mesoporous N-doped carbon materials during my stay in Alicante, Spain.

I would also like to thank my colleagues from the Institute of Chemistry.

This work has been supported by Estonian Research Council (Grant PRG723 and Grant No. 9323) and by the EU through the European Regional Development Fund (TK141, 'Advanced materials and high-technology devices for energy recuperation systems'). Furthermore, this work was supported by institutional research funding (IUT20-16, IUT2-24 and IUT34-14).

I am also grateful to my parents and grandparents for their support.

11. PUBLICATIONS

CURRICULUM VITAE

Name:	Madis Lüsi
Born:	March 14, 1991
Citizenship:	Estonian
Address:	Ravila 14a, 50411 Tartu, Estonia
Phone:	+372 5340 8190
E-mail:	madis.lusi@ut.ee

Education:

From 2017 –	University of Tartu, Faculty of Science and Technology, PhD student
2015–2017	University of Tartu, Faculty of Science and Technology, MSc (in chemistry) 2017.
2010–2015	University of Tartu, Faculty of Science and Technology, BSc (in chemistry) 2015.

Major scientific Publications:

H. Erikson, M. Lüsi, A. Sarapuu, K. Tammeveski, J. Solla-Gullon, J.M. Feliu, Oxygen electroreduction on carbon-supported Pd nanocubes in acid solutions, *Electrochimica Acta* 188 (2016) 301–308.

M. Lüsi, H. Erikson, A. Sarapuu, K. Tammeveski, J. Solla-Gullon, J.M. Feliu, Oxygen reduction reaction on carbon-supported palladium nanocubes in alkaline media, *Electrochemistry Communications* 64 (2016) 9–13.

M. Lüsi, H. Erikson, A. Sarapuu, M. Merisalu, M. Rähn, A. Treshchalov, P. Paiste, M. Käärik, J. Leis, V. Sammelselg, T. Kaljuvee, K. Tammeveski, Electroreduction of Oxygen on Carbide-Derived Carbon Supported Pd Catalysts, *ChemElectroChem* 7(2) (2020) 546–554.

M. Lüsi, H. Erikson, M. Merisalu, M. Rähn, V. Sammelselg, K. Tammeveski, Electrochemical reduction of oxygen in alkaline solution on Pd/C catalysts prepared by electrodeposition on various carbon nanomaterials, *Journal of Electroanalytical Chemistry* 834 (2019) 223–232.

M. Lüsi, H. Erikson, A. Treshchalov, M. Rähn, M. Merisalu, A. Kikas, V. Kisand, V. Sammelselg, K. Tammeveski, Oxygen reduction reaction on Pd nanocatalysts prepared by plasma-assisted synthesis on different carbon nanomaterials, *Nanotechnology* 32(3) (2020) 035401.

M. Lüsi, H. Erikson, M. Merisalu, A. Kasikov, L. Matisen, V. Sammelselg, K. Tammeveski, Oxygen Electroreduction in Alkaline Solution on Pd Coatings Prepared by Galvanic Exchange of Copper, *Electrocatalysis* 9(3) (2018) 400–408.

ELULOOKIRJELDUS

Nimi: Madis Lüsi
Sünniaeg: 14.03.1991
Kodakondsus: Eesti
Aadress: Ravila 14a, 50411 Tartu, Eesti
Telefon: +372 5340 8190
E-post: madis.lusi@ut.ee

Haridus:

Alates 2017 – Tartu Ülikool, Loodus- ja täppisteaduste valdkond, doktoriõppe üliõpilane.

2015–2017 Tartu Ülikool, Loodus- ja täppisteaduste valdkond, MSc (keemia) 2017.

2010–2015 Tartu Ülikool, Loodus- ja täppisteaduste valdkond, BSc (keemia) 2015.

Publikatsioonide loetelu:

H. Erikson, M. Lüsi, A. Sarapuu, K. Tammeveski, J. Solla-Gullon, J.M. Feliu, Oxygen electroreduction on carbon-supported Pd nanocubes in acid solutions, *Electrochimica Acta* 188 (2016) 301–308.

M. Lüsi, H. Erikson, A. Sarapuu, K. Tammeveski, J. Solla-Gullon, J.M. Feliu, Oxygen reduction reaction on carbon-supported palladium nanocubes in alkaline media, *Electrochemistry Communications* 64 (2016) 9–13.

M. Lüsi, H. Erikson, A. Sarapuu, M. Merisalu, M. Rähn, A. Treshchalov, P. Paiste, M. Käärik, J. Leis, V. Sammelselg, T. Kaljuvee, K. Tammeveski, Electroreduction of Oxygen on Carbide-Derived Carbon Supported Pd Catalysts, *ChemElectroChem* 7(2) (2020) 546–554.

M. Lüsi, H. Erikson, M. Merisalu, M. Rahn, V. Sammelselg, K. Tammeveski, Electrochemical reduction of oxygen in alkaline solution on Pd/C catalysts prepared by electrodeposition on various carbon nanomaterials, *Journal of Electroanalytical Chemistry* 834 (2019) 223–232.

M. Lüsi, H. Erikson, A. Treshchalov, M. Rähn, M. Merisalu, A. Kikas, V. Kisand, V. Sammelselg, K. Tammeveski, Oxygen reduction reaction on Pd nanocatalysts prepared by plasma-assisted synthesis on different carbon nanomaterials, *Nanotechnology* 32(3) (2020) 035401.

M. Lüsi, H. Erikson, M. Merisalu, A. Kasikov, L. Matisen, V. Sammelselg, K. Tammeveski, Oxygen Electroreduction in Alkaline Solution on Pd Coatings Prepared by Galvanic Exchange of Copper, *Electrocatalysis* 9(3) (2018) 400–408.

DISSERTATIONES CHIMICAE UNIVERSITATIS TARTUENSIS

1. **Toomas Tamm.** Quantum-chemical simulation of solvent effects. Tartu, 1993, 110 p.
2. **Peeter Burk.** Theoretical study of gas-phase acid-base equilibria. Tartu, 1994, 96 p.
3. **Victor Lobanov.** Quantitative structure-property relationships in large descriptor spaces. Tartu, 1995, 135 p.
4. **Vahur Mäemets.** The ^{17}O and ^{1}H nuclear magnetic resonance study of H_2O in individual solvents and its charged clusters in aqueous solutions of electrolytes. Tartu, 1997, 140 p.
5. **Andrus Metsala.** Microcanonical rate constant in nonequilibrium distribution of vibrational energy and in restricted intramolecular vibrational energy redistribution on the basis of slater's theory of unimolecular reactions. Tartu, 1997, 150 p.
6. **Uko Maran.** Quantum-mechanical study of potential energy surfaces in different environments. Tartu, 1997, 137 p.
7. **Alar Jänes.** Adsorption of organic compounds on antimony, bismuth and cadmium electrodes. Tartu, 1998, 219 p.
8. **Kaido Tammeveski.** Oxygen electroreduction on thin platinum films and the electrochemical detection of superoxide anion. Tartu, 1998, 139 p.
9. **Ivo Leito.** Studies of Brønsted acid-base equilibria in water and non-aqueous media. Tartu, 1998, 101 p.
10. **Jaan Leis.** Conformational dynamics and equilibria in amides. Tartu, 1998, 131 p.
11. **Toonika Rinken.** The modelling of amperometric biosensors based on oxidoreductases. Tartu, 2000, 108 p.
12. **Dmitri Panov.** Partially solvated Grignard reagents. Tartu, 2000, 64 p.
13. **Kaja Orupõld.** Treatment and analysis of phenolic wastewater with microorganisms. Tartu, 2000, 123 p.
14. **Jüri Ivask.** Ion Chromatographic determination of major anions and cations in polar ice core. Tartu, 2000, 85 p.
15. **Lauri Vares.** Stereoselective Synthesis of Tetrahydrofuran and Tetrahydropyran Derivatives by Use of Asymmetric Horner-Wadsworth-Emmons and Ring Closure Reactions. Tartu, 2000, 184 p.
16. **Martin Lepiku.** Kinetic aspects of dopamine D_2 receptor interactions with specific ligands. Tartu, 2000, 81 p.
17. **Katrin Sak.** Some aspects of ligand specificity of P2Y receptors. Tartu, 2000, 106 p.
18. **Vello Pällin.** The role of solvation in the formation of iotsitch complexes. Tartu, 2001, 95 p.
19. **Katrin Kollist.** Interactions between polycyclic aromatic compounds and humic substances. Tartu, 2001, 93 p.

20. **Ivar Koppel.** Quantum chemical study of acidity of strong and superstrong Brønsted acids. Tartu, 2001, 104 p.
21. **Viljar Pihl.** The study of the substituent and solvent effects on the acidity of OH and CH acids. Tartu, 2001, 132 p.
22. **Natalia Palm.** Specification of the minimum, sufficient and significant set of descriptors for general description of solvent effects. Tartu, 2001, 134 p.
23. **Sulev Sild.** QSPR/QSAR approaches for complex molecular systems. Tartu, 2001, 134 p.
24. **Ruslan Petrukhin.** Industrial applications of the quantitative structure-property relationships. Tartu, 2001, 162 p.
25. **Boris V. Rogovoy.** Synthesis of (benzotriazolyl)carboximidamides and their application in relations with *N*- and *S*-nucleophyles. Tartu, 2002, 84 p.
26. **Koit Herodes.** Solvent effects on UV-vis absorption spectra of some solvatochromic substances in binary solvent mixtures: the preferential solvation model. Tartu, 2002, 102 p.
27. **Anti Perkson.** Synthesis and characterisation of nanostructured carbon. Tartu, 2002, 152 p.
28. **Ivari Kaljurand.** Self-consistent acidity scales of neutral and cationic Brønsted acids in acetonitrile and tetrahydrofuran. Tartu, 2003, 108 p.
29. **Karmen Lust.** Adsorption of anions on bismuth single crystal electrodes. Tartu, 2003, 128 p.
30. **Mare Piirsalu.** Substituent, temperature and solvent effects on the alkaline hydrolysis of substituted phenyl and alkyl esters of benzoic acid. Tartu, 2003, 156 p.
31. **Meeri Sassian.** Reactions of partially solvated Grignard reagents. Tartu, 2003, 78 p.
32. **Tarmo Tamm.** Quantum chemical modelling of polypyrrole. Tartu, 2003. 100 p.
33. **Erik Teinemaa.** The environmental fate of the particulate matter and organic pollutants from an oil shale power plant. Tartu, 2003. 102 p.
34. **Jaana Tammiku-Taul.** Quantum chemical study of the properties of Grignard reagents. Tartu, 2003. 120 p.
35. **Andre Lomaka.** Biomedical applications of predictive computational chemistry. Tartu, 2003. 132 p.
36. **Kostyantyn Kirichenko.** Benzotriazole – Mediated Carbon–Carbon Bond Formation. Tartu, 2003. 132 p.
37. **Gunnar Nurk.** Adsorption kinetics of some organic compounds on bismuth single crystal electrodes. Tartu, 2003, 170 p.
38. **Mati Arulepp.** Electrochemical characteristics of porous carbon materials and electrical double layer capacitors. Tartu, 2003, 196 p.
39. **Dan Cornel Fara.** QSPR modeling of complexation and distribution of organic compounds. Tartu, 2004, 126 p.
40. **Riina Mahlapuu.** Signalling of galanin and amyloid precursor protein through adenylate cyclase. Tartu, 2004, 124 p.

41. **Mihkel Kerikmäe.** Some luminescent materials for dosimetric applications and physical research. Tartu, 2004, 143 p.
42. **Jaanus Kruusma.** Determination of some important trace metal ions in human blood. Tartu, 2004, 115 p.
43. **Urmas Johanson.** Investigations of the electrochemical properties of polypyrrole modified electrodes. Tartu, 2004, 91 p.
44. **Kaido Sillar.** Computational study of the acid sites in zeolite ZSM-5. Tartu, 2004, 80 p.
45. **Aldo Oras.** Kinetic aspects of dATPαS interaction with $P2Y_1$ receptor. Tartu, 2004, 75 p.
46. **Erik Mölder.** Measurement of the oxygen mass transfer through the air-water interface. Tartu, 2005, 73 p.
47. **Thomas Thomberg.** The kinetics of electroreduction of peroxodisulfate anion on cadmium (0001) single crystal electrode. Tartu, 2005, 95 p.
48. **Olavi Loog.** Aspects of condensations of carbonyl compounds and their imine analogues. Tartu, 2005, 83 p.
49. **Siim Salmar.** Effect of ultrasound on ester hydrolysis in aqueous ethanol. Tartu, 2006, 73 p.
50. **Ain Uustare.** Modulation of signal transduction of heptahelical receptors by other receptors and G proteins. Tartu, 2006, 121 p.
51. **Sergei Yurchenko.** Determination of some carcinogenic contaminants in food. Tartu, 2006, 143 p.
52. **Kaido Tämm.** QSPR modeling of some properties of organic compounds. Tartu, 2006, 67 p.
53. **Olga Tšubrik.** New methods in the synthesis of multisubstituted hydrazines. Tartu. 2006, 183 p.
54. **Lilli Sooväli.** Spectrophotometric measurements and their uncertainty in chemical analysis and dissociation constant measurements. Tartu, 2006, 125 p.
55. **Eve Koort.** Uncertainty estimation of potentiometrically measured ph and pK_a values. Tartu, 2006, 139 p.
56. **Sergei Kopanchuk.** Regulation of ligand binding to melanocortin receptor subtypes. Tartu, 2006, 119 p.
57. **Silvar Kallip.** Surface structure of some bismuth and antimony single crystal electrodes. Tartu, 2006, 107 p.
58. **Kristjan Saal.** Surface silanization and its application in biomolecule coupling. Tartu, 2006, 77 p.
59. **Tanel Tätte.** High viscosity $Sn(OBu)_4$ oligomeric concentrates and their applications in technology. Tartu, 2006, 91 p.
60. **Dimitar Atanasov Dobchev**. Robust QSAR methods for the prediction of properties from molecular structure. Tartu, 2006, 118 p.
61. **Hannes Hagu**. Impact of ultrasound on hydrophobic interactions in solutions. Tartu, 2007, 81 p.
62. **Rutha Jäger.** Electroreduction of peroxodisulfate anion on bismuth electrodes. Tartu, 2007, 142 p.

63. **Kaido Viht.** Immobilizable bisubstrate-analogue inhibitors of basophilic protein kinases: development and application in biosensors. Tartu, 2007, 88 p.
64. **Eva-Ingrid Rõõm.** Acid-base equilibria in nonpolar media. Tartu, 2007, 156 p.
65. **Sven Tamp.** DFT study of the cesium cation containing complexes relevant to the cesium cation binding by the humic acids. Tartu, 2007, 102 p.
66. **Jaak Nerut.** Electroreduction of hexacyanoferrate(III) anion on Cadmium (0001) single crystal electrode. Tartu, 2007, 180 p.
67. **Lauri Jalukse.** Measurement uncertainty estimation in amperometric dissolved oxygen concentration measurement. Tartu, 2007, 112 p.
68. **Aime Lust.** Charge state of dopants and ordered clusters formation in CaF_2:Mn and CaF_2:Eu luminophors. Tartu, 2007, 100 p.
69. **Iiris Kahn**. Quantitative Structure-Activity Relationships of environmentally relevant properties. Tartu, 2007, 98 p.
70. **Mari Reinik.** Nitrates, nitrites, N-nitrosamines and polycyclic aromatic hydrocarbons in food: analytical methods, occurrence and dietary intake. Tartu, 2007, 172 p.
71. **Heili Kasuk.** Thermodynamic parameters and adsorption kinetics of organic compounds forming the compact adsorption layer at Bi single crystal electrodes. Tartu, 2007, 212 p.
72. **Erki Enkvist.** Synthesis of adenosine-peptide conjugates for biological applications. Tartu, 2007, 114 p.
73. **Svetoslav Hristov Slavov**. Biomedical applications of the QSAR approach. Tartu, 2007, 146 p.
74. **Eneli Härk.** Electroreduction of complex cations on electrochemically polished Bi(*hkl*) single crystal electrodes. Tartu, 2008, 158 p.
75. **Priit Möller.** Electrochemical characteristics of some cathodes for medium temperature solid oxide fuel cells, synthesized by solid state reaction technique. Tartu, 2008, 90 p.
76. **Signe Viggor.** Impact of biochemical parameters of genetically different pseudomonads at the degradation of phenolic compounds. Tartu, 2008, 122 p.
77. **Ave Sarapuu.** Electrochemical reduction of oxygen on quinone-modified carbon electrodes and on thin films of platinum and gold. Tartu, 2008, 134 p.
78. **Agnes Kütt.** Studies of acid-base equilibria in non-aqueous media. Tartu, 2008, 198 p.
79. **Rouvim Kadis.** Evaluation of measurement uncertainty in analytical chemistry: related concepts and some points of misinterpretation. Tartu, 2008, 118 p.
80. **Valter Reedo.** Elaboration of IVB group metal oxide structures and their possible applications. Tartu, 2008, 98 p.
81. **Aleksei Kuznetsov.** Allosteric effects in reactions catalyzed by the cAMP-dependent protein kinase catalytic subunit. Tartu, 2009, 133 p.

82. **Aleksei Bredihhin.** Use of mono- and polyanions in the synthesis of multisubstituted hydrazine derivatives. Tartu, 2009, 105 p.
83. **Anu Ploom.** Quantitative structure-reactivity analysis in organosilicon chemistry. Tartu, 2009, 99 p.
84. **Argo Vonk.** Determination of adenosine A_{2A}- and dopamine D_1 receptor-specific modulation of adenylate cyclase activity in rat striatum. Tartu, 2009, 129 p.
85. **Indrek Kivi.** Synthesis and electrochemical characterization of porous cathode materials for intermediate temperature solid oxide fuel cells. Tartu, 2009, 177 p.
86. **Jaanus Eskusson.** Synthesis and characterisation of diamond-like carbon thin films prepared by pulsed laser deposition method. Tartu, 2009, 117 p.
87. **Marko Lätt.** Carbide derived microporous carbon and electrical double layer capacitors. Tartu, 2009, 107 p.
88. **Vladimir Stepanov.** Slow conformational changes in dopamine transporter interaction with its ligands. Tartu, 2009, 103 p.
89. **Aleksander Trummal.** Computational Study of Structural and Solvent Effects on Acidities of Some Brønsted Acids. Tartu, 2009, 103 p.
90. **Eerold Vellemäe.** Applications of mischmetal in organic synthesis. Tartu, 2009, 93 p.
91. **Sven Parkel.** Ligand binding to 5-HT_{1A} receptors and its regulation by Mg^{2+} and Mn^{2+}. Tartu, 2010, 99 p.
92. **Signe Vahur.** Expanding the possibilities of ATR-FT-IR spectroscopy in determination of inorganic pigments. Tartu, 2010, 184 p.
93. **Tavo Romann**. Preparation and surface modification of bismuth thin film, porous, and microelectrodes. Tartu, 2010, 155 p.
94. **Nadežda Aleksejeva.** Electrocatalytic reduction of oxygen on carbon nanotube-based nanocomposite materials. Tartu, 2010, 147 p.
95. **Marko Kullapere.** Electrochemical properties of glassy carbon, nickel and gold electrodes modified with aryl groups. Tartu, 2010, 233 p.
96. **Liis Siinor.** Adsorption kinetics of ions at Bi single crystal planes from aqueous electrolyte solutions and room-temperature ionic liquids. Tartu, 2010, 101 p.
97. **Angela Vaasa.** Development of fluorescence-based kinetic and binding assays for characterization of protein kinases and their inhibitors. Tartu 2010, 101 p.
98. **Indrek Tulp.** Multivariate analysis of chemical and biological properties. Tartu 2010, 105 p.
99. **Aare Selberg.** Evaluation of environmental quality in Northern Estonia by the analysis of leachate. Tartu 2010, 117 p.
100. **Darja Lavõgina.** Development of protein kinase inhibitors based on adenosine analogue-oligoarginine conjugates. Tartu 2010, 248 p.
101. **Laura Herm.** Biochemistry of dopamine D_2 receptors and its association with motivated behaviour. Tartu 2010, 156 p.

102. **Terje Raudsepp.** Influence of dopant anions on the electrochemical properties of polypyrrole films. Tartu 2010, 112 p.
103. **Margus Marandi.** Electroformation of Polypyrrole Films: *In-situ* AFM and STM Study. Tartu 2011, 116 p.
104. **Kairi Kivirand.** Diamine oxidase-based biosensors: construction and working principles. Tartu, 2011, 140 p.
105. **Anneli Kruve.** Matrix effects in liquid-chromatography electrospray mass-spectrometry. Tartu, 2011, 156 p.
106. **Gary Urb.** Assessment of environmental impact of oil shale fly ash from PF and CFB combustion. Tartu, 2011, 108 p.
107. **Nikita Oskolkov.** A novel strategy for peptide-mediated cellular delivery and induction of endosomal escape. Tartu, 2011, 106 p.
108. **Dana Martin.** The QSPR/QSAR approach for the prediction of properties of fullerene derivatives. Tartu, 2011, 98 p.
109. **Säde Viirlaid.** Novel glutathione analogues and their antioxidant activity. Tartu, 2011, 106 p.
110. **Ülis Sõukand.** Simultaneous adsorption of Cd^{2+}, Ni^{2+}, and Pb^{2+} on peat. Tartu, 2011, 124 p.
111. **Lauri Lipping.** The acidity of strong and superstrong Brønsted acids, an outreach for the "limits of growth": a quantum chemical study. Tartu, 2011, 124 p.
112. **Heisi Kurig.** Electrical double-layer capacitors based on ionic liquids as electrolytes. Tartu, 2011, 146 p.
113. **Marje Kasari.** Bisubstrate luminescent probes, optical sensors and affinity adsorbents for measurement of active protein kinases in biological samples. Tartu, 2012, 126 p.
114. **Kalev Takkis.** Virtual screening of chemical databases for bioactive molecules. Tartu, 2012, 122 p.
115. **Ksenija Kisseljova**. Synthesis of aza-β^3-amino acid containing peptides and kinetic study of their phosphorylation by protein kinase A. Tartu, 2012, 104 p.
116. **Riin Rebane.** Advanced method development strategy for derivatization LC/ESI/MS. Tartu, 2012, 184 p.
117. **Vladislav Ivaništšev.** Double layer structure and adsorption kinetics of ions at metal electrodes in room temperature ionic liquids. Tartu, 2012, 128 p.
118. **Irja Helm.** High accuracy gravimetric Winkler method for determination of dissolved oxygen. Tartu, 2012, 139 p.
119. **Karin Kipper.** Fluoroalcohols as Components of LC-ESI-MS Eluents: Usage and Applications. Tartu, 2012, 164 p.
120. **Arno Ratas.** Energy storage and transfer in dosimetric luminescent materials. Tartu, 2012, 163 p.
121. **Reet Reinart-Okugbeni**. Assay systems for characterisation of subtype-selective binding and functional activity of ligands on dopamine receptors. Tartu, 2012, 159 p.

122. **Lauri Sikk.** Computational study of the Sonogashira cross-coupling reaction. Tartu, 2012, 81 p.
123. **Karita Raudkivi.** Neurochemical studies on inter-individual differences in affect-related behaviour of the laboratory rat. Tartu, 2012, 161 p.
124. **Indrek Saar.** Design of GalR2 subtype specific ligands: their role in depression-like behavior and feeding regulation. Tartu, 2013, 126 p.
125. **Ann Laheäär.** Electrochemical characterization of alkali metal salt based non-aqueous electrolytes for supercapacitors. Tartu, 2013, 127 p.
126. **Kerli Tõnurist.** Influence of electrospun separator materials properties on electrochemical performance of electrical double-layer capacitors. Tartu, 2013, 147 p.
127. **Kaija Põhako-Esko.** Novel organic and inorganic ionogels: preparation and characterization. Tartu, 2013, 124 p.
128. **Ivar Kruusenberg.** Electroreduction of oxygen on carbon nanomaterial-based catalysts. Tartu, 2013, 191 p.
129. **Sander Piiskop.** Kinetic effects of ultrasound in aqueous acetonitrile solutions. Tartu, 2013, 95 p.
130. **Ilona Faustova**. Regulatory role of L-type pyruvate kinase N-terminal domain. Tartu, 2013, 109 p.
131. **Kadi Tamm.** Synthesis and characterization of the micro-mesoporous anode materials and testing of the medium temperature solid oxide fuel cell single cells. Tartu, 2013, 138 p.
132. **Iva Bozhidarova Stoyanova-Slavova.** Validation of QSAR/QSPR for regulatory purposes. Tartu, 2013, 109 p.
133. **Vitali Grozovski**. Adsorption of organic molecules at single crystal electrodes studied by *in situ* STM method. Tartu, 2014, 146 p.
134. **Santa Veikšina**. Development of assay systems for characterisation of ligand binding properties to melanocortin 4 receptors. Tartu, 2014, 151 p.
135. **Jüri Liiv.** PVDF (polyvinylidene difluoride) as material for active element of twisting-ball displays. Tartu, 2014, 111 p.
136. **Kersti Vaarmets.** Electrochemical and physical characterization of pristine and activated molybdenum carbide-derived carbon electrodes for the oxygen electroreduction reaction. Tartu, 2014, 131 p.
137. **Lauri Tõntson**. Regulation of G-protein subtypes by receptors, guanine nucleotides and Mn^{2+}. Tartu, 2014, 105 p.
138. **Aiko Adamson.** Properties of amine-boranes and phosphorus analogues in the gas phase. Tartu, 2014, 78 p.
139. **Elo Kibena**. Electrochemical grafting of glassy carbon, gold, highly oriented pyrolytic graphite and chemical vapour deposition-grown graphene electrodes by diazonium reduction method. Tartu, 2014, 184 p.
140. **Teemu Näykki.** Novel Tools for Water Quality Monitoring – From Field to Laboratory. Tartu, 2014, 202 p.
141. **Karl Kaupmees.** Acidity and basicity in non-aqueous media: importance of solvent properties and purity. Tartu, 2014, 128 p.

142. **Oleg Lebedev**. Hydrazine polyanions: different strategies in the synthesis of heterocycles. Tartu, 2015, 118 p.
143. **Geven Piir.** Environmental risk assessment of chemicals using QSAR methods. Tartu, 2015, 123 p.
144. **Olga Mazina.** Development and application of the biosensor assay for measurements of cyclic adenosine monophosphate in studies of G protein-coupled receptor signalinga. Tartu, 2015, 116 p.
145. **Sandip Ashokrao Kadam.** Anion receptors: synthesis and accurate binding measurements. Tartu, 2015, 116 p.
146. **Indrek Tallo.** Synthesis and characterization of new micro-mesoporous carbide derived carbon materials for high energy and power density electrical double layer capacitors. Tartu, 2015, 148 p.
147. **Heiki Erikson.** Electrochemical reduction of oxygen on nanostructured palladium and gold catalysts. Tartu, 2015, 204 p.
148. **Erik Anderson.** *In situ* Scanning Tunnelling Microscopy studies of the interfacial structure between Bi(111) electrode and a room temperature ionic liquid. Tartu, 2015, 118 p.
149. **Girinath G. Pillai.** Computational Modelling of Diverse Chemical, Biochemical and Biomedical Properties. Tartu, 2015, 140 p.
150. **Piret Pikma.** Interfacial structure and adsorption of organic compounds at Cd(0001) and Sb(111) electrodes from ionic liquid and aqueous electrolytes: an *in situ* STM study. Tartu, 2015, 126 p.
151. **Ganesh babu Manoharan.** Combining chemical and genetic approaches for photoluminescence assays of protein kinases. Tartu, 2016, 126 p.
152. **Carolin Siimenson**. Electrochemical characterization of halide ion adsorption from liquid mixtures at Bi(111) and pyrolytic graphite electrode surface. Tartu, 2016, 110 p.
153. **Asko Laaniste.** Comparison and optimisation of novel mass spectrometry ionisation sources. Tartu, 2016, 156 p.
154. **Hanno Evard.** Estimating limit of detection for mass spectrometric analysis methods. Tartu, 2016, 224 p.
155. **Kadri Ligi.** Characterization and application of protein kinase-responsive organic probes with triplet-singlet energy transfer. Tartu, 2016, 122 p.
156. **Margarita Kagan.** Biosensing penicillins' residues in milk flows. Tartu, 2016, 130 p.
157. **Marie Kriisa.** Development of protein kinase-responsive photoluminescent probes and cellular regulators of protein phosphorylation. Tartu, 2016, 106 p.
158. **Mihkel Vestli.** Ultrasonic spray pyrolysis deposited electrolyte layers for intermediate temperature solid oxide fuel cells. Tartu, 2016, 156 p.
159. **Silver Sepp**. Influence of porosity of the carbide-derived carbon on the properties of the composite electrocatalysts and characteristics of polymer electrolyte fuel cells. Tartu, 2016, 137 p.
160. **Kristjan Haav**. Quantitative relative equilibrium constant measurements in supramolecular chemistry. Tartu, 2017, 158 p.

161. **Anu Teearu**. Development of MALDI-FT-ICR-MS methodology for the analysis of resinous materials. Tartu, 2017, 205 p.
162. **Taavi Ivan**. Bifunctional inhibitors and photoluminescent probes for studies on protein complexes. Tartu, 2017, 140 p.
163. **Maarja-Liisa Oldekop**. Characterization of amino acid derivatization reagents for LC-MS analysis. Tartu, 2017, 147 p.
164. **Kristel Jukk**. Electrochemical reduction of oxygen on platinum- and palladium-based nanocatalysts. Tartu, 2017, 250 p.
165. **Siim Kukk**. Kinetic aspects of interaction between dopamine transporter and *N*-substituted nortropane derivatives. Tartu, 2017, 107 p.
166. **Birgit Viira**. Design and modelling in early drug development in targeting HIV-1 reverse transcriptase and Malaria. Tartu, 2017, 172 p.
167. **Rait Kivi**. Allostery in cAMP dependent protein kinase catalytic subunit. Tartu, 2017, 115 p.
168. **Agnes Heering**. Experimental realization and applications of the unified acidity scale. Tartu, 2017, 123 p.
169. **Delia Juronen**. Biosensing system for the rapid multiplex detection of mastitis-causing pathogens in milk. Tartu, 2018, 85 p.
170. **Hedi Rahnel.** ARC-inhibitors: from reliable biochemical assays to regulators of physiology of cells. Tartu, 2018, 176 p.
171. **Anton Ruzanov.** Computational investigation of the electrical double layer at metal–aqueous solution and metal–ionic liquid interfaces. Tartu, 2018, 129 p.
172. **Katrin Kestav.** Crystal Structure-Guided Development of Bisubstrate-Analogue Inhibitors of Mitotic Protein Kinase Haspin. Tartu, 2018, 166 p.
173. **Mihkel Ilisson.** Synthesis of novel heterocyclic hydrazine derivatives and their conjugates. Tartu, 2018, 101 p.
174. **Anni Allikalt.** Development of assay systems for studying ligand binding to dopamine receptors. Tartu, 2018, 160 p.
175. **Ove Oll.** Electrical double layer structure and energy storage characteristics of ionic liquid based capacitors. Tartu, 2018, 187 p.
176. **Rasmus Palm.** Carbon materials for energy storage applications. Tartu, 2018, 114 p.
177. **Jörgen Metsik.** Preparation and stability of poly(3,4-ethylenedioxythiophene) thin films for transparent electrode applications. Tartu, 2018, 111 p.
178. **Sofja Tšepelevitš.** Experimental studies and modeling of solute-solvent interactions. Tartu, 2018, 109 p.
179. **Märt Lõkov.** Basicity of some nitrogen, phosphorus and carbon bases in acetonitrile. Tartu, 2018, 104 p.
180. **Anton Mastitski**. Preparation of α-aza-amino acid precursors and related compounds by novel methods of reductive one-pot alkylation and direct alkylation. Tartu, 2018, 155 p.
181. **Jürgen Vahter**. Development of bisubstrate inhibitors for protein kinase CK2. Tartu, 2019, 186 p.

182. **Piia Liigand.** Expanding and improving methodology and applications of ionization efficiency measurements. Tartu, 2019, 189 p.
183. **Sigrid Selberg.** Synthesis and properties of lipophilic phosphazene-based indicator molecules. Tartu, 2019, 74 p.
184. **Jaanus Liigand.** Standard substance free quantification for LC/ESI/MS analysis based on the predicted ionization efficiencies. Tartu, 2019, 254 p.
185. **Marek Mooste.** Surface and electrochemical characterisation of aryl film and nanocomposite material modified carbon and metal-based electrodes. Tartu, 2019, 304 p.
186. **Mare Oja.** Experimental investigation and modelling of pH profiles for effective membrane permeability of drug substances. Tartu, 2019, 306 p.
187. **Sajid Hussain.** Electrochemical reduction of oxygen on supported Pt catalysts. Tartu, 2019, 220 p.
188. **Ronald Väli.** Glucose-derived hard carbon electrode materials for sodium-ion batteries. Tartu, 2019, 180 p.
189. **Ester Tee.** Analysis and development of selective synthesis methods of hierarchical micro- and mesoporous carbons. Tartu, 2019, 210 p.
190. **Martin Maide.** Influence of the microstructure and chemical composition of the fuel electrode on the electrochemical performance of reversible solid oxide fuel cell. Tartu, 2020, 144 p.
191. **Edith Viirlaid.** Biosensing Pesticides in Water Samples. Tartu, 2020, 102 p.
192. **Maike Käärik.** Nanoporous carbon: the controlled nanostructure, and structure-property relationships. Tartu, 2020, 162 p.
193. **Artur Gornischeff.** Study of ionization efficiencies for derivatized compounds in LC/ESI/MS and their application for targeted analysis. Tartu, 2020, 124 p.
194. **Reet Link.** Ligand binding, allosteric modulation and constitutive activity of melanocortin-4 receptors. Tartu, 2020, 108 p.
195. **Pilleriin Peets.** Development of instrumental methods for the analysis of textile fibres and dyes. Tartu, 2020, 150 p.
196. **Larisa Ivanova.** Design of active compounds against neurodegenerative diseases. Tartu, 2020, 152 p.
197. **Meelis Härmas.** Impact of activated carbon microstructure and porosity on electrochemical performance of electrical double-layer capacitors. Tartu, 2020, 122 p.
198. **Ruta Hecht.** Novel Eluent Additives for LC-MS Based Bioanalytical Methods. Tartu, 2020, 202 p.
199. **Max Hecht.** Advances in the Development of a Point-of-Care Mass Spectrometer Test. Tartu, 2020, 168 p.
200. **Ida Rahu.** Bromine formation in inorganic bromide/nitrate mixtures and its application for oxidative aromatic bromination. Tartu, 2020, 116 p.
201. **Sander Ratso**. Electrocatalysis of oxygen reduction on non-precious metal catalysts. Tartu, 2020, 371 p.
202. **Astrid Darnell.** Computational design of anion receptors and evaluation of host-guest binding. Tartu, 2021, 150 p.

203. **Ove Korjus.** The development of ceramic fuel electrode for solid oxide cells. Tartu, 2021, 150 p.
204. **Merit Oss.** Ionization efficiency in electrospray ionization source and its relations to compounds' physico-chemical properties. Tartu, 2021, 124 p.